Spring 2021

Fabrication, characterization of high-entropy alloys and deep learning-based inspection in metal additive manufacturing

Wenyuan Cui

Department: Mechanical and Aerospace Engineering

FABRICATION, CHARACTERIZATION OF HIGH-ENTROPY ALLOYS AND DEEP LEARNING-BASED INSPECTION IN METAL ADDITIVE MANUFACTURING

by

WENYUAN CUI

A DISSERTATION

Presented to the Faculty of the Graduate School of the

MISSOURI UNIVERSITY OF SCIENCE AND TECHNOLOGY

In Partial Fulfillment of the Requirements for the Degree

DOCTOR OF PHILOSOPHY

in

MECHANICAL ENGINEERING

2021

Approved by:

Frank Liou, Advisor
K. Chandrashekhara
Lianyi Chen
Ashok Midha
Xiaoming He

PUBLICATION DISSERTATION OPTION

This dissertation consists of the following four articles, formatted in the style used by the Missouri University of Science and Technology:

Paper I, "Fabrication and Characterization of $Al_xCrCuFeNi_2$ High-Entropy Alloys Coatings by Laser Metal Deposition," found on pages 13-27, was published in Procedia Manufacturing.

Paper II, "Fabrication of AlCoCrFeNi High-Entropy Alloy Coating on an AISI 304 Substrate via a $CoFe_2Ni$ Intermediate Layer," found on pages 28-50, was published in Entropy.

Paper III, "Metal Additive Manufacturing Parts Inspection Using Convolutional Neural Network," found on pages 51-77, was published in Applied Sciences.

Paper IV, "Laser Metal Deposition of an $AlCoCrFeNiTi_{0.5}$ High-Entropy Alloy Coating on a Ti6Al4V Substrate: Microstructure and Oxidation Behavior," found on pages 78-104, was published in Crystals.

ABSTRACT

Alloying has been used to confer desirable properties to materials. It typically involves the addition of small amounts of secondary elements to a primary element. In the past decade, however, a new alloying strategy that involves the combination of multiple principal elements in high concentrations to create new materials called high-entropy alloys (HEAs) has been in vogue. In the first part, the investigation focused on the fabrication process and property assessment of the additive manufactured HEA to broaden its engineering applications. Additive manufacturing (AM) is based on manufacturing philosophy through the layer-by-layer method and accomplish the near net-shaped components fabrication. Attempt was made to coat AlCoCrFeNi HEA on an AISI 304 stainless steel substrate to integrate their properties, however, it failed due to the cracks at the interface. The implementation of an intermediate layer improved the bond and eliminated the cracks. Next, an $AlCoCrFeNiTi_{0.5}$ HEA coating was fabricated on the Ti6Al4V substrate, and its isothermal oxidation behavior was studied. The HEA coating effectively improved the Ti6Al4V substrate's oxidation resistance due to the formation of continuous protective oxides. In the second part, research efforts were made on the deep learning-based quality inspection of additive manufactured products. The traditional inspection process has relied on manual recognition, which could suffer from low efficiency and potential bias. A neural-network approach was developed toward robust real-world AM anomaly detection. The results indicate the promising application of the neural network in the AM industry.

ACKNOWLEDGMENTS

First of all, I would like to express my sincere gratitude to my academic advisor, Dr.Frank Liou. I feel fortunate to be advised by him, who continually shares his insights, knowledge, and academic experience. In the years I worked with him, Dr.Liou set an excellent example of being professional, responsible, and calm, all of which are key to one's success. These are not only crucial to my entire Ph.D. study but also immensely valuable to my future career.

Next, I feel extremely grateful to Dr. Chandrashekhara, Dr.Lianyi Chen, Dr.Ashok Midha, and Dr. Xiaoming He for serving on my committee. During the dissertation work, they provided so much constructive feedback that significantly improves the quality of the work.

My Ph.D. study becomes so much more memorable and interesting working at LAMP. I would like to say thank you to all the labmates in our group. Outside my research work, I have been lucky to be surrounded by many great friends. I would like to thank all my friends who helped me, supported me, and had fun together.

Lastly, I would like to thank my parents for their support of my education and life. I am also thankful to my grandparents, uncles, aunts, and cousins. My parents exposed the latest technologies to me in my early childhood, which stimulated my curiosity in science and engineering. They have an excellent vision for my education and career, which turned out to be extremely important for my career growth. Thank you for encouraging me to work hard and pursue my dreams.

TABLE OF CONTENTS

Page

PUBLICATION DISSERTATION OPTION iii

ABSTRACT iv

ACKNOWLEDGMENTS v

LIST OF ILLUSTRATIONS x

LIST OF TABLES xiv

SECTION

1. INTRODUCTION 1

1.1. BACKGROUND AND RESEARCH OBJECTIVES 1

1.2. ADDITIVE MANUFACTURING OF HIGH-ENTROPY ALLOYS 3

1.3. HIGH-TEMPERATURE APPLICATION OF HIGH-ENTROPY ALLOYS 6

1.4. ANOMALY DETECTION IN ADDITIVE MANUFACTURING 6

1.4.1. Machine Learning Applications in Additive Manufacturing. 7

1.4.2. Recent Trends in Deep Learning. 10

1.5. ORGANIZATION OF THIS DISSERTATION 11

PAPER

I. FABRICATION AND CHARACTERIZATION OF $Al_xCrCuFeNi_2$ HIGH-ENTROPY ALLOYS COATINGS BY LASER METAL DEPOSITION 13

ABSTRACT 13

1. INTRODUCTION 14

2. EXPERIMENTAL 15

2.1. LMD PROCESSING 15

2.2. CHARACTERIZATION 17

3. RESULTS AND DISCUSSION 18

3.1. MICROSTRUCTURE 18

3.2. EDS AND EBSD ANALYSIS 18

3.3. VICKERS HARDNESS 22

4. CONCLUSIONS 25

ACKNOWLEDGMENTS 25

REFERENCES 25

II. FABRICATION OF ALCOCRFENI HIGH-ENTROPY ALLOY COATING ON AN AISI 304 SUBSTRATE VIA A $CoFe_2Ni$ INTERMEDIATE LAYER 28

ABSTRACT 28

1. INTRODUCTION 29

2. MATERIALS AND METHODS 31

3. RESULTS AND DISCUSSION 35

3.1. DIRECT COATING OF ALCOCRFENI HEA ON AISI 304 SUBSTRATE 35

3.2. A NEW TRANSITION ROUTE 37

3.3. AlCoCrFeNi HEA-AISI 304 WITH AN INTERMEDIATE LAYER 38

3.3.1. Microstructure. 38

3.3.2. Electron Backscatter Diffraction. 43

3.3.3. Vickers Hardness Analysis. 45

4. CONCLUSIONS 46

ACKNOWLEDGMENTS 47

REFERENCES 47

III. METAL ADDITIVE MANUFACTURING PARTS INSPECTION USING CONVOLUTIONAL NEURAL NETWORK 51

ABSTRACT 51

1. INTRODUCTION 51

2. ADDITIVE MANUFACTURING PARTS INSPECTION 56

2.1. SAMPLE PREPARATION 56

2.2. PREPROCESSING 57

2.3. DATA AUGMENTATION 57

2.4. CONVOLUTIONAL NEURAL NETWORK (CNN) ARCHITECTURE 57

2.4.1. Hyper-Parameter Tuning. 61

2.4.2. Training Details. 61

2.4.3. Evaluation Metrics. 61

3. RESULTS AND DISCUSSION 62

3.1. EVALUATION OF THE CNN ARCHITECTURE 62

3.2. IMPACT OF DATA AUGMENTATION 63

3.3. REGULARIZATION 64

3.4. PERFORMANCE EVALUATION 66

3.5. FEATURE VISUALIZATION 69

3.6. FAILURE CASE STUDY 70

4. CONCLUSION 72

ACKNOWLEDGMENTS 72

REFERENCES 73

IV. LASER METAL DEPOSITION OF AN $AlCoCrFeNiTi_{0.5}$ HIGH-ENTROPY ALLOY COATING ON A Ti6Al4V SUBSTRATE: MICROSTRUCTURE AND OXIDATION BEHAVIOR 78

ABSTRACT 78

1. INTRODUCTION 78

2. MATERIALS AND METHODS 82

2.1. SAMPLE PREPARATION 82

2.2. CHARACTERIZATION 83

2.3. OXIDATION TESTS 84

3. RESULTS AND DISCUSSION 85

3.1. MICROSTRUCTURE OF THE AS-DEPOSITED HEA 85

3.2. OXIDATION BEHAVIOR 91

3.2.1. Oxidation Kinetics 91

3.2.2. Phase Analysis 92

3.2.3. Cross-Section Morphology of Oxidate Scales. 92

3.3. DISCUSSION ON THE OXIDATION BEHAVIOR 93

4. CONCLUSION 98

ACKNOWLEDGMENTS 99

REFERENCES 99

SECTION

2. CONCLUSIONS 105

3. RECOMMENDATIONS FOR FUTURE WORK 107

REFERENCES 108

VITA 121

LIST OF ILLUSTRATIONS

PAPER I

Page

Figure 1. Schematic of the laser metal deposition (LMD) system. 17

Figure 2. Optical images of (a) the interface between $CrCuFeNi_2$ HEA and AISI 304 SS substrate, (b) microstructure of $CrCuFeNi_2$ HEA, (c) the interface between $Al_{0.75}CrCuFeNi_2$ HEA and AISI 304 SS substrate and (d) microstructure of $Al_{0.75}CrCuFeNi_2$ HEA 19

Figure 3. Elemental composition evolution (a) the interface between AISI 304 SS substrate and $CrCuFeNi_2$ HEA, (b) the interface from AISI 304 SS substrate to $Al_{0.75}CrCuFeNi_2$ HEA..... 19

Figure 4. EBSD phase map indicates predominating FCC phase in the $CrCuFeNi_2$ alloy. 22

Figure 5. EBSD phase map indicates predominating FCC phase in the $Al_{0.75}CrCuFeNi_2$ alloy.. 22

Figure 6. EDS elemental maps of $CrCuFeNi_2$ alloy, (a) region of interest, (b) element map of Fe, (c) Cr, (d) Ni and (e) Cu. 23

Figure 7. EDS elemental maps of $Al_{0.75}CrCuFeNi_2$ alloy, (a) region of interest, (b) Fe, (c) Cr, (d) Ni, (e) Cu and (f) Al.. 23

Figure 8. Vickers hardness profiles of the $Al_xCrCuFeNi_2$ (x = 0,0.75) alloys. 24

PAPER II

Figure 1. Schematic of the experimental setup, (a) laser metal deposition (LMD) system and (b) the trochoidal tool path. 34

Figure 2. (a) Optical microscopy image of the vertical transverse cross-section of direct AlCoCrFeNi HEA coating on AISI 304 substrate, (b) a high-magnification view of the dashed–line-boxed area in (a)..... 36

Figure 3. Elemental composition distribution along the interface between the AISI 304 substrate and the HEA deposit. 36

Figure 4. Vickers hardness profile of the direct coating of the AlCoCrFeNi alloy on AISI 304 stainless steel. 37

Figure 5. Ternary alloy phase diagram of Fe–Co–Ni at 1073 K [24]..... 38

Figure 6. The optical microstructure of (a) the $CoFe_2Ni$ intermediate layer and the AISI 304 substrate and (b) the AlCoCrFeNi alloy deposit and the $CoFe_2Ni$ intermediate layer... 39

Figure 7. Secondary electron image of the AlCoCrFeNi HEA microstructure at a magnification of 10000....41

Figure 8. XRD pattern of the AISI 304 substrate, the $CoFe_2Ni$ intermediate layer and the AlCoCrFeNi HEA....42

Figure 9. Elemental composition distribution along the boundary, (a) $CoFe_2Ni$ intermediate layer and AISI 304 substrate and (b) AlCoCrFeNi HEA and $CoFe_2Ni$ intermediate layer.... 43

Figure 10. (a) Inverse pole figure (IPF)IPF map of the bottom of the HEA section in the specimen; the measured region was approximately 3.4 mm × 1.2 mm, from the left to the right side in the cross-section parallel to the build direction (BD); (b) distribution of the intercept length of grains with the bin size of 10 μm; (c) pole figure of areas 1 and 3; and (d) pole figure of area 2 in (a).... 44

Figure 11. Vickers hardness profile of the AISI 304 substrate—AlCoCrFeNi HEA with the $CoFe_2Ni$ intermediate layer. 46

PAPER III

Figure 1. Examples of laser metal deposition (LMD) build parts quality optical images: (a) good quality, (b) crack, (c) gas porosity, and (d) lack of fusion with a resolution of 224 × 224 pixels. 58

Figure 2. Data augmentation: (a) origin image, (b) rotation, (c) flipping, (d) crop, (e) adding Gaussian noise, and (f) adding blur 59

Figure 3. Final schematic of the convolutional neural network (CNN) model for autonomous recognition of LMD build parts quality. 60

Figure 4. (a) The accuracy and (b) the loss values of the training and validation dataset for Model 6. 63

Figure 5. (a) The accuracy and (b) the loss values of the training and validation dataset for Model 11 using data augmentation, L2 regularization, and dropout. 65

Figure 6. Plots of accuracy and loss for (a,b) Model 15, (c,d) Model 16, (e,f) Model 17 and (g,h) Model 18. 67

Figure 7. Visualization of the (a) 32 learned filters of the first convolutional layers, (b) 32 feature maps for a crack sample, (c) 32 feature maps for a lack of fusion sample, (d) 32 feature maps for a good sample and (e) 32 feature maps for a gas porosity sample. 70

Figure 8. (a–d) Additive manufacturing build metal parts images, (e–h) attention maps corresponding to (a–d). 71

Figure 9. Examples of wrongly classified images in the test dataset of metal additive manufacturing defects.. 71

PAPER IV

Figure 1. Schematic of the laser metal deposition (LMD) experiment setup. 83

Figure 2. X-ray diffraction (XRD) pattern of the (a) Ti6Al4V substrate and (b) as-deposited $AlCoCrFeNiTi_{0.5}$ HEA. 85

Figure 3. (a) Secondary electron images of the interface between the $AlCoCrFeNiTi_{0.5}$ HEA coating and Ti6Al4V substrate, (b) energy dispersive spectroscopy (EDS) line scan along the white arrow line in (a), (c) and (d) backscattered electron images of the HEA microstructure at different magnifications. 87

Figure 4. (a) Secondary electron image and the corresponding elemental maps of (b) Al, (c) Ti, (d) Ni, (e) Fe, (f) Cr, and (g) Co of the $AlCoCrFeNiTi_{0.5}$ HEA. 88

Figure 5. (a) Electron backscatter diffraction (EBSD)- inverse pole figure (IPF) map of the XZ-plane in the as-deposited HEA sample, and (b) histogram of the grain size measurement. 90

Figure 6. Microhardness of various alloys [17,18]. 91

Figure 7. Isothermal oxidation results of $AlCoCrFeNiTi_{0.5}$ HEA and Ti6Al4V at 700 °C and 800 °C for 45 h; (a) weight gain versus oxidation time curves, the parabolic plot for (b)Ti6Al4V at 700 °C, (c) HEA at 700 °C and (d) HEA at 800 °C. 94

Figure 8. XRD patterns of the oxidized (a) Ti6Al4V at 700 °C, (b) HEA at 700 °C, and (c) HEA at 800 °C for 45 h. 94

Figure 9. Cross-sectional backscattered electron images and the corresponding elemental composition distribution along the yellow arrow for the oxidized: (a) and (b) Ti6Al4V at 700 °C, (c) and (d) HEA at 700 °C, (e) and (f) HEA at 800 °C for 45 h. 95

Figure 10. (a) Backscattered electron image and the corresponding (b) O, (c) Al, (d) Ti, (e) Cr, (f) Ni, (g) Fe and (h) Co EDS maps of the oxide scales on $AlCoCrFeNiTi_{0.5}$ HEA oxidized at 700 °C for 45 h. 96

Figure 11. (a) Backscattered electron image and the corresponding (b) O, (c) Al, (d) Ti, (e) Cr, (f) Ni, (g) Fe and (h) Co EDS maps of the oxide scales on $AlCoCrFeNiTi_{0.5}$ HEA oxidized at 800 °C for 45 h. 97

LIST OF TABLES

PAPER I Page

Table 1. Particle size distribution of the elemental powders. 16

Table 2. Nominal compositions (atomic %) of HEAs. 16

Table 3. Summary of the lattice parameter and phase fraction (%) of the $Al_xCrCuFeNi_2$ HEAs obtained from EBSD analysis. 21

Table 4. Elemental compositions of the elements at different regions in atomic % for the $CrCuFeNi_2$ and $Al_{0.75}CrCrFeNi_2$ alloys. 24

Table 5. Mixing enthalpy of different atom-pair in the $CrCuFeNi_2$ and $Al_{0.75}CrCrFeNi_2$ alloys [19] 24

Table 6. Vickers hardness of various alloys. 24

PAPER II

Table 1. Particle size distribution of the precursor elemental powders. 32

Table 2. Elemental analysis (atom %) of elemental powders as provided by the manufacturer. 32

Table 3. Nominal compositions (atom %) of $CoFe_2Ni$ and AlCoCrFeNi alloy powder blends. 32

Table 4. Elemental compositions analyzed by energy dispersive X-ray spectroscopy (EDS)of the AlCoCrFeNi HEA shown in Figure 7. 40

Table 5. Summary of phases detected by XRD analysis for AISI 304, $CoFe_2Ni$ and the AlCoCrFeNi HEA.. 42

Table 6. Vickers hardness of various alloys... 46

PAPER III

Table 1. Process conditions employed in the laser metal deposition. 56

Table 2. The number of images in each category. 58

Table 3. Experimental results with six architectures. 63

Table 4. Experimental results of Models 3–6 using data augmentation operations. 64

Table 5. Experimental results of different L2 regularization and dropout parameters. 65

Table 6. Results of fine tuning dropout parameters. 66

Table 7. Precision, recall, and F score of the final model on the test dataset. 68

Table 8. Classification accuracy of different alloys in the test dataset. 68

Table 9. The performance of classification accuracy with different methods. 68

PAPER IV

Table 1. Nominal composition (atom%) of an $AlCoCrFeNiTi_{0.5}$ high-entropy alloy (HEA). 83

Table 2. Elemental composition (atom %) of each phase in the HEA by SEM-EDS (more than 5 locations). 88

Table 3. The chemical mixing enthalpies of element pairs and atomic size [9,10] 89

Table 4. The values of the parabolic constants for various alloys. 98

SECTION

1. INTRODUCTION

1.1. BACKGROUND AND RESEARCH OBJECTIVES

Additive manufacturing (AM), also known as 3D printing technology, has developed rapidly and revolutionized how it produces the complex and high-quality components in the biomedical, transportation, and automotive industries [1]–[9]. AM process consists of successive printing layers of materials that are formed on top of each other. AM technology's primary advantages over the conventional process lie in the freedom of design and automaton, albeit the slow uptake time [10]–[12].

Currently, there are several representative AM techniques, including inkjet printing [13], fused deposition modeling (FDM) [14], selective laser melting (SLM) [15]–[17], extrusion [18], [19], direct energy deposition (DED) [2], [20], [21]. Each AM method has its specific applications based on its merits. For example, powder bed selective fusion methods are ideal for producing complex and high accuracy components [16], [20]. Extrusion-based AM processes are the favored approach for ceramic fabrication due to the simplicity and low cost of the fabrication system combined with the high-density of the fabricated parts [22]–[26]. Due to the DED process's nature, it can simultaneously feed different kinds of powders through multiple hoppers; therefore, DED is applicable for building composite materials or graded materials [27]–[30].

Materials are the basis of AM technology and hopefully extend the connotation of this advanced process, thereby boosting new opportunities for AM's future development.

The strategy of "Create Materials" proposed by Gu [31] by AM is a step-by-step approach based on the fact of "Use Materials" and "Develop Materials." As such, AM could potentially extend the traditional materials science and engineering paradigm relating to structure-property-processing-performance. Recent efforts have been made on the materials design, the selection of feedstock materials, the metallurgical behaviors, the resulted performance, and the relationship between these factors. The current state of materials development focuses on metal alloys (Ti/Al/Mg alloys, steels, Ni or Co-based superalloys [20], [31]–[37]), polymer composites [38]–[40], ceramics (Al_2O_3, or Al_2O_3-ZrO_2 system [41]–[44]) and concrete [35].

This research objective will provide comprehensive knowledge of the advanced materials processing, characterization, and neural network-based detection in metal additive manufacturing. The current research will provide critical information on the production of novel high-entropy alloys (HEAs) from the elemental powders by laser metal deposition method, microstructures, mechanical and oxidation properties of the HEA system. This study advances the knowledge of fabrication of a HEA coating on the stainless steel substrate using a novel intermediate layer, which lays the foundation of future application of HEA as a structural material. A neural network-based method has been developed to classify the defects existing in laser metal deposition fabricated parts with excellent performance. The promising results give real-time quality inspection in the industry to improve the AM product quality.

1.2. ADDITIVE MANUFACTURING OF HIGH-ENTROPY ALLOYS

Recent advancements in metallic materials and alloys for AM are increasing the range of usable materials. Current studies are being conducted on the High-entropy alloys (HEAs). They are a relatively new alloy design strategy in which a minimum of five principal elements are combined to a concentration of 5-35 atom (at.) % to produce high entropies of mixing (1.61R, compared to < 0.69R for conventional alloys, where R is the gas constant) [45]. The high mixing entropy may lead to non-ordered solid solution crystal structures, such as body-centered (BCC) or face-centered (FCC). There are other inherent characteristics in addition to the high-entropy effect: lattice distortion effect, sluggish diffusion effect, and cocktail effect [45]–[47]. Due to the multi-component alloy design concept, HEAs exhibit property combinations not found in the conventional alloys [20], [34], [48]–[52], such as high hardness, strength and wear resistance, exceptional high-temperature strength, and high corrosion and oxidation resistance [53].

Among the various HEAs, $Al_xCoCrFeNi$ (x value in molar ratio) [45], [46], [54]–[61] is one of the most comprehensively investigated systems due to the relative abundance of constituent elements coupled with excellent mechanical properties. As the mechanical properties depend on the microstructure, the latter has been studied intensively. The as-cast equiatomic AlCoCrFeNi alloy has a BCC+B2 crystal structure, which decomposes into dendrites and interdendrites, both containing CrFe-rich precipitates embedded in a NiAl-rich matrix. The AlNi-rich phase is an ordered B2 type, and the CrFe-rich phase belongs to a disordered BCC phase [60]. The microstructure of as-cast AlxCoCrFeNi can be tailored from a single FCC phase, duplex FCC and BCC phase to a single BCC phase with the increasing aluminum mole ratio; meanwhile, the

hardness increases from 116 HV to 509 HV [59]. AlCoCrFeNi exhibited impressive 1.37-1.45 GPa yield stress, 2.96-3.53 GPa ultimate stress and 15.5-24.5% strain from the compression results [57], [58]. However, the as-cast AlCoCrFeNi showed a poor tensile elongation of only 1.0% due to the limited dislocation motion through these finely-spaced interfaces (50-100 nm) [55]. After the heat treatment, the FCC phase's occurrence of ductility and reduced casting defects could lead to improved elongation to 11.7% [55]. The heat treatment also makes an impact on the microstructures and properties. Lin et al. found out the age-hardening occurred in the temperate range between 350-950 °C [56]. The formation of the brittle sigma phase was detected around 1273K, restricting their usage in high temperatures. FCC phase was formed at the grain boundaries after aging, which helped improve ductility and decreased yield strength [54].

Various processing routes have been utilized to fabricate HEAs, such as casting, arc melting, plasma sintering, and laser metal deposition (LMD). LMD is an additive manufacturing technology that can produce fully dense metallic parts with complex near-net-shape by deposition of powders layer by layer [61]. This encourages a variety of metallic parts fabricated by LMD, such as stainless steels (304L, 316L, 17-4PH), Co-Cr alloys (Co28Cr6Mo), tool steels (H13), Ni-based superalloys (Inconel 625, Inconel 728), Ti-based alloy (commercial purity grade 1 and 2, Ti-6Al-4V), functionally gradient materials (304 SS to Ti-6Al-4V, 304 SS to Inconel 625, 316 SS to Ti-6Al-4V, Cu to Inconel 718) [62]. LMD can use the pre-alloyed powders or pure elemental powders. With the possibility of using elemental powder blends and controlled supply from several hoppers, LMD provides an alternative process to efficiently and effectively prepare in situ homogenous HEAs.

HEA coatings have been prepared by LMD in the recent years, such as those of 6FeNiCoSiCrAlTi [63], TiVCrAlSi [64], $FeCoNiCrCuTiMoAlSiB_{0.5}$ [65], $Al_2CrFeCoCuTiNi_X$ [66], $Al_XFeCoNiCuCr$ [67] and CoCrCuFeNi [68]. The laser engineered net shaping (LENS) produced AlCoCrFeNi alloy exhibited an average microhardness of approximately 543 $HV_{0.5}$, and this approximately 13% higher than the hardness in the as-cast state due to the grain refinement in the LENS-produced alloy [69]. AlNiCoCuFeNi HEA was fabricated on Mg substrates using laser cladding, and some Cu diffused into the Mg melt and subsequently solidified following the Mg-Cu phase diagram [70]. AlCoCrFeNi HEA coating on the Al substrate showed superior corrosion resistance, which could be attributed to the reduced dilution and formation of the HEA phase [71]. Zhang et al. have performed a similar study, FeCoCrAlNi HEA alloy coating was synthesized on 304 stainless steel to enhance corrosion and cavitation erosion resistance [72]. When Ti was added in the AlCoCrFeNi system, it led to Ti_2Ni or Fe_2Ti intermetallic phases besides the FCC and BCC phases. The phase transition and the increase in atom size difference with Ti's addition explained the enhanced microhardness and cavitation erosion resistance [73], [74]. The compositionally graded $Al_XCrCuFeNi_2$ (x varying from 0 to 1.5) alloys were processed using LENS technology, which permitted a detailed transition in microstructure along the same alloy gradient. The increasing Al content made a progressive increase in BCC/B2 microstructure and stronger ferromagnetic [75]. Previous research has demonstrated that AlCoCrFeNi HEA is attractive coating materials for enhancing surface properties.

1.3. HIGH-TEMPERATURE APPLICATION OF HIGH-ENTROPY ALLOYS

To seek HEAs' applications in the aerospace industry or other fields, an understanding of their oxidation behaviors and the development of models to predict their behaviors are required. To the best knowledge of the author, the research in this field is lacking. With regarding oxidation, HEAs are less compositionally constrained than conventional structural alloys (e.g., stainless steels, Ni-based superalloys) since they accommodate higher concentrations of the elements that are necessary to form protective external oxide scales (e.g., Al or Cr) [76]–[79]. Secondly, HEAs have been reported to own sluggish diffusion kinetics, which could improve their oxidation behaviors by inhibiting the formation of non-protective transient oxides [80]–[86]. With this in mind, there have been several investigations of the oxidation behaviors of different HEAs. Their results indicate that HEAs tend to selectively oxidize and exhibit varying modes of oxide growth [87]–[92]. Huang et al. studied the enhancement in oxidation resistance of Ti6Al4V alloy at 800 °C in the air due to the laser clad coating of AlSiTiVCr HEA. The enhancement in oxidation resistance was attributed to dense and adherent multi-oxide scale [64]. Zhang et al. demonstrated remarkable thermal stability of laser cladding CrFeCoNiCu HEA coating on the Q235 steel substrate up to 750 °C [68]. Butler reported that AlCoCrFeNi HEAs selectively oxidized to form predominantly Al_2O_3 and Cr_2O_3 scales and presented some parabolic oxide growth similar to model NiCrAl alloys [92].

1.4. ANOMALY DETECTION IN ADDITIVE MANUFACTURING

AM has demonstrated promising potential in the medical, construction, or automobile field, particularly for custom designs and functionally critical parts

manufactured locally at distinct locations. However, uncertainties regarding the product quality have hindered the full introduction of AM technology in these fields [93], [94]. Generally, the product quality is influenced by the materials' microstructures and defects, such as porosity, cracks, or lack of fusion [95]–[102]. The defects are highly dependent on numerous processing parameters, such as the laser scanning speed, laser power, or layer thickness. The process-structure-property relationships have been discussed from the previous work. One approach is to conduct experiments to obtain reliable data and optimize the processing parameters, which could be either time-consuming or expensive. The second method to ensure product quality and process reliability is the in-situ monitoring systems. For example, thermal camera, high-speed digital camera, stereomicroscope, and acoustic sensor have been developed and applied for data acquisition in AM monitoring [101], [103]. Zhang reported that stereomicroscope could capture the AM metallic parts' surface, and the detected weld features could reflect the manufacturing quality [104]. Materials scientists or engineers can identify the product quality, but human labor could lead to time-consuming, high-cost or evaluation bias for mass production. Therefore, this challenge is being addressed by applying machine learning in additive manufacturing [105]–[107].

1.4.1. Machine Learning Applications in Additive Manufacturing. Machine learning (ML) is an artificial intelligence (AI) technique that allows machines or systems to learn from data automatically and decisions or predictions [105], [108]. ML is gaining popularity in autonomous driving, fraud detection, natural language processing, object detection, medical diagnostics, materials property prediction, and smart manufacturing

[109]–[114]. In general, ML algorithms are commonly categorized as supervised, unsupervised, and reinforcement learning.

Supervised learning enables the algorithm to learn from a set of labeled data in a training set to predict unlabelled data from a test set with the highest possible accuracy. The objective function is the cost function, which calculates the errors between the predicted output values and the actual output values [106], [115]. During the training process, the parameters or weights are updated to minimize the cost function after each iteration. The unseen data is introduced to the algorithms to provide an unbiased evaluation of the model's accuracy. Multiple supervised ML methods have been utilized in the field of AM industry, i.e., Decision Tree (DT), K-Nearest Neighbor (KNN), Support Vector Machine (SVM), Linear Discriminant Analysis (LDA) [116].

As indicated in the name, unsupervised learning will study the relationship among the unlabeled data. Therefore, it uncovers the hidden pattern or cluster similarities together from the given dataset. Unsupervised learning is often used in the recommendation systems (e.g., e-commerce, online advertisement), anomaly detection (e.g., signal processing, finance, manufacturing) [117]–[119]. Reinforcement learning is semi-supervised learning how to map situations to actions to yield the most significant rewards. It requires no training dataset and allows the model to interact with the environment [120], [121]. Reinforcement learning is popularly adopted in disciplines like robotic arms, autonomous driving, and AlphaGo [122]–[124].

In the past few years, ML's application has gained increasing attention in the AM field due to its unprecedented performance in the AM design, process, and production. Generally, ML can be leveraged to optimize process parameters, conduct in-process

defects monitoring, pre-manufacturing planning, and quality assessment [105], [125]–[128]. For example, process parameter development and optimization have been traditionally implemented by designing experiments or simulation methods. Nevertheless, the design of the experiment approach usually involves trial-and-error, which is time-consuming and costly. Even though the physical-based simulation could reveal the AM process's underlying mechanism, it may suffer from the discrepancies with experimental results for its simplified physical assumptions. Therefore, many research works have explored the possibility of solving the above challenges by ML approaches. Aoyagi et al. proposed an SVM method to predict the surface quality in the electron beam melting process [125]. Their results showed that the CoCr process window could be determined by a small amount of data (precisely, 11 data points) and could be used to optimize the process parameters unique to the machine. Bayes classifier and DT were implemented to investigate the influence of support structure parameters on the electron beam produced parts [126]. Similar work has been performed to estimate the melt pool geometry in laser deposition and predict the maximal printable height in the materials extrusion process. It is found that ML has been used to link the process parameters to the quality indicators at mesoscale (i.e., porosity, melt pool geometries) [127]and macroscale (mechanical properties) levels [128].

The AM process suffers from various process-related defects like lack of fusion, cracks, porosity, delamination, and keyhole, which results from one layer to the subsequent layers and lead the build to fail. There have been many efforts addressing AM process quality monitoring, which involve the acoustic-based, optical-based, or computed tomography (CT) inspection. Ye et al. collected acoustic signals by a microphone, and

the framework of a deep belief network could reach a defect detection accuracy up to 95% with Fast Fourier transformation and denoising [129]. A fiber Bragg grating acoustic sensor was employed to collect the quality features for the SLM process [130]. In particular, the time span for each running window was configured to be 160 ms to achieve a balance between the spatial resolution and classification accuracy. A high-speed visible-light camera with a fixed field of view was used to observe the melt pool morphology in a commercial powder-bed machine autonomous detection of six powder bed anomalies via Bag of Words algorithm [115]. A porosity prediction method was developed using a thermal monitoring system to capture the melt-pool morphological characteristics [116]. Supervised learning methods were utilized to identify the melt pool images' patterns, which KNN had the highest rate of accuracy of 98% among the various models (i.e., DT, KNN, SVM, LDA). A binary classification via SVM was developed and implemented on the in-situ CT-based powder-ped process inspection [107]. The authors found the discontinuities, i.e., incomplete fusion, porosity, or inclusions, were identified using automated analysis or manual inspection. Through fine-tuning and cross-validation, the in-situ detection accuracy of over 80% was achieved.

1.4.2. Recent Trends in Deep Learning. Conventional machine learning techniques have been limited in their ability to process natural data in the raw form. It is usually required careful engineering and domain expertise to design a feature extractor that transforms the raw data, i.e., the pixel values of an image, into a suitable internal representation or feature vector [131], [132]. Deep learning is making significant advances in the artificial intelligence community for years, which uses multiple processing layers to learn data representations. LaCun stated that as deep learning takes

much less engineering by hand, it can easily take advantage of the increasingly available data [131]. Current and new learning algorithms deployed for deep neural networks with cloud computing will accelerate this progress.

Despite such success, a few studies have been performed using deep learning in the materials informatics community. A convolutional neural network (CNN) was adopted to link the microstructure with ionic conductivity in yttria-stabilized zirconia [133]. The results revealed that seven micrographs could train CNN, and its performance exceeded the traditional hand-crafted features scheme. CNN was also carried out for defects detection in photovoltaic cell images of 93% accuracy on an ordinary computer, which could help manual labeling [134]. One major obstacle is the lack of well-labeled data, as it takes a few days to obtain the optical or electron microscope patterns [135], which requires a great deal of time and expense. Another reason is the difficulty in feeding meaningful information from deep learning networks to materials researchers, as the representations are highly abstract.

1.5. ORGANIZATION OF THIS DISSERTATION

This research work aims to advance the knowledge of fabrication of high-entropy alloys (HEAs) and the application of artificial intelligence in the field of laser metal additive manufacturing (AM). To achieve this goal, four papers are listed as follow:

Study the feasibility of fabrication of a HEA alloy by laser metal deposition (LMD). $Al_xCrCuFeNi_2$ (x in molar ratios) HEA alloys will be prepared by elemental powder blends. The evolution of chemistry, phases, and hardness will be performed by

energy dispersive diffraction (EDS), X-ray diffraction (XRD). The grain size will be studied by electron backscatter diffraction (EBSD).

AlCoCrFeNi HEA coating will be fabricated on AISI 304 stainless steel (SS) substrate by laser metal deposition. Crack has been found during the direct deposit AlCoCrFeNi HEA coating on AISI 304 SS, so a novel intermediate layer will be proposed to bridge the composition differences gap. The intermediate layer, the phase structure and elemental composition change will be examined by XRD and EDS. EBSD will characterize the texture and grain size of the HEA coating.

To enhance the oxidation resistance of titanium alloy, $AlCoCrFeNiTi_{0.5}$ HEA coating will be synthesized on the Ti6Al4V substrate. First, AlCoCrFeNiTi HEA coating will be deposited on the Ti6Al4V substrate, and its microstructure, interface characteristics, and phase composition will be investigated. Secondly, high-temperature properties will be evaluated in terms of the thermal oxidation behaviors and phase compositions. The present study will help the future design of HEAs towards high-temperature structural applications.

A convolutional neural network (CNN) approach will be presented towards robust AM quality inspection, including good quality, crack, gas porosity, and lack of fusion. To obtain the appropriate model, extensive experiments will be performed on a series of architectures. Besides, data augmentation will be adopted to deal with data scarcity. L_2 regularization and dropout will be applied to avoid overfitting.

A conclusion section is presented after the four papers to summarize the current work. The recommendations for future work are proposed at the last section.

PAPER

I. FABRICATION AND CHARACTERIZATION OF $Al_xCrCuFeNi_2$ HIGH-ENTROPY ALLOYS COATINGS BY LASER METAL DEPOSITION

ABSTRACT

High-entropy alloys (HEAs) are becoming new hot spots in the metallic materials community, which are defined to contain equiatomic or close-to-equiatomic compositions. HEAs can possess many interesting mechanical properties, and in particular, they have the great potential to be used as coating materials requiring high hardness and wear resistance. In this study, the feasibility of fabrication $Al_xCrCuFeNi_2$ (x=0,0.75) HEAs was investigated via laser metal deposition from elemental powders. The microstructure, phase structure, and hardness were studied by an optical microscope, scanning electron microscopy with energy dispersive spectroscopy (SEM/EDS), electron backscatter diffraction (EBSD) and Vickers hardness tester. The bonding between the $Al_xCrCuFeNi_2$ (x = 0,0.75) HEAs and AISI 304 stainless steel were good combinations. The $Al_{0.75}CrCrFeNi_2$ alloy consisted of columnar dendritic microstructure with Al/Ni enrichment in the dendritic regions. The phase structure of the $Al_xCrCuFeNi_2$ (x = 0,0.75) HEAs were face center cubic structure as identified by EBSD. Vickers hardness results indicate that the average hardness of $CrCuFeNi_2$ HEA was 175 HV. With the addition of aluminium, the Vickers hardness of $Al_{0.75}CrCuFeNi_2$ HEA increased to 285 HV.

1. INTRODUCTION

Conventional metallurgical theory suggests that the multiple alloying elements in an alloy may result in the formation of complex compounds. Recently this paradigm has been broken by high-entropy alloys (HEAs) developed by Yeh et al. [1] HEAs are composed of five or more principle elements in equimolar or near-equimolar ratios. The high mixing entropy of multi-principle elements induces the formation of solid-solution structure, e.g., face center cubic (FCC) or body center cubic (BCC) or FCC combined with BCC [1-6]. The discovery of HEAs has brought a new alloy design concept and generated researchers' interest in the past decade. An AlCrFeCoNi HEA was prepared by vacuum arc melting and exhibited excellent compressive strength 2004.23 MPa [2]. Another study of $AlCrFeCuNi_x$ ($0.6 \leq x \leq 1.4$) HEAs was prepared by casting reported by Jinhong et al., which found the hardness of as-cast HEAs decreased as x increased from 1.0 to 1.4 [3]. Dong et al. investigated the $AlCrFeNiMo_x$ (x = 0,0.2,0.5,0.8 and 1.0 in molar ratios) HEAs produced by vacuum melting [7]. Their work showed $AlCrFeNiMo_{0.2}$ HEA possessed good fracture strength of 3222 MPa and plastic strain of 0.287, which implies its potential application in industrial areas. These HEAs were fabricated by casting or vacuum melting. Unlike the previous studies, this work will implement the laser metal deposition (LMD) method to fabricate the $Al_xCrCuFeNi_2$ (x = 0, 0.75 in molar ratios) HEAs.

As an advanced additive manufacturing technology, LMD can accomplish layer-by-layer fabrication of near net-shaped components by introducing a powder stream through a high energy laser beam [4,5,8-10]. A melt pool is formed by rastering the laser

beam, and the powders are injected into the melt pool to deposit each layer during the LMD process. Layer by layer composition changes, the introduction of a dissimilar metal interlayer and control over the melt zone size can be accommodated [4,9-13]. A FeCoNiCrCu HEA coating was synthesized, and its microhardness reached 375 $HV_{0.5}$, which was about 50% higher than that of the same alloy prepared by arc melting [4]. With the additional of titanium content, $Al_2CrFeNiCoCuTi_x$ (x = 0, 0.5, 1.0, 1.5 and 2.0 in molar ratios) HEAs showed good corrosion and wear resistance on Q235 steel substrate [10]. Few research has been devoted to the fabrication of $AlCrCuFeNi_2$ HEAs by LMD.

In this paper, the feasibility of fabrication $Al_xCrCuFeNi_2$ (x = 0, 0.75 in molar ratios) HEA coatings on AISI 304 stainless steel (SS) was performed by laser metal deposition technology using elemental powders. The metallurgical bonding, microstructure, and Vickers hardness were investigated.

2. EXPERIMENTAL

2.1. LMD PROCESSING

Gas-atomized elemental powders of aluminium (Al), chromium (Cr), copper (Cu), iron (Fe) and nickel (Ni) purchased from Atlantic Equipment Engineers Inc. was used as precursor materials. The particle size of the elemental powders provided by Atlantic Equipment Inc. is as tabulated in Table 1. The elemental powders were weighted in the required ratios and then mixed by a Turbula mixer (Glen Mills Inc., Clifton, NJ, USA)

for 30 mins to obtain homogeneous blends. Elemental compositions (atomic %) of the as-blended HEAs are given in Table 2.

Table 1. Particle size distribution of the elemental powders.

Materials	US Standard Mesh
Al	-100
Cr	-100
Cu	-100
Fe	-100
Ni	-100/+325

Table 2. Nominal compositions (atomic %) of HEAs.

Alloys	Al	Cr	Cu	Fe	Ni
$CrCuFeNi_2$	0	20	20	20	40
$Al_{0.75}CrCuFeNi_2$	13	17	17	17	36

The schematic of the LMD system is shown in Figure 1. The 1 kW continuous-wave YAG fiber laser (IPG, Photonics, Oxford, MA, USA) was used as a heat source with a beam diameter of 2 mm. The metallic powders were fed through a vibration X2 powder feed system (Powder Motion Labs, MO, USA). The powders were introduced into the melt pool by an alumina tube. Argon gas was used as a carrier gas to deliver the powder mixtures to the melt pool. The movement during the laser deposition was achieved through a computer numerical control (CNC) table.

Commercially procured AISI 304 SS bar stock (dimension: 2 inch × 2 inch × 0.25 inch) was used as the substrate and cleaned with acetone to clean the surface. A preheating scan was performed by running the laser across the substrate. The thin wall structure was built, and the laser power of the initial three layers was conducted at 700 W

and 8.5% (3.36 g/min) powder feed rate. The remaining of the deposition was carried out at 600 W and 8.5% (3.36 g/min) powder feed rate with 1 mm layer thickness.

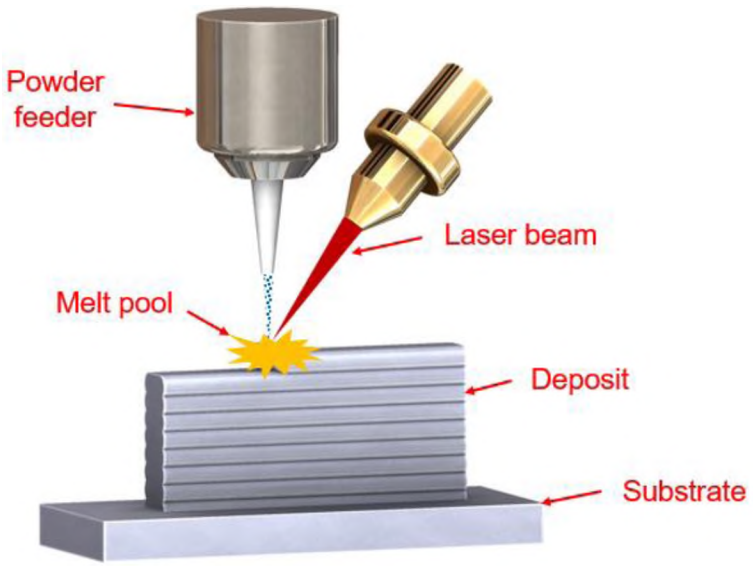

Figure. 1. Schematic of the laser metal deposition (LMD) system.

2.2. CHARACTERIZATION

For microstructural characterization, the deposits were transverse cross-sectioned and prepared with standard metallographic methods. The samples were polished with 320-1200 grit SiC grinding paper, and the final mechanical polish was 0.05 μm silica suspension. The specimens were given the electrolytic etching in the nitric acid solution (70 mL nitric acid and 30 mL distilled water).

A Hirox optical microscope investigated the $Al_xCrCuFeNi_2$ HEAs morphology. The scanning electron microscopy (SEM), elemental analysis using energy dispersive spectroscopy (EDS), and electron backscatter diffraction (EBSD) studies of the specimens were carried out in a Helios Nanolab 600 SEM coupled with an EDS and an

EBSD detector. The obtained EBSD data was processed and analyzed using Aztec software. The hardness was obtained with a Struers Duramin hardness tester (Struers Inc., Cleveland, OH, USA) using a 9.81 N force and 10 s load duration.

3. RESULTS AND DISCUSSION

3.1. MICROSTRUCTURE

Figure 2 shows the optical images of the deposited HEAs. The deposit was shown in the top area in Figure 2a while the bottom part was AISI 304 SS substrate. An explicit interface was seen between the deposit and the AISI 304 SS substrate. The columnar dendrite microstructure was observed from Figure 2b. Similarly, a good metallurgical bonding existed between $Al_{0.75}CrCuFeNi_2$ HEA and the AISI 304 SS substrate. The dendritic continued in $Al_{0.75}CrCuFeNi_2$ alloy. The growth direction of these columnar was identified to be along with the deposition direction, which could be correlated with the solidification direction during the LMD process.

3.2. EDS AND EBSD ANALYSIS

The evolution in chemistry from the substrate to the $CrCuFeNi_2$ HEA was characterized by EDS line scan first. The quantitative results are plotted in Figure 3a. The results measured by EDS of the AISI 304 SS substrate (Cr: ~18-19 atomic %, Fe: ~70-71 atomic %, Ni: ~9-10 atomic % in Figure 3a) did not derive from the nominal AISI 304 SS chemical compositions. Mn (~ 1-2 atomic %) was detected by EDS in AISI 304 SS substrate but was not shown in Figure 3.

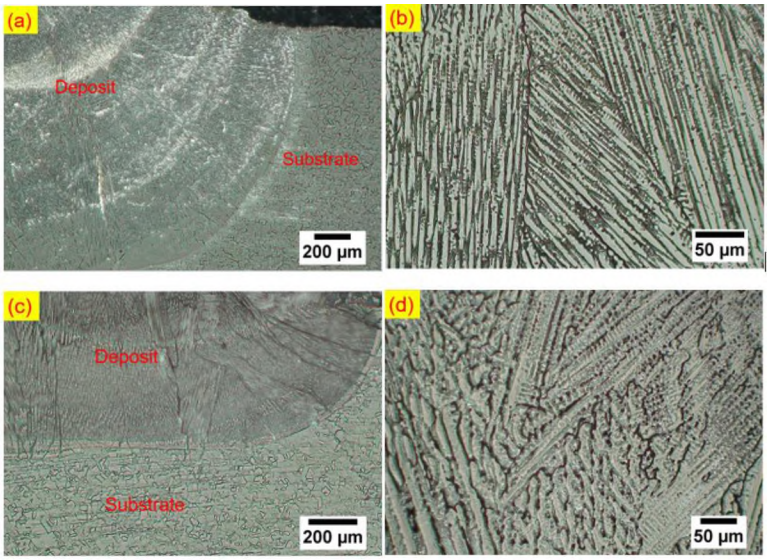

Figure 2. Optical images of (a) the interface between $CrCuFeNi_2$ HEA and AISI 304 SS substrate, (b) microstructure of $CrCuFeNi_2$ HEA, (c) the interface between $Al_{0.75}CrCuFeNi_2$ HEA and AISI 304 SS substrate and (d) microstructure of $Al_{0.75}CrCuFeNi_2$ HEA.

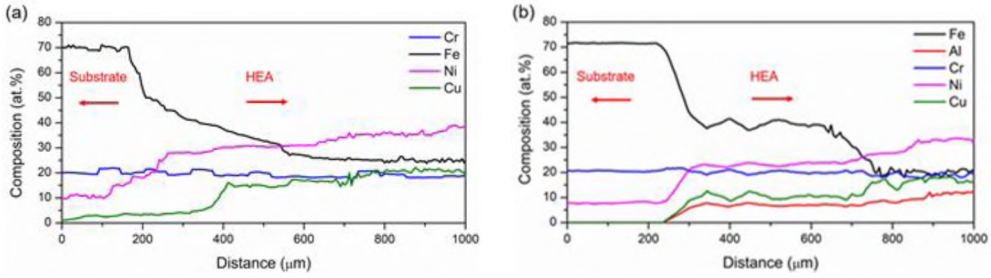

Figure 3. Elemental composition evolution (a) the interface between AISI 304 SS substrate and $CrCuFeNi_2$ HEA, (b) the interface from AISI 304 SS substrate to $Al_{0.75}CrCuFeNi_2$ HEA.

The elemental compositions of Cu (~18-21 atomic %) and Ni (~35-38 atomic %) increased while that of Fe (~23-26 atomic %) reduced, and Cr (~20 atomic %) remained changed from the substrate to the $CrCuFeNi_2$ HEA deposit. A small amount of Cu (~1-2 atomic %) was detected in the substrate because the substrate was mixed with the HEA

deposit. The distribution of the consisted compositions from the substrate to the $Al_{0.75}CrCuFeNi_2$ HEA was shown in Figure 3b. The constituents of the $Al_{0.75}CrCuFeNi_2$ HEA were determined by EDS (Al: ~9-10 atomic %, Cr: ~19 atomic %, Cu: ~17 atomic %, Fe: ~20 atomic %, Ni: ~ 32-34 atomic %). The difference between the as-blended (13 atomic %) and as-deposited aluminum (~9-10 atomic %) compositions could be attributed to the inconsistency of powder capture efficiency and evaporation due to its low melting point.

EBSD and EDS measurements were conducted in the aim of differentiating structure and phase information of the $Al_xCrCuFeNi_2$ (x = 0, 0.75) alloys. Regions of interest and phase analysis of $CrCuFeNi_2$ and $Al_{0.75}CrCuFeNi_2$ alloys are shown in Figures 4 and 5 respectively. Figures 4 and 5 indicate an FCC structure in both HEA fabrications. The phase fractions and the corresponding lattice parameter identified by EBSD are listed in Table 3. The zero solution is the fraction of the selected area whose crystal structure could not be solved by the software.

Figures 6 and 7 show the EDS element maps obtained from the $Al_xCrCuFeNi_2$ HEAs. The Fe-Kα, Cr-Kα, Ni-Kα, Cu-Kα and Al-Kα signals were used to estimate the elemental compositions within the regions of interest in the deposits. EDS elemental compositions were gathered from the dendritic microstructures for the $Al_xCrCuFeNi_2$ (x = 0, 0.75) HEAs. The standardless measurements are listed in Table 4. The microstructure of $CrCuFeNi_2$ alloy exhibited a dendritic microstructure as reported previously. Based on the previous EBSD phase analysis, this dendritic phase was likely to be a single FCC phase. While it was observed a distinct contrast between the dendritic and interdendritic regions (as seen in Figure 6), this contrast could be attributed to the

segregation of Cu (which tended to partition and segregate readily [14,15]) as in Figure 6e. Table 4 shows that Cu was enriched in the interdendritic regions. Figure 7 indicates that with the addition of aluminum, $Al_{0.75}CrCuFeNi_2$ alloy contained predominantly two phases. Associated with the results from Table 4, the dendritic phase was observed to be Al and Ni rich (Al+Ni: ~41 atomic %, Fe+Cr: ~18 atomic %), while the interdendritic microstructure was rich in Fe and Cr (Al+Ni: ~28 atomic %, Fe+Cr: ~52 atomic %). The Cu was deficient in the interdendritic regions.

Table 3. Summary of the lattice parameter and phase fraction (%) of the $AlxCrCuFeNi_2$ HEAs obtained from EBSD analysis.

Alloy	Phase Name	Space Group	Lattice Parameter (Å)	Fraction (%)
$CrCuFeNi_2$	FCC	Fm-3m (225)	3.66	88.2
	BCC	Im-3m (229)	2.93	0.13
	Zero solution	-	-	11.67
$Al_{0.75}CrCuFeNi_2$	FCC	Fm-3m (225)	3.66	99.3
	BCC	Im-3m (229)	2.93	0.09
	Zero solution	-	-	0.61

From the mixing enthalpy of atom-pair as listed in Table 5, it clearly shows that the mixing of enthalpy of Al and Ni is higher (-22 kJ/mol) than of other atom-pair. It indicates that Al and Ni atoms tend to form atom pairs and segregate. Similar results have been reported previously, with this microstructure being attributed to the spinodal decomposition [2,6,16-18].

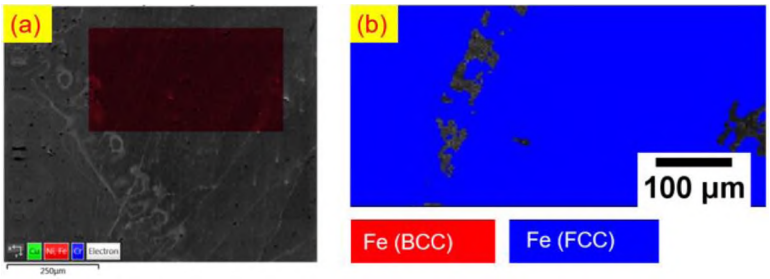

Figure 4. EBSD phase map indicates predominating FCC phase in the $CrCuFeNi_2$ alloy. (a) The region of interest on $CrCrFeNi_2$ alloy (b) Phase map shows predominantly FCC phase (represented by blue color) within the region of interest.

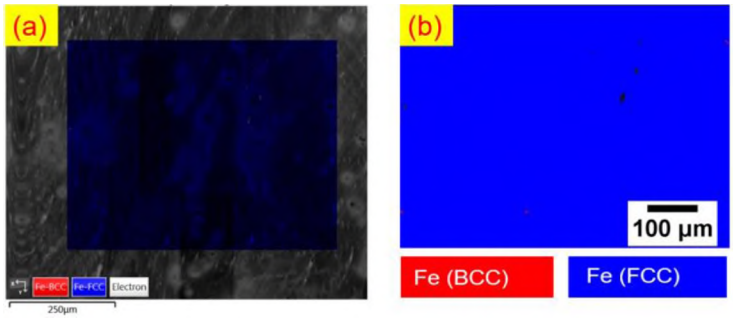

Figure 5. EBSD phase map indicates predominating FCC phase in the $Al_{0.75}CrCuFeNi_2$ alloy. (a) The region of interest on $Al_{0.75}CrCuFeNi_2$ alloy, (b) Phase map shows predominantly FCC phase (represented by blue color) within the region of interest.

3.3. VICKERS HARDNESS

Figure 8 gives the Vickers hardness profiles of the $Al_xCrCuFeNi_2$ (x = 0, 0.75) alloys deposits on the AISI 304 SS substrates. The Vickers hardness of $CrCuFeNi_2$ alloy was around 175 HV, which could be attributed to the solid solution strengthening.

Table 6 gives the Vickers hardness of various alloys, including AISI 304 SS, Inconel 625 and 7075-T6 aluminum [20,21], and $Al_{0.75}CrCuFeNi_2$ alloy has the highest average hardness of 285 HV. With the addition of aluminum, the average Vickers hardness of $Al_{0.75}CrCuFeNi_2$ HEA reached 285 HV, because the second phase

strengthening blocked the dislocation [6,18]. The high hardness of HEA coating is expected to correlate with good performance in strength and wear resistance [10,13].

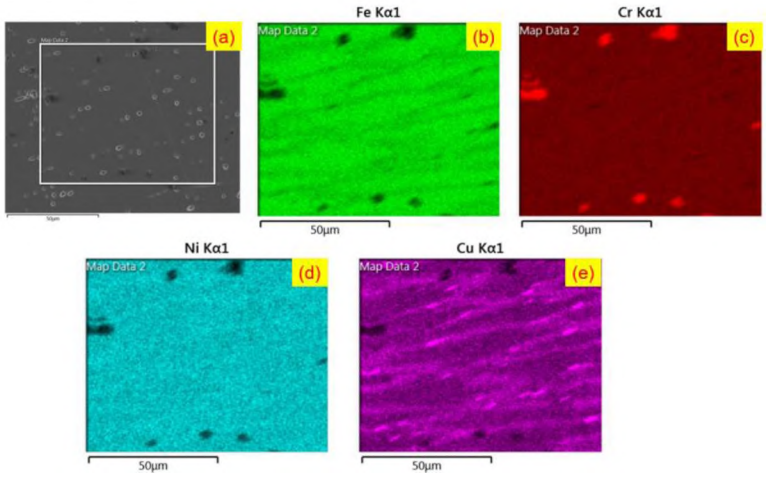

Figure 6. EDS elemental maps of $CrCuFeNi_2$ alloy, (a) region of interest, (b) element map of Fe, (c) Cr, (d) Ni and (e) Cu.

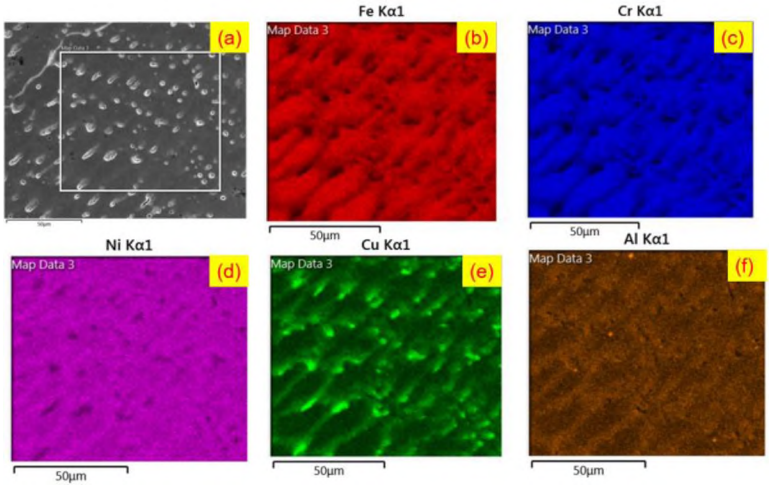

Figure 7. EDS elemental maps of $Al_{0.75}CrCuFeNi_2$ alloy, (a) region of interest, (b) Fe, (c) Cr, (d) Ni, (e) Cu and (f) Al.

Table 4. Elemental compositions of the elements at different regions in atomic % for the $CrCuFeNi_2$ and $Al_{0.75}CrCrFeNi_2$ alloys.

Alloy	Area	Al	Cr	Cu	Fe	Ni
$CrCuFeNi_2$	Nominal	0	20	20	20	40
	Dendritic	0	18.5	18.7	27.1	35.7
	Interdendritic	0	16.9	25.9	21.4	35.8
$Al_{0.75}CrCuFeNi_2$	Nominal	13	17	17	17	36
	Dendritic	15	7.3	41.4	10.3	26
	Interdendritic	8	20	24	28	20

Table 5. Mixing enthalpy of different atom-pair in the $CrCuFeNi_2$ and $Al_{0.75}CrCrFeNi_2$ alloys [19].

ΔHmix (kJ/mol)	Cu	Cr	Al	Ni
Fe	13	-1	-11	-2
Cu	-	12	-1	4
Cr	-	-	-10	-7
Al	-	-	-	-22

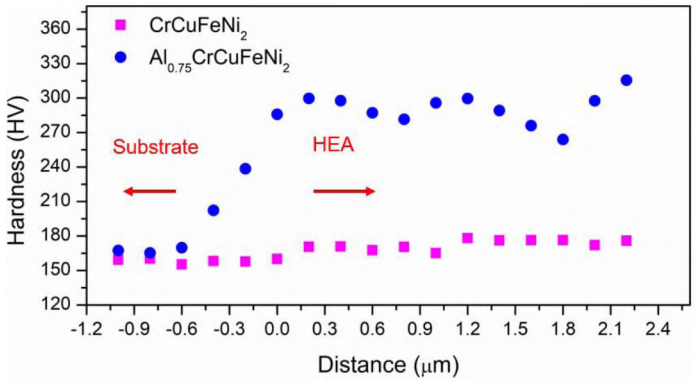

Figure 8. Vickers hardness profiles of the $Al_xCrCuFeNi_2$ (x = 0,0.75) alloys.

Table 6. Vickers hardness of various alloys.

Alloy	Hardness (HV)	Reference
$CrCuFeNi_2$	175	This work
$Al_{0.75}CrCuFeNi_2$	285	This work
AISI 304 SS	160	This work
Inconel 625	156	[21]
7075-T6 aluminum	118	[20]

4. CONCLUSIONS

$Al_xCrCuFeNi_2$ (x = 0,0.75 in molar ratios) HEAs were coated on AISI 304 stainless steel substrate via laser metal deposition technology. The metallurgical bonding, microstructure, and the Vickers hardness were investigated and discussed. The good metallurgical bonding was observed between the HEA coatings and the substrate. The $Al_xCrCuFeNi_2$ (x = 0,0.75) HEAs coating exhibited columnar dendritic microstructure and FCC structure identified by EBSD. $CrCuFeNi_2$ HEA was found to have an average hardness of 175 HV, while $Al_{0.75}CrCuFeNi_2$ HEA has a hardness of 285 HV.

ACKNOWLEDGMENTS

The authors gratefully acknowledge the financial support from NSF (National Science Foundation) grants CMMI-1547042 and CMMI-1625736. The support from the Intelligent System Center (ISC) and Materials Research Center (MRC) at Missouri University of Science and Technology are also greatly appreciated.

REFERENCES

[1] J.-W. Yeh *et al.*, "Nanostructured High-Entropy Alloys with Multiple Principal Elements: Novel Alloy Design Concepts and Outcomes," *Adv. Eng. Mater.*, vol. 6, no. 5, pp. 299–303, May 2004.

[2] Y. P. Wang, B. S. Li, M. X. Ren, C. Yang, and H. Z. Fu, "Microstructure and compressive properties of AlCrFeCoNi high entropy alloy," *Mater. Sci. Eng. A*, vol. 491, no. 1–2, pp. 154–158, Sep. 2008.

[3] P. Jinhong, P. Ye, Z. Hui, and Z. Lu, "Microstructure and properties of AlCrFeCuNix ($0.6 \leq x \leq 1.4$) high-entropy alloys," *Mater. Sci. Eng. A*, vol. 534, pp. 228–233, Feb. 2012.

[4] H. Zhang, Y. Pan, and Y.-Z. He, "Synthesis and characterization of FeCoNiCrCu high-entropy alloy coating by laser cladding," *Mater. Des.*, vol. 32, no. 4, pp. 1910–1915, Apr. 2011.

[5] W. Cui, X. Zhang, and F. Liou, "Additive Manufacturing of High-Entropy Alloys - A Review," in *Proceedings of the 28th Annual International Solid Freeform Fabrication Symposium – An Additive Manufacturing Conference*, 2017, pp. 712–724.

[6] W.-R. Wang, W.-L. Wang, S.-C. Wang, Y.-C. Tsai, C.-H. Lai, and J.-W. Yeh, "Effects of Al addition on the microstructure and mechanical property of AlxCoCrFeNi high-entropy alloys," *Intermetallics*, vol. 26, pp. 44–51, Jul. 2012.

[7] Y. Dong, Y. Lu, J. Kong, J. Zhang, and T. Li, "Microstructure and mechanical properties of multi-component AlCrFeNiMox high-entropy alloys," *J. Alloys Compd.*, vol. 573, pp. 96–101, Oct. 2013.

[8] W. Li, A. Ghazanfari, D. McMillen, M. C. Leu, G. E. Hilmas, and J. Watts, "Fabricating ceramic components with water dissolvable support structures by the Ceramic On-Demand Extrusion process," *CIRP Ann.*, vol. 66, no. 1, pp. 225–228, Jan. 2017.

[9] A. Reichardt *et al.*, "Development and characterization of Ti-6Al-4V to 304L stainless steel gradient components fabricated with laser deposition additive manufacturing," *Mater. Des.*, vol. 104, pp. 404–413, Aug. 2016.

[10] X. W. Qiu, Y. P. Zhang, and C. G. Liu, "Effect of Ti content on structure and properties of Al2CrFeNiCoCuTix high-entropy alloy coatings," *J. Alloys Compd.*, vol. 585, pp. 282–286, Feb. 2014.

[11] W. Cui, S. Karnati, X. Zhang, E. Burns, and F. Liou, "Fabrication of AlCoCrFeNi High-Entropy Alloy Coating on an AISI 304 Substrate via a CoFe2Ni Intermediate Layer," *Entropy*, vol. 21, no. 1, p. 2, Dec. 2019.

[12] W. Li *et al.*, "Fabricating Functionally Graded Materials by Ceramic On-Demand Extrusion with Dynamic Mixing," in *Proceedings of the 29th Annual International Solid Freeform Fabrication Symposium – An Additive Manufacturing Conference*, 2018, pp. 1087–1099.

[13] S. Chen, Y. Tong, P. Liaw, S. Chen, Y. Tong, and P. K. Liaw, "Additive Manufacturing of High-Entropy Alloys: A Review," *Entropy*, vol. 20, no. 12, p. 937, Dec. 2018.

[14] D. Choudhuri *et al.*, "Formation of a Huesler-like L21 phase in a CoCrCuFeNiAlTi high-entropy alloy," *Scr. Mater.*, vol. 100, pp. 36–39, Apr. 2015.

[15] T. Borkar *et al.*, "Hierarchical multi-scale microstructural evolution in an as-cast Al2CuCrFeNi2 complex concentrated alloy," *Intermetallics*, vol. 71, pp. 31–42, Apr. 2016.

[16] S. Guo, C. Ng, and C. T. Liu, "Anomalous solidification microstructures in Co-free AlxCrCuFeNi2 high-entropy alloys," *J. Alloys Compd.*, vol. 557, pp. 77–81, Apr. 2013.

[17] C. Ng *et al.*, "Phase stability and tensile properties of Co-free Al0.5CrCuFeNi2 high-entropy alloys," *J. Alloys Compd.*, vol. 584, pp. 530–537, Jan. 2014.

[18] Z. Tang *et al.*, "Tensile ductility of an AlCoCrFeNi multi-phase high-entropy alloy through hot isostatic pressing (HIP) and homogenization," *Mater. Sci. Eng. A*, vol. 647, pp. 229–240, Oct. 2015.

[19] A. Takeuchi and A. Inoue, "Classification of Bulk Metallic Glasses by Atomic Size Difference, Heat of Mixing and Period of Constituent Elements and Its Application to Characterization of the Main Alloying Element," *Mater. Trans.*, vol. 46, no. 12, pp. 2817–2829, 2005.

[20] A. S. El-Amoush, "Intergranular corrosion behavior of the 7075-T6 aluminum alloy under different annealing conditions," *Mater. Chem. Phys.*, vol. 126, no. 3, pp. 607–613, Apr. 2011.

[21] M. A. Shaikh, M. Ahmad, K. A. Shoaib, J. I. Akhter, and M. Iqbal, "Precipitation hardening in Inconel * 625," *Mater. Sci. Technol.*, vol. 16, no. 2, pp. 129–132, Feb. 2000.

II. FABRICATION OF ALCOCRFENI HIGH-ENTROPY ALLOY COATING ON AN AISI 304 SUBSTRATE VIA A $CoFe_2Ni$ INTERMEDIATE LAYER

ABSTRACT

Through laser metal deposition, attempts were made to coat AlCoCrFeNi, a high-entropy alloy (HEA), on an AISI 304 stainless steel substrate to integrate their properties. However, the direct coating of the AlCoCrFeNi HEA on the AISI 304 substrate was found to be unviable due to cracks at the interface between these two materials. The difference in compositional change was suspected to be the source of the cracks. Therefore, a new transition route was performed by coating an intermediate layer of $CoFe_2Ni$ on the AISI 304 substrate. Investigations into the microstructure, phase composition, elemental composition and Vickers hardness were carried out in this study. Consistent metallurgical bonding was observed along both of the interfaces. It was found that the AlCoCrFeNi alloy solidified into a dendritic microstructure. The X-ray diffraction pattern revealed a transition of the crystal structure of the AISI 304 substrate to the AlCoCrFeNi HEA. An intermediate step in hardness was observed between the AISI 304 substrate and the AlCoCrFeNi HEA. The AlCoCrFeNi alloy fabricated was found to have an average hardness of 418 HV, while the $CoFe_2Ni$ intermediate layer had an average hardness of 275 HV.

1. INTRODUCTION

As a novel metallic alloy system, high-entropy alloys (HEAs) have received considerable attention in the past decade. The name HEA indicates that the mixing of the principal elements in the alloy leads to a substantial change in entropy. This change in entropy promotes the formation of a simple solid solution instead of complex compounds. One of the extensively studied HEAs is equiatomic AlCoCrFeNi, which shows high hardness, good wear behavior but low tensile ductility [1-7]. As-cast AlCoCrFeNi alloy showed a tensile elongation of 1.0%, while post-heat treatment, the elongation was increased to 11.7% [4]. Wang et al. studied the compressive properties of AlCrFeCoNi HEA prepared by vacuum arc melting. They found that this alloy showed large strain hardening and compressive strength up to 2004 MPa with a 32.7% compressive plasticity [6]. Munitz et al. reported the impact of heat treatment of AlCoCrFeNi HEA, in which the BCC (Body-centered cubic) matrix transformation occurred between 650 and 975 °C. This transformation led to a substantial increase in microhardness [5]. Further modification of this alloy system through the addition of titanium, leading to $AlCoCrFeNiTi_X$ (x = molar ratios), was found to be promising for wear protection [1]. Further, AlCoCrFeNi HEA solidified with dendritic and interdendritic microstructures due to elemental segregation. Dendritic segregation regions were found to be Al- and Ni-rich, while interdendritic areas were Fe- and Cr-rich, and the distribution of Co was uniform. Body-centered cubic (BCC) Fe and Cr precipitates, and B2 (ordered BCC) Al- and Ni-rich matrices were observed in previous studies [2,4,6,8,9]. Most of these studies are based on material fabricated through processes such as casting

and arc melting. Unlike these early studies, laser metal deposition (LMD) was implemented in this study.

LMD is capable of fabricating freeform three-dimensional metallic components [10-12] and has been used to fabricate several HEAs [12-16]. Chen et al. fabricated $Al_xCoFeNiCu_{1-x}$ (x = 0.25, 0.5 and 0.75 atom %, respectively) HEAs using elemental powders on the AISI 304 substrate. They reported an increase in hardness with an increase in aluminum content [16]. He et al. used laser cladding to produce $FeCoCrNiAlTi_x$ (x = 0, 0.25, 0.5, 0.75 and 1 atom %, respectively) coating on Q253 steel through the use of elemental powders. Addition of titanium was observed to improve the hardness and wear resistance of the HEA [15]. Similarly, FeCoCrAlCu HEA coating by laser cladding demonstrated good wear resistance under a dry sliding condition [17].

In this paper, the feasibility of coating an AlCoCrFeNi HEA on an AISI 304 stainless steel substrate was investigated. Sole LMD fabrication of AlCoCrFeNi HEA components is very costly due to the need for high-purity (i.e., 99.9%) raw powders of elements such as Co, Cr and Ni. AISI 304 stainless steel, on the other hand, is a low-cost structural material. However, AISI 304 is a soft material with low wear resistance. It is widely used in industrial facilities, transportation equipment and architectural applications. Therefore, by coating AlCoCrFeNi HEA on AISI 304, it can enhance the hardness of AISI 304 structures. This combination of materials could facilitate fabrication of components for applications that require both hardness and wear resistance.

However, direct coating of AlCoCrFeNi HEA on AISI 304 is difficult due to the change in chemistry, thermal expansion and residual stress of the dissimilar materials. For example, the measured coefficient of thermal expansion (CTE, 10^{-6}/K) for

AlCoCrFeNi HEA was 9.03 (293–303 K), 12.47 (368–378 K) and 13.54 (423–773 K) [18]. However, the CTE values of AISI 304 were 14.7 (293 K), 16.3 (400 K), 19.5 (700 K) and 20.2 (800 K) [19]. Harihar et al. observed crack formation at the bottom of an AlCoCrFeNi deposit when deposited on an AISI 304 substrate. Due to the brittleness of the deposited material, the deposit broke off from the AISI 304 substrate easily [12]. An extensive network of cracks occurred when a TiVCrAlSi HEA was cladded on a Ti-6Al-4V substrate. This was attributed to the difference between the thermal expansion coefficients and residual stresses associated with the high cooling rate in laser cladding [20].

Therefore, to facilitate the dissimilar material bond, an intermediate layer was necessary and could accommodate the residual stresses and variation in chemistry change [10,20,22]. Intermediate layers of Fe/Cr/V were used between AISI 316 stainless steel and Ti6Al4V to facilitate a similar material bond [10]. Currently, there are few studies available identifying the viable intermediate layer between AlCoCrFeNi HEA and AISI 304. In this study, an attempt was made to coat the equiatomic AlCoCrFeNi HEA on the AISI 304 substrate using LMD. The objective was to obtain a strong bond between the two materials. We first demonstrated the issues with direct-coating the HEA onto the substrate. Then we proposed a candidate intermediate material and proved its viability.

2. MATERIALS AND METHODS

Elemental powders of gas-atomized aluminum (Al), chromium (Cr), cobalt (Co), nickel (Ni) and iron (Fe) from Atlantic Equipment Engineers Inc. were used as precursor

materials. These powders, weighed in required ratios, were mixed using a Turbula mixer (Glen Mills Inc., Clifton, NJ, USA) for 1 h to obtain homogeneous blends. Commercially procured AISI 304 bar stock (dimensions: 2.75 inch × 2 inch × 0.25 inch) was used as the substrate material for the deposition. The particle size distribution of the elemental powders stated by the producer is as tabulated in Table 1. Elemental analysis of the elemental powders is listed in Table 2. Elemental compositions (atom %) of the as-blended $CoFe_2Ni$ intermediate layer and AlCoCrFeNi alloy are given in Table 3.

Table 1. Particle size distribution of the precursor elemental powders.

Materials	US Standard Mesh
Al	−100
Co	−100/+325
Cr	−100
Fe	−100
Ni	−100/+325

Table 2. Elemental analysis (atom %) of elemental powders as provided by the manufacturer.

Materials	Al	Cr	Si	Fe	C	Ni	Co	S	Ca
Al	0.88	-	0.07	0.05	-	-	-	-	-
Co	-	-	-	0.002	-	<0.001	~0.99	-	0.001
Cr	-	0.89	-	0.02	0.09	-	-	-	-
Fe	-	-	-	0.99	0.01	-	-	-	-
Ni	-	-	-	0.01	0.05	0.92	-	0.02	-

Table 3. Nominal compositions (atom %) of $CoFe_2Ni$ and AlCoCrFeNi alloy powder blends.

Alloy	Al	Co	Cr	Fe	Ni
$CoFe_2Ni$	0	25	0	50	25
AlCoCrFeNi	20	20	20	20	20

The laser deposition process was performed in an LMD system whose schematic representation is as seen in Figure 1a. The heat source was a 1 kW continuous-wave YAG fiber laser (IPG Photonics, Oxford, MA, USA) with a 2 mm beam diameter. The powders were fed using a vibration X2 powder feed system procured from Powder Motion Labs. The powder was introduced into the melt pool through an alumina tube. A computer numerical control (CNC) table was used to facilitate the movement during the deposition. Argon gas was used to ensure an inert atmosphere and act as a carrier gas to deliver the powder mixture to the melt pool.

In the current setup, the 2 mm spot size is insufficient to attain a large capture efficiency of the powder. This is due to the scatter of the powder flow out of the powder feed tube. This scatter was suspected to vary with individual precursor powder. Therefore, in order to obtain as-deposited compositions that are close to as-blended compositions, the capture efficiency during the deposition process needed to be increased. A trochoidal toolpath (shown in Figure 1b) was designed to create a large enough melt pool to improve capture efficiency during deposition. This toolpath was inspired by "weave"-style toolpaths that are commonly used in welding.

The AISI 304 substrates were cleaned with acetone to remove the impurities such as dirt and oil from the surface. A preheating scan was conducted by running the laser across the substrate surface. To ensure a successful start, the power of the initial five layers of the deposition was carried out at 750 W and 8.5% (3.36 g/min) powder feed rate. The remainder of the deposit was run at a power level of 550 W and 8.5% (3.36 g/min) powder feed rate. The thickness of each layer is 1 mm.

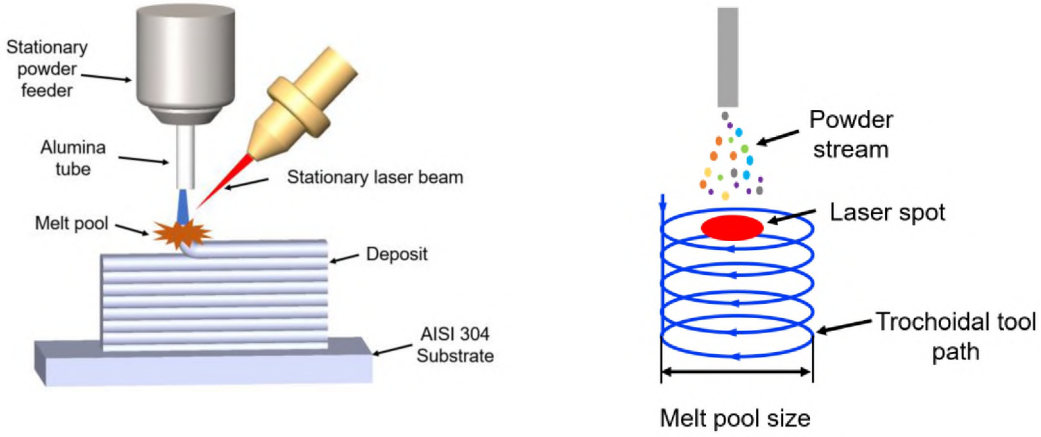

Figure 1. Schematic of the experimental setup, (a) laser metal deposition (LMD) system and (b) the trochoidal tool path.

After laser deposition, vertical transverse sections of the specimens were cut using a wire electric discharge machine (Hansvedt Industries Inc., Rantoul, IL, USA) and mounted in Bakelite for polishing and etching. The metallographic specimens were first ground using 240, 400, 600 and 800 grit silicon carbide papers and then polished using 15 µm, 9 µm and 3 µm diamond suspensions. The final step of polishing involved 0.05 µm colloidal silica suspension. To reveal the microstructure, the electrolytic etching was carried out in the nitric acid solution (70 mL nitric acid, 30 mL distilled water) at 5 V for 5 seconds. Scanning electron microscopy (SEM), energy dispersive X-ray spectroscopy (EDS) and electron backscatter diffraction (EBSD) were performed on Helios Nanolab 600 SEM (Thermo Fisher Scientific, Waltham, MA, USA). The SEM image was acquired by an Everhart-Thornley detector. The EDS element was analyzed by the factory standardizations provided in the Aztec software. The EBSD step size was selected to be 2.5 µm. EBSD data acquisition and analysis were conducted using Aztec and

Channel 5 software, respectively. Grain size was measured by the line intercept method, and the misorientation angle was 10°. Optical microscopy images were collected using a Hirox optical microscope. X-ray diffraction patterns were collected using Philips X'pert MRD using Cu anode. The Vickers hardness was measured using a Struers Duramin hardness tester (Struers Inc., Cleveland, OH, USA) at a 9.8 N load and a 10 s load duration. The reported hardness results were the average of three indentations.

3. RESULTS AND DISCUSSION

3.1. DIRECT COATING OF ALCOCRFENI HEA ON AISI 304 SUBSTRATE

The direct LMD of the AlCoCrFeNi HEA on the AISI 304 substrate will be discussed first. Figure 2a shows a portion of the vertical transverse section of the HEA deposit near the AISI 304 substrate. An area close to the crack zone, as marked in the dashed-line box, is shown in Figure 2b with high magnification. A network of cracks, mostly transverse and horizontal in orientation, were found to be prevalent. Cracking occurred at the bottom of this HEA deposit. This could be attributed to the mismatch between the thermal expansion coefficients. The CTE of this HEA was reported to be 9.03 (10^{-6}/K, 293–303 K) while the value of AISI 304 was 14.7 (10^{-6}/K, 293 K) [18,19].

The elemental composition distribution along the interface between the HEA deposit and the AISI 304 substrate is shown in Figure 3. At the bottom of the melted metal, the composition mixing was significant during the laser deposition process (see Figure 3). The bottom of the deposit had high susceptibility of cracking in the transverse cross-section, as seen in Figure 2.

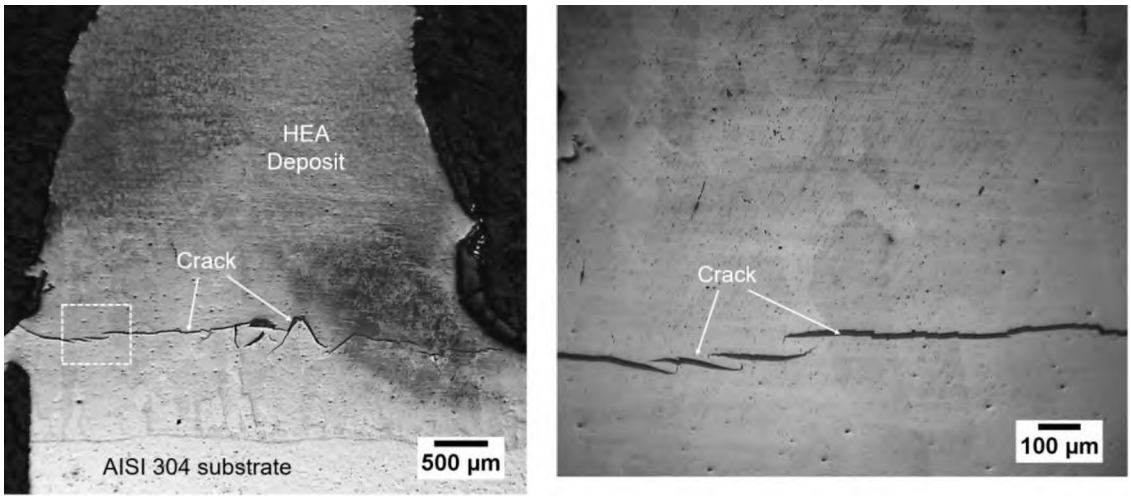

(a) (b)

Figure 2. (a) Optical microscopy image of the vertical transverse cross-section of direct AlCoCrFeNi HEA coating on AISI 304 substrate, (b) a high-magnification view of the dashed–line-boxed area in (a).

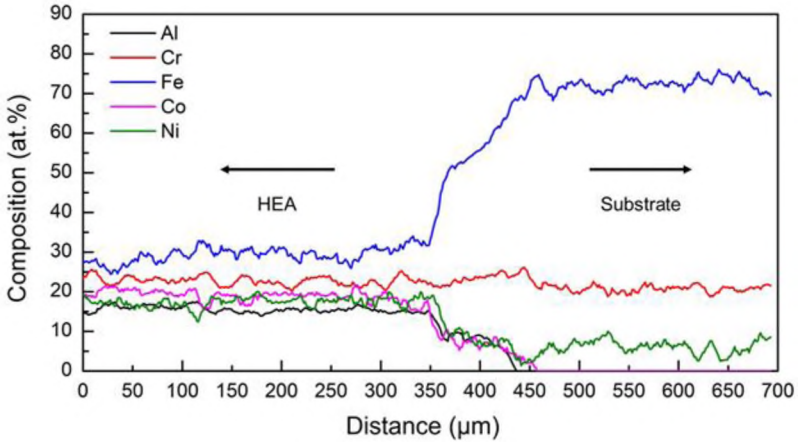

Figure 3. Elemental composition distribution along the interface between the AISI 304 substrate and the HEA deposit.

The variation in Vickers hardness across the HEA–AISI 304 direct coating is presented in Figure 4. The average Vickers hardness of the HEA deposits was 412 HV, while that of the substrate was 161 HV. Since the coefficients of thermal expansion are

mismatched between HEA and the substrate, residual stresses were developed during the laser deposition process. The AISI 304 substrate had a high elongation rate from 28% to 50% in the temperature range of 300–500 °C [23]. However, the tensile elongations of the AlCoCrFeNi HEA were 1% (as-cast condition) and 11.7% (after heat treatment) [4]. A difference in ductility exists between the substrate and the HEA. Having an intermediate material to bridge these differences was deemed necessary.

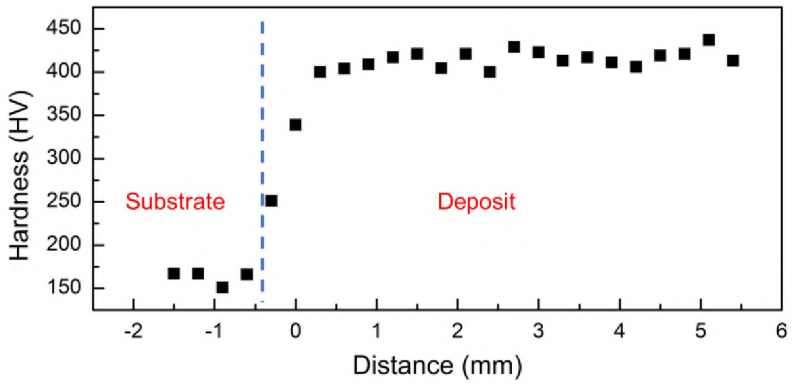

Figure 4. Vickers hardness profile of the direct coating of the AlCoCrFeNi alloy on AISI 304 stainless steel.

3.2. A NEW TRANSITION ROUTE

A blend of Fe, Co and Ni powders was selected as the candidate intermediate material. Since they are among the constituents of the AlCoCrFeNi HEA, no special procurement was needed. A Fe–Co–Ni ternary phase diagram at 1073 K compiled from experimental data is shown in Figure 5 [24]. Fe, Ni and Co have excellent mutual solubility, and no brittle intermetallic phases are expected. From the phase diagram, an atomic composition ratio of Fe, Ni and Co of 50%, 25% and 25%, respectively, was chosen. The selected ratio is expected to bridge the material composition gap between the

AlCoCrFeNi HEA and AISI 304. This new transition route, AISI 304 substrate → $CoFe_2Ni$ intermediate layer → AlCoCrFeNi HEA, was then carried out and characterized.

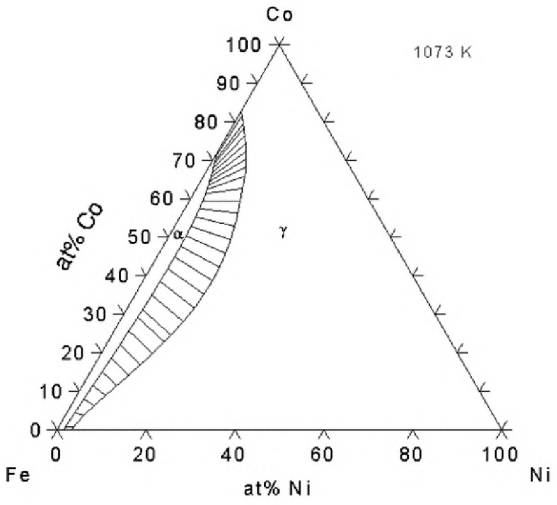

Figure 5. Ternary alloy phase diagram of Fe–Co–Ni at 1073 K [24].

3.3. AlCoCrFeNi HEA-AISI 304 WITH AN INTERMEDIATE LAYER

3.3.1. Microstructure. The $CoFe_2Ni$ intermediate layer was coated on the AISI 304 substrate using premixed elemental powder. Then, the AlCoCrFeNi HEA was coated on the intermediate layer by LMD. The intermediate layer composition was theorized to avoid the formation of intermetallic compounds and bridge the large gap in strength differences. Figures 6a and 6b show the optical images of etched surfaces of transverse sections of these deposits. Unlike the HEA–AISI 304 direct coating, no apparent cracks were observed, which indicated an improvement in bonding. However, issues of

microporosity persisted. A dendrite microstructure was observed along the interface between the intermediate layer and the HEA.

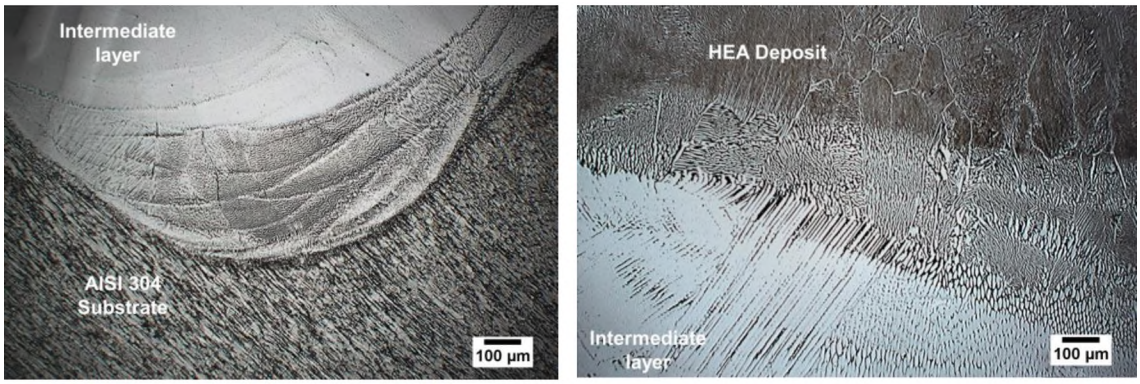

(a) (b)

Figure 6. The optical microstructure of (a) the $CoFe_2Ni$ intermediate layer and the AISI 304 substrate and (b) the AlCoCrFeNi alloy deposit and the $CoFe_2Ni$ intermediate layer.

A high-magnification secondary electron image of the AlCoCrFeNi HEA deposit is shown in Figure 7, where a two-phase dendritic microstructure was observed. The area fraction of the dendritic microstructure was ~52%, while the interdendritic area fraction was ~48%. The interdendritic region is named A, and the dendritic region is named B. The mean elemental compositions of A and B (average from three arbitrary points) were analyzed by EDS, and the results are listed in Table 4. It is shown that the atomic percentages of Al and Ni were ~29% in A and ~41% in B. The percentages of Fe and Cr were ~54 atom % in A and 43 atom % in B. These results indicate that Fe and Cr were rich in A, while Al and Ni were rich in B. The composition of Co did not show evident differences between A and B. The mixing enthalpies between Fe–Cr, Fe–Ni, Fe–Co, Fe–Al, Cr–Ni, Cr–Co, Cr–Al, Ni–Co, Ni–Al and Co–Al were −1, −2, −1, −11, −7, −4, −10,

0, −22 and −19 kJ/mol, respectively [6,25]. The mixing enthalpy of Al and Ni was higher than other pairs, which indicated that Al and Ni tended to form atomic pairs and segregate. Similar results have been reported for the AlCoCrFeNi HEA, with this microstructure being attributed to the spinodal decomposition [2,4-6,9].

Table 4. Elemental compositions analyzed by energy dispersive X-ray spectroscopy (EDS)of the AlCoCrFeNi HEA shown in Figure 7.

Elements (atom %)	Al	Co	Cr	Fe	Ni
A	16.2	16.8	23.4	30.2	13.4
B	23.5	15.7	19.4	24.2	17.2

XRD was used to identify the crystal structures of the intermediate layers and the HEA. A transition of the crystal structure was observed from the AISI 304 substrate to the AlCoCrFeNi alloy. The XRD patterns of the AISI 304 substrate, the $CoFe_2Ni$ intermediate layer and the AlCoCrFeNi alloy are shown in Figure 8. The present phases and the corresponding crystallographic information are summarized in Table 5. The peak patterns of FCC were observed in the $CoFe_2Ni$ intermediate layer, while BCC peak patterns were detected in the AlCoCrFeNi alloy. Löbel et al. found BCC and B2 (ordered BCC) phases in $AlCoCrFeNiTi_x$ ($x = 0$) when fabricated via arc melting [1]. A similar result was reported by Shiratori et al., when casting was employed to produce an AlCoCrFeNi HEA [26]. Due to the same basic lattice structure and lattice parameters, the B2 ordered structure is very hard to detect from XRD, as the peak patterns of B2 and BCC are the same [2,9]. However, the evidence of the existence of the B2 phase was found from the EDS analysis above. Previously, an AlCoCrFeNi HEA was reported to also contain the FCC crystal structure with preheating or post-heat treatment [5,13,26].

The FCC structure was not found in this work, which could be because the high cooling rate during LMD inhibited the formation of the FCC crystal structure [5,13,26].

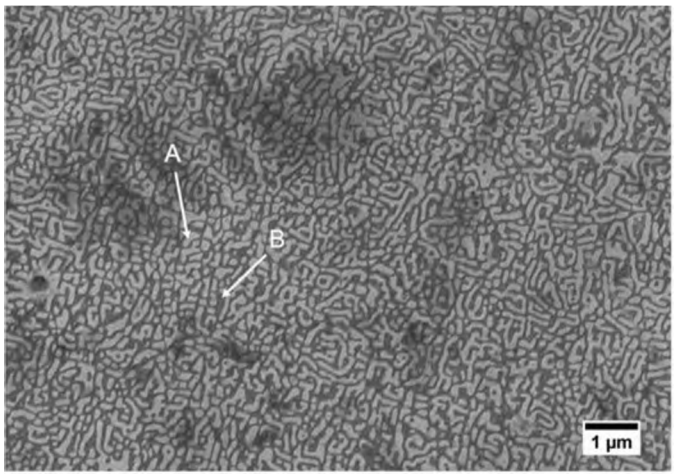

Figure 7. Secondary electron image of the AlCoCrFeNi HEA microstructure at a magnification of 10000.

The evolution in chemistry from the intermediate layer to the substrate was characterized by an EDS line scan first. The quantitative results are shown in Figure 9a. The EDS measured results of the AISI 304 substrate (Cr: ~18–19 atom %, Fe: ~70–72 atom %, Ni: ~9–10 atom % in Figure 9a) did not vary from the nominal AISI 304 elemental compositions. Mn (~1–2 atom %) was detected in the AISI 304 substrate by EDS but is not shown in Figure 9. The percentages of Co (~17–22 atom %) and Ni (~21–23 atom %) reduced, while the Fe (~54–56 atom %) content increased from the intermediate layer to the AISI 304 substrate. A small amount of Cr (~3–5 atom %) was present in the intermediate layer, because the substrate was mixed with the intermediate layer. The composition distribution from the HEA to the intermediate layer is shown in Figure 9b. The constituents of the AlCoCrFeNi HEA were detected by EDS (Al: ~16–17

atom %, Co: 19–20 atom %, Cr: ~17 atom %, Fe: ~25 atom %, Ni: ~20–21 atom %). The difference between the as-blended (20 atom %) and as-deposited aluminum (~16–17 atom %) percentages is suspected to be a consequence of inconsistency in capture efficiencies of the constituent powders, and evaporation due to differences in melting point. Al and Cr were present in the intermediate layer as seen in Figure 9b, and their total content was ~4–5 atom %.

Table 5. Summary of phases detected by XRD analysis for AISI 304, $CoFe_2Ni$ and the AlCoCrFeNi HEA.

Alloy	Lattice	Structure	Space Group	Lattice Parameter (Å)
AISI 304	FCC	Cu	Fm-3m (225)	3.5911
	BCC	Fe	Im-3m (229)	2.87
$CoFe_2Ni$	FCC	Cu	Fm-3m (225)	3.5911
AlCoCrFeNi HEA	BCC	W	Im-3m (229)	2.876

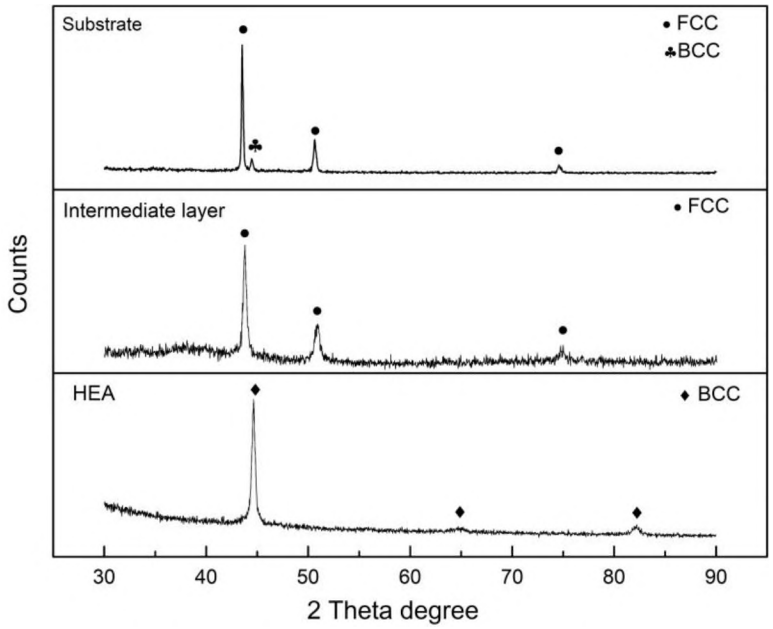

Figure 8. XRD pattern of the AISI 304 substrate, the $CoFe_2Ni$ intermediate layer and the AlCoCrFeNi HEA.

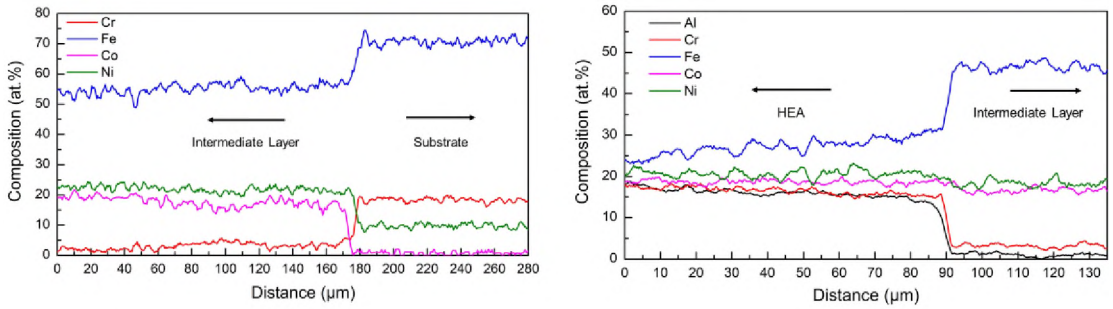

(a) (b)

Figure 9. Elemental composition distribution along the boundary, (a) $CoFe_2Ni$ intermediate layer and AISI 304 substrate and (b) AlCoCrFeNi HEA and $CoFe_2Ni$ intermediate layer.

3.3.2. Electron Backscatter Diffraction. Figure 10a shows the inverse pole figure (IPF) map obtained from the bottom of the HEA section of the specimen. The measured area was approximately 3.4 mm × 1.2 mm of the cross-section parallel to the build direction (BD), which spanned from the left to the right of the specimen. The difference in color indicates the different crystallographic orientations. From Figure 10a, the overall constitution can be classified into two zones—the edge zone (1 and 3) and the middle zone (2). In areas 1 and 3, the grains were observed to be elongated along the build direction (see 1 and 3 in Figure 10a). The distributions of the intercept lengths (using 100 horizontal lines) in different areas are depicted Figure 10b. The median linear intercept for areas 1 and 3 was 72.5 μm, while it was 127.5 μm for area 2. From the linear intercept distribution of area 2, 25% of the intercept values were greater than 300 μm, whereas only 14% of the intercept values were above 300 μm for areas 1 and 3. This grain morphology is likely to be a consequence of deposition toolpath and variation in cooling rate at edges and in the middle [27,28]. Figures 10c and 10d show the {100}, {110} and {111} pole figures of different areas, which give the distribution of the pole

density along the build direction. The pole figure of the areas 1 and 3 (Figure 10c) suggests that the orientations of the grains were close to the <100> direction. However, the grains were random in orientation and did not appear with obvious texture in area 2 (Figure 10d). Further study is necessary to investigate the impact of this toolpath on the grain morphology.

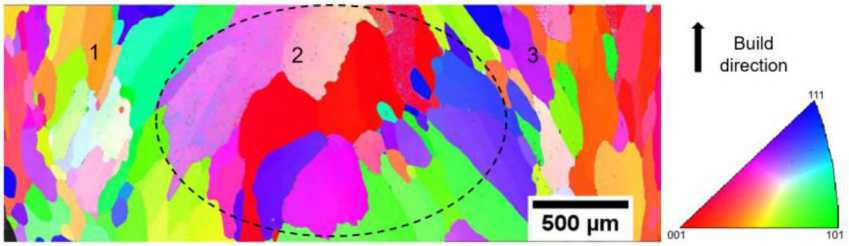

(a)

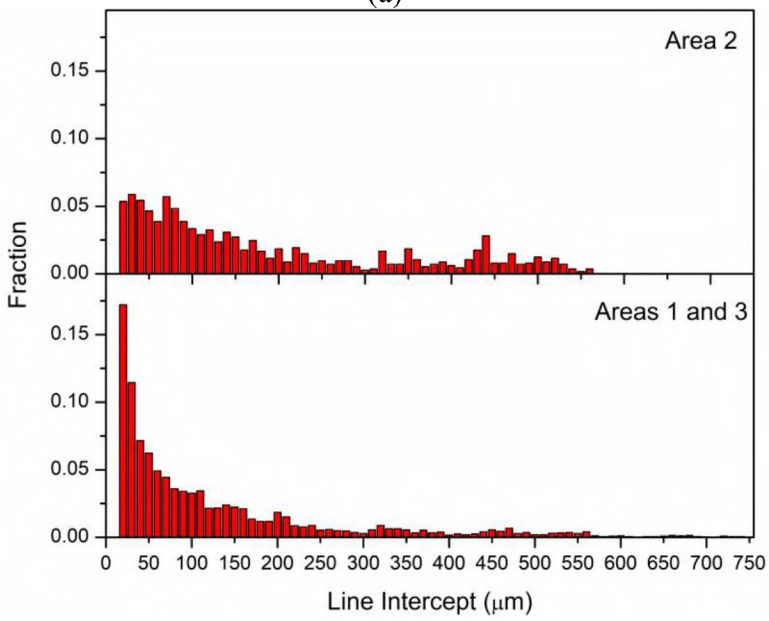

(b)

Figure 10. (a) Inverse pole figure (IPF)IPF map of the bottom of the HEA section in the specimen; the measured region was approximately 3.4 mm × 1.2 mm, from the left to the right side in the cross-section parallel to the build direction (BD); (b) distribution of the intercept length of grains with the bin size of 10 µm; (c) pole figure of areas 1 and 3; and (d) pole figure of area 2 in (a).

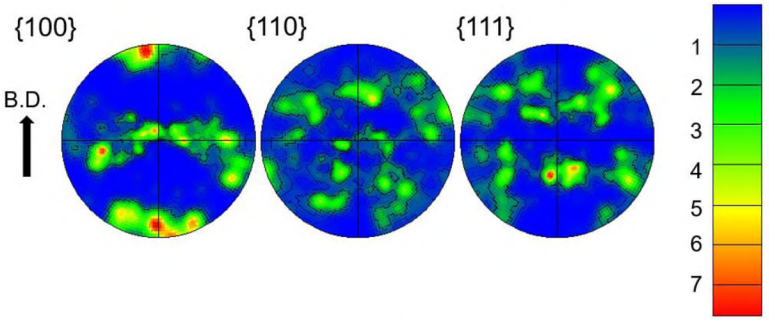

(c)

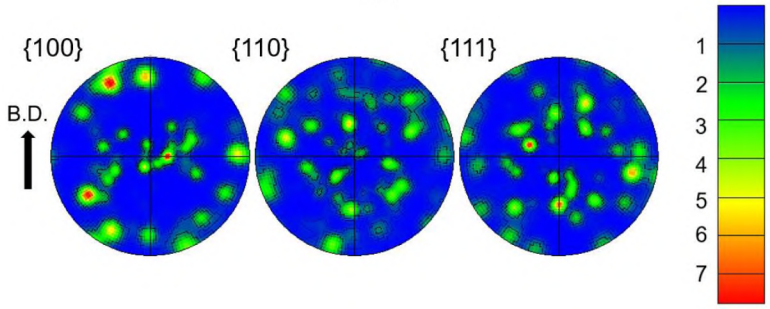

(d)

Figure 10. (a) Inverse pole figure (IPF)IPF map of the bottom of the HEA section in the specimen; the measured region was approximately 3.4 mm × 1.2 mm, from the left to the right side in the cross-section parallel to the build direction (BD); (b) distribution of the intercept length of grains with the bin size of 10 μm; (c) pole figure of areas 1 and 3; and (d) pole figure of area 2 in (a). (cont.)

3.3.3. Vickers Hardness Analysis. Figure 11 gives the Vickers hardness distribution of the AlCoCrFeNi HEA deposited on the AISI 304 substrate with the $CoFe_2Ni$ intermediate layer. The Vickers hardness of the $CoFe_2Ni$ intermediate layer was around the 275 HV, which could be attributed to the solid solution strengthening. Table 6 lists the Vickers hardness of the AlCoCrFeNi HEA, annealed AISI 304, aged Inconel 625, and annealed duplex steel SAF 2205 [29,31]. The average Vickers hardness of the HEA deposit was in the range of 418 HV, because of the second-phase strengthening [4].

According to the XRD results, the AISI 304 substrate and the $CoFe_2Ni$ intermediate layer had an FCC structure, while the AlCoCrFeNi HEA had a BCC structure. The transition from FCC to BCC structure is also expected to enhance the

hardness. The high hardness is expected to correlate with good performance in strength and wear resistance [1,16].

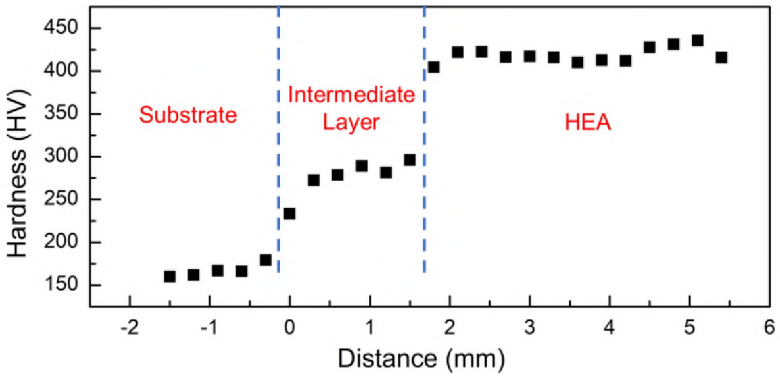

Figure 11. Vickers hardness profile of the AISI 304 substrate—AlCoCrFeNi HEA with the $CoFe_2Ni$ intermediate layer.

Table 6. Vickers hardness of various alloys.

Alloy	Hardness (HV)	Reference
AlCoCrFeNi HEA	418	This work
AISI 304 annealed	188	[29]
Inconel 625 aged	225	[30]
Duplex steel SAF 2205 annealed	290	[31]

4. CONCLUSIONS

An AlCoCrFeNi HEA was coated on an AISI 304 substrate by laser metal deposition (LMD) technology. The coating on the substrate without and with the intermediate layer was characterized and discussed. The main conclusions are as follows:

Cracking was found to be prominent when the AlCoCrFeNi HEA was directly coated on the AISI 304 substrate due to the compositional change between HEA and the substrate.

Using an intermediate layer of $CoFe_2Ni$ improved the bond. The incorporation of the intermediate layer successfully eliminated crack formation in the deposit.

XRD patterns revealed a transition of crystal structure from FCC in the AISI 304 substrate to BCC in the AlCoCrFeNi alloy. The evidence of a B2 phase in the AlCoCrFeNi HEA was also found in the EDS analysis results.

The AlCoCrFeNi alloy fabricated by LMD was found to have an average hardness of 418 HV, while the $CoFe_2Ni$ intermediate layer had an average hardness of 275 HV.

ACKNOWLEDGMENTS

The authors gratefully acknowledge the financial support from NSF (National Science Foundation) grants CMMI-1547042 and CMMI-1625736. The support from the Intelligent Systems Center (ISC) and Materials Research Center (MRC) for the help in sample preparation and materials characterization is also appreciated.

REFERENCES

[1] M. Löbel *et al.*, "Influence of Titanium on Microstructure, Phase Formation and Wear Behaviour of AlCoCrFeNiTix High-Entropy Alloy," *Entropy*, vol. 20, no. 7, p. 505, Jul. 2018.

[2] I. Kunce, M. Polanski, K. Karczewski, T. Plocinski, and K. J. Kurzydlowski, "Microstructural characterisation of high-entropy alloy AlCoCrFeNi fabricated by laser engineered net shaping," vol. 648, pp. 751–758, 2015.

[3] T. Fujieda et al., "First demonstration of promising selective electron beam melting method for utilizing high-entropy alloys as engineering materials," Mater. Lett., vol. 159, pp. 12–15, Nov. 2015.

[4] Z. Tang et al., "Tensile ductility of an AlCoCrFeNi multi-phase high-entropy alloy through hot isostatic pressing (HIP) and homogenization," Mater. Sci. Eng. A, vol. 647, pp. 229–240, 2015.

[5] A. Munitz, S. Salhov, S. Hayun, and N. Frage, "Heat treatment impacts the micro-structure and mechanical properties of AlCoCrFeNi high entropy alloy," J. Alloys Compd., vol. 683, pp. 221–230, Oct. 2016.

[6] Y. P. Wang, B. S. Li, M. X. Ren, C. Yang, and H. Z. Fu, "Microstructure and compressive properties of AlCrFeCoNi high entropy alloy," Mater. Sci. Eng. A, vol. 491, no. 1–2, pp. 154–158, Sep. 2008.

[7] Y. Zhang et al., "Microstructures and properties of high-entropy alloys," Prog. Mater. Sci., vol. 61, pp. 1–93, Apr. 2014.

[8] W.-R. Wang, W.-L. Wang, S.-C. Wang, Y.-C. Tsai, C.-H. Lai, and J.-W. Yeh, "Effects of Al addition on the microstructure and mechanical property of AlxCoCrFeNi high-entropy alloys," Intermetallics, vol. 26, pp. 44–51, Jul. 2012.

[9] A. Manzoni, H. Daoud, R. Völkl, U. Glatzel, and N. Wanderka, "Phase separation in equiatomic AlCoCrFeNi high-entropy alloy," Ultramicroscopy, vol. 132, pp. 212–215, Sep. 2013.

[10] W. Li et al., "Ti-Fe intermetallics analysis and control in joining titanium alloy and stainless steel by Laser Metal Deposition," J. Mater. Process. Technol., vol. 242, pp. 39–48, Apr. 2017.

[11] W. U. H. Syed, A. J. Pinkerton, Z. Liu, and L. Li, "Coincident wire and powder deposition by laser to form compositionally graded material," Surf. Coatings Technol., vol. 201, no. 16–17, pp. 7083–7091, May 2007.

[12] H. R. Sistla, J. W. Newkirk, and F. Frank Liou, "Effect of Al/Ni ratio, heat treatment on phase transformations and microstructure of AlxFeCoCrNi2−x (x = 0.3, 1) high entropy alloys," Mater. Des., vol. 81, pp. 113–121, Sep. 2015.

[13] R. Wang, K. Zhang, C. Davies, and X. Wu, "Evolution of microstructure, mechanical and corrosion properties of AlCoCrFeNi high-entropy alloy prepared by direct laser fabrication," J. Alloys Compd., vol. 694, pp. 971–981, Feb. 2017.

[14] H. Zhang, Y. Pan, and Y.-Z. He, "Synthesis and characterization of FeCoNiCrCu high-entropy alloy coating by laser cladding," Mater. Des., vol. 32, no. 4, pp. 1910–1915, Apr. 2011.

[15] B. He et al., "The Phase Evolution and Property of FeCoCrNiAlTix High-Entropy Alloying Coatings on Q253 via Laser Cladding," Coatings, vol. 7, no. 10, p. 157, Sep. 2017.

[16] X. Chen et al., "Fabrication and Characterization of AlxCoFeNiCu1−x High Entropy Alloys by Laser Metal Deposition," Coatings, vol. 7, no. 4, p. 47, Mar. 2017.

[17] S. Zhang, C. L. Wu, J. Z. Yi, and C. H. Zhang, "Synthesis and characterization of FeCoCrAlCu high-entropy alloy coating by laser surface alloying," Surf. Coatings Technol., vol. 262, pp. 64–69, Jan. 2015.

[18] H.-P. Chou, Y.-S. Chang, S.-K. Chen, and J.-W. Yeh, "Microstructure, thermophysical and electrical properties in AlxCoCrFeNi ($0 \leq x \leq 2$) high-entropy alloys," Mater. Sci. Eng. B, vol. 163, no. 3, pp. 184–189, Jul. 2009.

[19] R. K. Shiue, C. T. Chang, M. C. Young, and L. W. Tsay, "The effect of residual thermal stresses on the fatigue crack growth of laser-surface-annealed AISI 304 stainless steel: Part I: computer simulation," Mater. Sci. Eng. A, vol. 364, no. 1–2, pp. 101–108, Jan. 2004.

[20] C. Huang, Y. Zhang, R. Vilar, and J. Shen, "Dry sliding wear behavior of laser clad TiVCrAlSi high entropy alloy coatings on Ti–6Al–4V substrate," Mater. Des., vol. 41, pp. 338–343, Oct. 2012.

[21] Y. Li, Y. Shen, C.-H. Hung, M. C. Leu, and H.-L. Tsai, "Additive manufacturing of Zr-based metallic glass structures on 304 stainless steel substrates via V/Ti/Zr intermediate layers," Mater. Sci. Eng. A, vol. 729, pp. 185–195, Jun. 2018.

[22] W. Li et al., "Fabricating Functionally Graded Materials by Ceramic On-Demand Extrusion with Dynamic Mixing," in Proceedings of the 29th Annual International Solid Freeform Fabrication Symposium, 2018, pp. 1087–1099.

[23] R. K. Desu, H. Nitin Krishnamurthy, A. Balu, A. K. Gupta, and S. K. Singh, "Mechanical properties of Austenitic Stainless Steel 304L and 316L at elevated temperatures," J. Mater. Res. Technol., vol. 5, no. 1, pp. 13–20, Jan. 2016.

[24] A. F. Guillermet, "Assessing the thermodynamics of the Fe CO Ni system using a calphad predictive technique," Calphad, vol. 13, no. 1, pp. 1–22, Jan. 1989.

[25] Z. Tang et al., "Aluminum Alloying Effects on Lattice Types, Microstructures, and Mechanical Behavior of High-Entropy Alloys Systems," JOM, vol. 65, no. 12, pp. 1848–1858, Dec. 2013.

[26] H. Shiratori et al., "Relationship between the microstructure and mechanical properties of an equiatomic AlCoCrFeNi high-entropy alloy fabricated by selective electron beam melting," Mater. Sci. Eng. A, vol. 656, pp. 39–46, Feb. 2016.

[27] A. Reichardt et al., "Development and characterization of Ti-6Al-4V to 304L stainless steel gradient components fabricated with laser deposition additive manufacturing," Mater. Des., vol. 104, pp. 404–413, Aug. 2016.

[28] X. Zhang, W. Cui, W. Li, and F. Liou, "Effects of tool path in remanufacturing cylindrical components by laser metal deposition," Int. J. Adv. Manuf. Technol., pp. 1–11, Oct. 2018.

[29] M. Milad, N. Zreiba, F. Elhalouani, and C. Baradai, "The effect of cold work on structure and properties of AISI 304 stainless steel," J. Mater. Process. Technol., vol. 203, no. 1–3, pp. 80–85, Jul. 2008.

[30] M. A. Shaikh, M. Ahmad, K. A. Shoaib, J. I. Akhter, and M. Iqbal, "Precipitation hardening in Inconel * 625," Mater. Sci. Technol., vol. 16, no. 2, pp. 129–132, Feb. 2000.

[31] I. Calliari, M. Zanesco, and E. Ramous, "Influence of isothermal aging on secondary phases precipitation and toughness of a duplex stainless steel SAF 2205," J. Mater. Sci., vol. 41, no. 22, pp. 7643–7649, Nov. 2006.

III. METAL ADDITIVE MANUFACTURING PARTS INSPECTION USING CONVOLUTIONAL NEURAL NETWORK

ABSTRACT

Metal additive manufacturing (AM) is gaining increasing attention from academia and industry due to its unique advantages compared to the traditional manufacturing process. Parts quality inspection is playing a crucial role in the AM industry, which can be adopted for product improvement. However, the traditional inspection process has relied on manual recognition, which could suffer from low efficiency and potential bias. This study presented a convolutional neural network (CNN) approach toward robust AM quality inspection, such as good quality, crack, gas porosity, and lack of fusion. To obtain the appropriate model, experiments were performed on a series of architectures. Moreover, data augmentation was adopted to deal with data scarcity. L2 regularization and dropout were applied to avoid overfitting. The impact of each strategy was evaluated. The final CNN model achieved an accuracy of 92.1%, and it took 8.01 milliseconds to recognize one image. The CNN model presented here can help in automatic defect recognition in the AM industry.

1. INTRODUCTION

Metal additive manufacturing (AM) processes have introduced some capabilities unparalleled by traditional manufacturing, as they realize custom-designed shape, complex features, and low materials consumptions provided by AM [1]. Laser metal

deposition (LMD) is a form of AM which accomplishes the layer-by-layer fabrication of near net-shaped components by introducing a powder stream into a high-energy laser beam. During the LMD process, a melt pool is formed by rastering the laser beam across the sample surface, and the powders are injected into the melt pool for each layer deposition. LMD has been explored for various applications, e.g., metallic component repair, surface modification, and layering gradient metal alloy on a dissimilar metal base [2-5]. Some of the control parameters involved in LMD are the laser power, laser scan speed, powder feed rate, shielding gas flow rate, and the quality of the powder feedstock. The above parameters constantly affect the parts being formed. Some studies have focused on the process parameter selection and optimization of the performance of LMD parts, but the defect presence is still high compared to traditional manufacturing [1,6-8].

The common defects present in the LMD process are crack, gas porosity, and lack of fusion (LoF), which have negatively affected the properties of LMD fabricated parts [9]. The direct joining of two dissimilar alloys is usually compromised by cracks, resulting from the residual stress, formation of brittle intermetallic compounds, or differences in thermal expansion coefficient [2,5,10]. Reichardt tried to fabricate gradient components transitioning from AISI 304L stainless steel to Ti6Al4V, but the component was halted due to cracks in the build [3]. A similar phenomenon has been observed by Huang [4] and Cui [5], which the material deposited cracked prior to analysis. Gas porosity, which is caused by the entrapment of gas from the powder feed system or the release of gas present in the powder particles [8,11,12]. This type of porosity could occur in any specific location and is nearly spherical. The gas porosities are highly undesirable because they severely degrade mechanical strength and fatigue resistance. The noticeable

effect of porosity was reported by Sun, in that 3.3% gas porosity content in the direct energy deposited AISI 4340 steel made the ductility decrease by 92.4% compared to the annealed one [8]. When there is insufficient energy in the melt pool, the resulting inability to melt the powder particles leads to LoF defects. LoF defects are usually found along boundaries between layers and in irregular shapes [6,7]. A significant LoF defect nucleated the fracture and led to poor elongation of 7% (as compared to 25%–33% elongation without LoF defects) for Ti-6Al-4V [6]. These defects contribute to the variation in the mechanical properties of each deposit, representing the main barrier to the widespread adoption of LMD technology. Therefore, this creates a need to inspect and evaluate the LMD build parts.

Traditionally, the quality of AM build parts has been manually inspected by experienced materials engineers. However, the manual inspection process is very time-consuming and labor-intensive. The machine vision-based inspection method has been investigated in the past decade. This method has been adopted for many years in facility parts identification and classification, glass products, steel strips, metal surface inspection, and agricultural product identification [13-16]. Barua used the deviation of a melt-pool temperature gradient from a reference defect-free cooling curve to predict gas porosity in the LMD process [15]. The Gaussian pyramid decomposition was applied to low the resolution and center-surround difference operation for steel strip defects detection, which would lose the image information [14]. Vision-based methods had been used the primitive attributes reflected by local anomalies to detect and segment defects. Therefore, it is necessary to tailor the algorithm according to practical image content. The

features identified by handcrafted or shallow learning techniques are not discriminative for a complex condition.

In recent years, due to the advance of deep learning, in particular, the convolutional neural network (CNN) has emerged as state of the art in terms of accuracy and robust for a number of computer vision tasks such as image classification, object detection, and segmentation [13,17-20]. Based on artificial neural networks, CNN discovers the distributed representation of its input data by transforming the low-level features into a more abstract and composite representation. LeCun proposed the LeNet model back in 1998, which included convolution layers and pooling layers for digits recognition [21]. However, restricted by the computation performance of the central processing unit (CPU) and graphics processing unit (GPU), CNN fell silent for several years. With the acceleration of GPU, AlexNet was proposed by Krizhevsky in 2012 [22], and it significantly increased the accuracy and computation speed of CNN for ImageNet dataset classification.

The significance of utilizing CNN-based methods in AM is that it can lead the trend towards real-time monitoring and quality evaluation for AM build parts. Due to the complexity of the physical process, it is difficult to predict the whole AM process via analytical models [23]. Current process monitoring in AM has been focused on statistical learning methods. Gaja investigated the ability of acoustic emission to detect and identify the defects in the LMD using a logistic regression model [24]. Supervised learning methods have been utilized to predict the porosity in the LMD process by Khanzadeh [25]. Porosity-related features were extracted from the melt-pool thermal images and then converted into vectors by transformation and rescaling. The vectors were processed by K-

nearest neighbors (K-NN), support vector machine (SVM), decision tree (DT), and linear discriminant analysis (LDA) algorithms [25]. Gobert collected the layerwise images using a high-resolution digital single-lens reflex camera [26]. The visual features were extracted and evaluated by linear SVM for binary defect classification. Likewise, metallic powder micrographs were identified by the scale-invariant feature transform method and represented by principal component analysis [27]. The statistical methods mentioned above rely on handcraft features. However, CNN-based methods can learn the features from the raw data and have achieved excellent performance in the engineering area.

Lots of researchers have applied CNN into the area of material informatics. DeCost et al. compared the classic bag of visual words [28] and CNN-based representations on the steel microstructures image classifications. The calculated image-based features were then fed to an SVM [29] classifier. The results showed that the CNN methods offered the best classification performance [30]. Similarly, Wang [20] and Chowdhury [31] successfully applied the traditional computer vision and CNN algorithms to micrography recognition tasks, which turned out that CNN represented the highest classification accuracies. Besides, CNN was adopted to link experimental microstructure with ionic conductivity for yttria-stabilized zirconia samples [32]. The CNN models have been applied in surface detection in bearing rollers, aluminum parts, and steel plates [33-37]. It was found out that CNN-based methods had better and more robust performance compared to the SVM classifiers.

The objective of this work is to explore a good CNN-based architecture with its parameters for the robust inspection of LMD fabricated parts. We will first discuss the model training and then provide performance evaluation and failure analysis.

2. ADDITIVE MANUFACTURING PARTS INSPECTION

In this section, the sample preparation, data preprocessing, data augmentation and convolutional neural network architecture is described.

2.1. SAMPLE PREPARATION

The sample preparation was performed by the researchers at Missouri S&T. The specimens were fabricated by the LMD process, which included AISI 304 stainless steel, AISI 316 stainless steel, Ti6Al4V, AlCoCrFeNi alloys, Inconel 718 alloys. A 1 kW continuous wave YAG fiber laser (IPG Photonics, Oxford, MA, USA) with a 2 mm beam diameter was used in the experiments. Table 1 lists the process parameters employed to fabricate the parts. The energy density is defined as E = Laser Power/Scan speed × Layer thickness (J/mm^2) [7,8], which is considered as a key factor affecting the quality. For the quality inspection, the samples were transverse cross-sectioned and prepared with the standard metallographic procedure. The images were captured by a Hirox (Hackensack, NJ, USA) digital microscope with a magnification of 100 and a resolution of 1600 × 1200 pixels, which provided enough information about the defects.

Table 1. Process conditions employed in the laser metal deposition.

Powder Size (μm)	Power (W)	Scan Speed (mm/s)	Layer Thickness (mm)
44–145	300–750	150–220	0.6–1

2.2. PREPROCESSING

The optical images obtained were split into blocks of size 224 × 224 pixels. After splitting, each block was screened, and 4140 image blocks were processed for the experiment. Some of the image blocks were not selected as they consisted of unusable regions, such as the mounting epoxy materials. Four types of parts quality, including good quality, crack, lack of fusion, and gas porosity are shown in Figure 1. The number of each type is given in Table 2. The samples were shuffled and randomly split into a training set (3519 samples) and a test set (621 samples). Then the training dataset was divided into training samples (2898 samples) and validation samples of 621 images.

2.3. DATA AUGMENTATION

To achieve good performance of CNN, a large number of labeled datasets are needed. As our dataset is comprised of several thousands of samples, the expansion of the dataset is necessary. Therefore, data augmentation operations [22] were applied to our original images. Each image was passed through a series transformation: random rotation from −180° to 180°, horizontal flipping, random crop, adding Gaussian noise and blur [16], as shown in Figure 2.

2.4. CONVOLUTIONAL NEURAL NETWORK (CNN) ARCHITECTURE

Several CNN models were explored using our dataset to obtain the optimal hyper-parameters of the model.

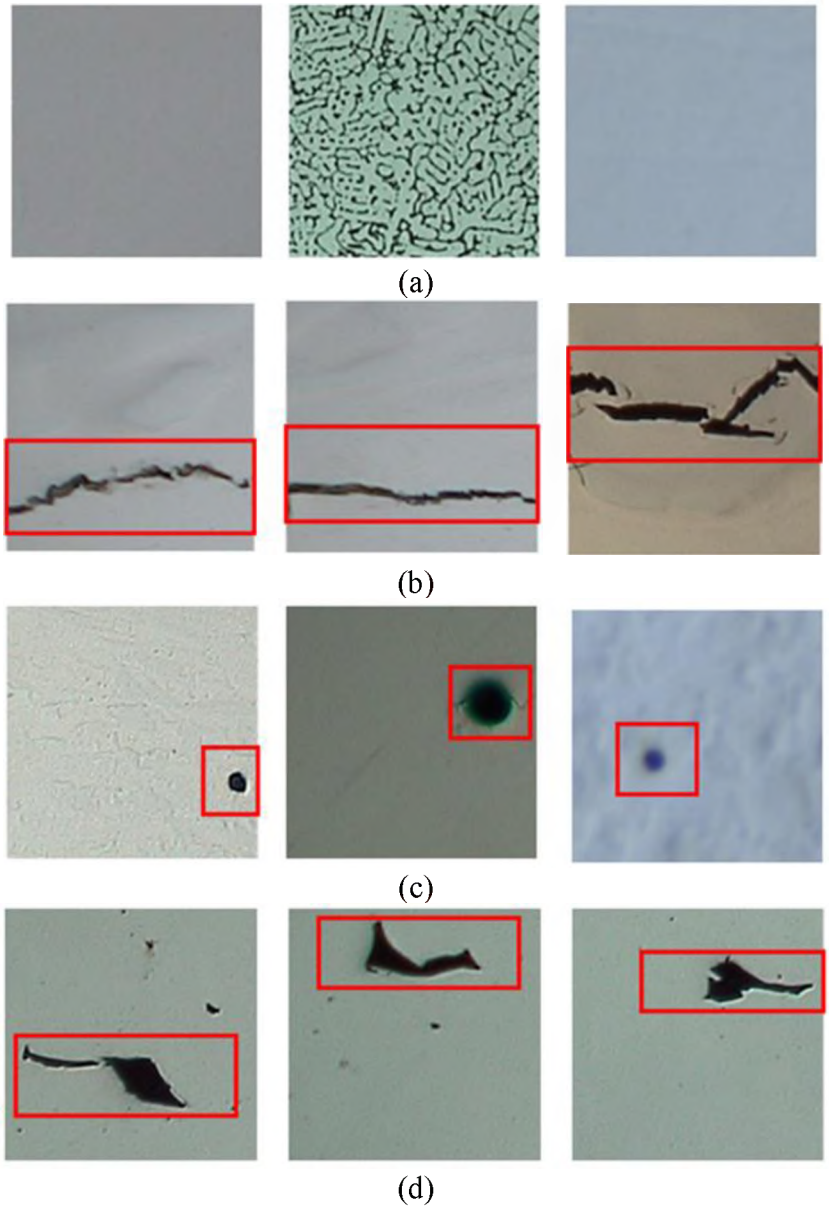

Figure 1. Examples of laser metal deposition (LMD) build parts quality optical images: (a) good quality, (b) crack, (c) gas porosity, and (d) lack of fusion with a resolution of 224 × 224 pixels.

Table 2. The number of images in each category.

Crack	Gas Porosity	Lack of Fusion	Good	Total
1013	1015	1005	1107	4140

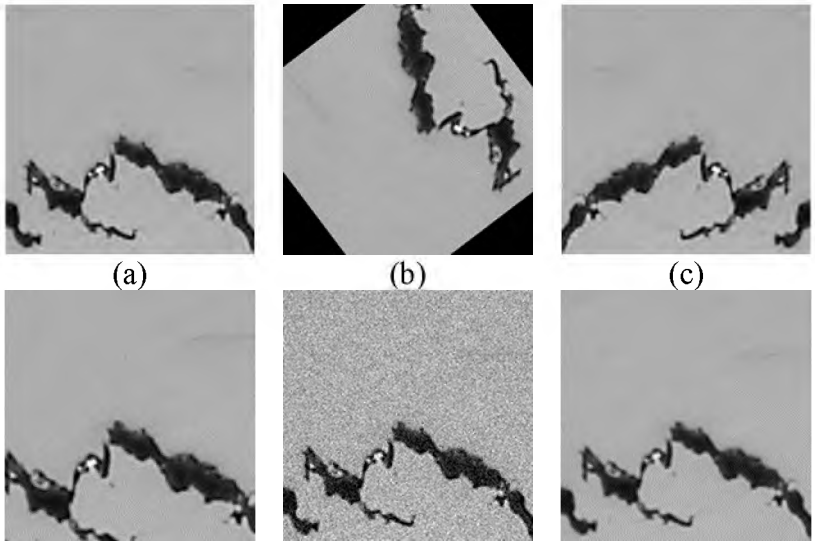

Figure 2. Data augmentation: (a) origin image, (b) rotation, (c) flipping, (d) crop, (e) adding Gaussian noise, and (f) adding blur.

Figure 3 presents the final schematic framework after several experiments. The overall schematic model is composed of feature extraction and classification. To make this work in a self-contained way, the fundamentals of our CNN model will be briefly described below. First, there were M depth images, Xm, and the images were scaled to 224 × 224 pixels with grayscales after the data augmentation process, and then fed into the first convolutional layer with the kernel size of 5 × 5 for feature extraction. In order to model non-linearities of the mapping between input and output, the Rectified Linear Unit (ReLU(x) = max (0,x)) [21]was used in each convolutional layer operation. Moreover, a max pooling layer of 2 × 2 was followed by each convolutional layer. The max pooling layer substituted the activation in a sub-region of the feature map with the maximum value in that region. The pooling layer downsampled the previous feature map.

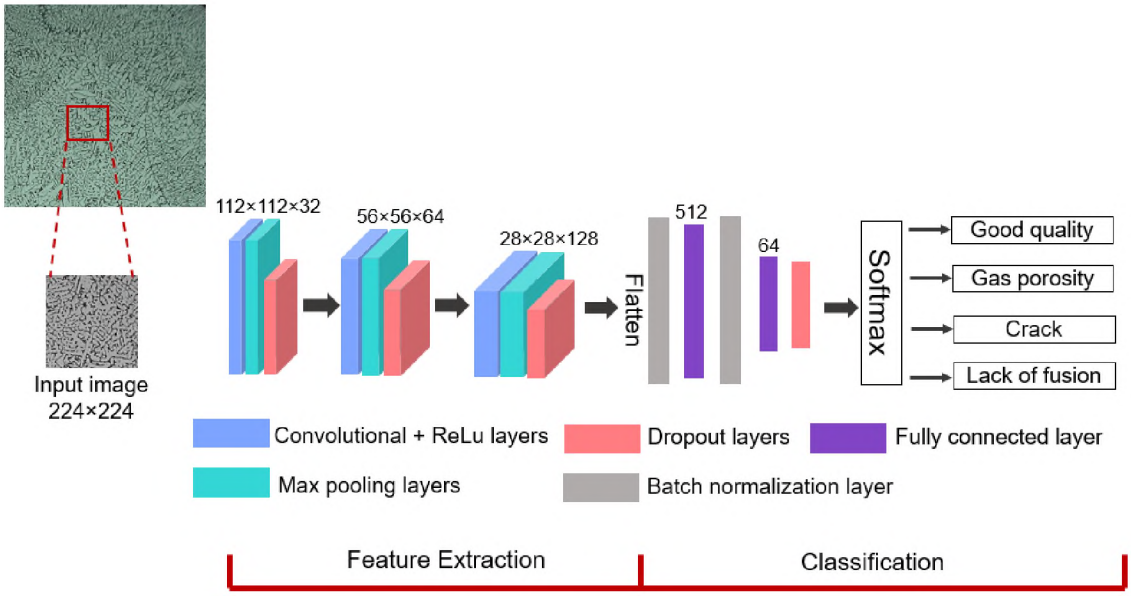

Figure 3. Final schematic of the convolutional neural network (CNN) model for autonomous recognition of LMD build parts quality.

After the feature extraction, the classification module took the 28 × 28 × 128 feature maps and flattened them as a 512 feature vector. Then fully connected (FC) layers were applied to densify the 512 feature vector to the dimension of 64 and C, where C is the number of categories in our dataset. The vectors of C dimensions ([V1, V2, …, Vc]) were computed the predicted probability of a class using Softmax function [21] Equation (1) and transformed to the output.

$$P(y_m = c \mid X_m) = \frac{\exp(V_c)}{\sum_{c=1}^{C} \exp(V_c)} \quad (1)$$

where $P(y_m = c \mid X_m)$ was the predicted probability of a sample Xm being class c.

During the training process of our CNN model, the difference between the true class and corresponding predicted class were calculated by the cross-entropy loss

function as in Equation (2). Through the optimization of parameters ω in the network, our target was to minimize the loss function for the training dataset X.

$$L(\omega) = \sum_{m=1}^{M} \sum_{c=1}^{C} y_{mc} \log(P(y_m = c \mid X_m) \quad (2)$$

2.4.1. Hyper-Parameter Tuning. The hyper-parameter is a crucial part of the CNN model and has a significant impact on the performance, such as the number of the convolutional layers, kernel size, and L2 regularization and dropout parameters. To determine the optimal hyper-parameters, several architectures were built and trained. The study of hyper-parameters was based on the training and validation datasets, which is described in Sections 3.1–3.3.

2.4.2. Training Details. The experiments in this work were conducted with one six-core AMD (Santa Clara, CA, USA) Ryzen 5 2600 processor and one Nvidia (Santa Clara, CA, USA) GeForce 1070 GPU. The code was developed in Python 3.6.8 using TensorFlow (version 1.13.1) and Keras (version 2.2.4). Some parameters were common in all experiments and are described here. A batch size of 32 and a learning rate of 1×10^{-4} were used. Each convolutional layer was followed by a max pooling layer with a filter size of 2×2 and a stride of 1. Batch normalization was used for centering and normalization of the images [40] and applied before the fully connected layers. An Adam optimizer [41] was used in the training process. Each network was identified with a unique Model #.

2.4.3. Evaluation Metrics. The commonly used evaluation metrics were implemented for our multiclass performance as in Equations (3)–(5).

Precision:

$$\text{Precision} = TP/(TP + FP) \tag{3}$$

Recall:

$$\text{Recall} = TP/(FN + TP) \tag{4}$$

F score:

$$\text{F score} = (2 \times Precision \times Recall)/(Precision + Recall) \tag{5}$$

In Equations (3)–(5), True Positive (TP) describes a sample from X_m from a certain class y_m that is correctly classified as y_m; False Positive (FP) represents a sample of X_m which does not belong to class y_m but incorrectly classified as y_m; False Negative (FN) is defined as a sample of X_m belonging to the class y_m that is incorrectly classified as "not y_m" classes. F score in Equation (5) indicates the overall performance of the precision and recall, which is their harmonic mean in the interval of [0, 1].

3. RESULTS AND DISCUSSION

3.1. EVALUATION OF THE CNN ARCHITECTURE

Because of the complexity and parametric variation existing in the CNN models, it was not feasible to perform all possible models with their parameters, e.g., kernel size, the number of convolutional layers. Therefore, six representative CNN models with an increasing number of convolutional layers were compared to find the optimal network. The experimental results of the six CNN frameworks are tabulated in Table 3. It was shown that by increasing the depth and the number of kernels of the network, the validation accuracy changed from 74.6% to 83.8% (from Model 1 to Model 6). The

accuracy and loss plots for Model 6 in Figure 4 suggested the overfitting, in which the model fit better on the training dataset than on the validation dataset. Considering the validation accuracy, the following data augmentation operations were conducted with the network used in Models 3–6.

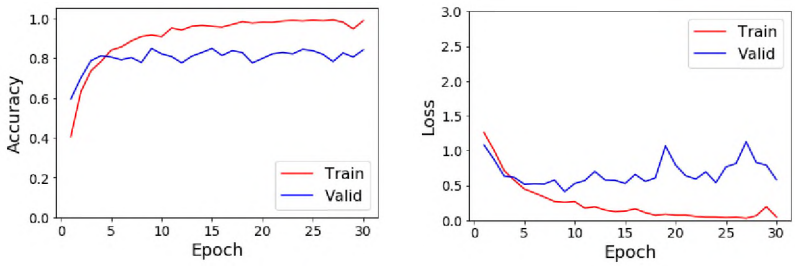

(a) (b)

Figure 4. (a) The accuracy and (b) the loss values of the training and validation dataset for Model 6.

Table 3. Experimental results with six architectures. The convolutional layers' parameters are denoted as "C kernel size/number of kernels". The fully connected layers are denoted as "FC number of hidden units". Epoch = 30, learning rate = 1×10^{-4}.

Model #	Architecture	Time (h:m:s)	Val. Acc. (%)
1	C 3 × 3/8, C 3 × 3/16, FC 64	0:4:30	74.6
2	C 5 × 5/8, C 5 × 5/16, FC 64	0:4:46	76.7
3	C 3 × 3/16, C 3 × 3/32, C 3 × 3/64, FC 256, FC 64	0:4:37	79.5
4	C 5 × 5/16, C 5 × 5/32, C 5 × 5/64, FC 256, FC 64	0:4:45	80.1
5	C 3 × 3/32, C 3 × 3/64, C 3 × 3/128, FC 512, FC 64	0:5:43	82.5
6	C 5 × 5/32, C 5 × 5/64, C 5 × 5/128, FC 512, FC 64	0:6:31	83.8

3.2. IMPACT OF DATA AUGMENTATION

Data augmentation operations were carried out on original images, and the classification performance is provided in Table 4. It was found that the validation accuracy has improved up to 5.6% compared to Table 3. It took an average of 5 min 13 s

longer to train the models compared to doing so without data augmentation. Therefore, with the availability of large training datasets, the CNN models could achieve high accuracies. The following regularization was performed on the architectures of Models 5 and 6 associated with data augmentation.

3.3. REGULARIZATION

Regularization could be used to mitigate the problem of overfitting during the training process. The implementation of L2 regularization and dropout were explored in our study. L2 regularization applies a penalty on large framework parameters and forces them to be relatively small. Dropout is a method that randomly drops units in the network. Several combinations of L2 regularization and dropout in convolutional and fully connected layers were tested.

Table 4. Experimental results of Models 3–6 using data augmentation operations. The convolutional layers' parameters are denoted as "C kernel size/number of kernels". The fully connected layers are denoted as "FC number of hidden units". Epoch = 30 and learning rate = 1×10^{-4}.

Model #	Architecture	Time (h:m:s)	Val. Acc. (%)
3	C 3 × 3/16, C 3 × 3/32, C 3 × 3/64, FC 256, FC 64	0:10:39	81.2
4	C 5 × 5/16, C 5 × 5/32, C 5 × 5/64, FC 256, FC 64	0:10:11	85.7
5	C 3 × 3/32, C 3 × 3/64, C 3 × 3/128, FC 512, FC 64	0:10:37	86.7
6	C 5 × 5/32, C 5 × 5/64, C 5 × 5/128, FC 512, FC 64	0:11:05	87.3

The training time and validation accuracy of eight models were presented in Table 5. The use of L2 in the convolutional layer with a ratio of 1×10^{-5} and a dropout rate of 0.25 on all layers was demonstrated to be the most conducive for both architectures. Regarding the convolutional kernel size, the size of 5 has a 4.3% higher validation

accuracy than the size of 3. Therefore, Model 11 was chosen, and the corresponding accuracy and loss plots are shown in Figure 5. It was observed that the overfitting issue was alleviated compared to Model 6 in Figure 4, but more fine tuning of regularization parameters and longer training time were needed to improve the network performance.

Table 5. Experimental results of different L2 regularization and dropout parameters. The convolutional layers' parameters are denoted as "C kernel size/number of kernels". The fully connected layers are denoted as "FC number of hidden units". Epoch = 30 and learning rate = 1×10^{-4}.

Model #	Architecture	L2	Dropout	Time (h:m:s)	Val. Acc. (%)
7	C 3 × 3/32, C 3 × 3/64, C 3 × 3/128, FC 512, FC 64	Y(1×10^{-5}) | N [1]	Y(0.25)|Y(0.25)	0:10:43	84.4
8		Y(1×10^{-5}) | Y(1×10^{-5})	Y(0.25)|Y(0.25)	0:11:05	82.5
9		Y(1×10^{-5}) | Y(1×10^{-5})	N|N	0:10:47	77.6
10		N|N	Y(0.25)|Y(0.25)	0:10:56	81.2
11	C 5 × 5/32, C 5 × 5/64, C 5 × 5/128, FC 512, FC 64	Y(1×10^{-5}) | N	Y(0.25)|Y(0.25)	0:10:24	88.7
12		Y(1×10^{-5})|Y(1×10^{-5})	Y(0.25)|Y(0.25)	0:10:29	87.5
13		Y(1×10^{-5})|Y(1×10^{-5})	N|N	0:10:17	73.2
14		N|N	Y(0.25)|Y(0.25)	0:10:10	87.8

[1] The left side of "|" indicates the use of regularization in the convolutional layer, and the right side of "|" means the use of regularization in the fully connected layer. "N" means no regularization. "Y" means the use of regularization, the number in "()" means the regularization parameter.

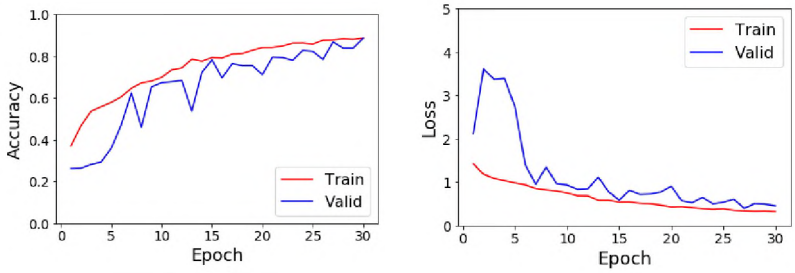

(a) (b)

Figure 5. (a) The accuracy and (b) the loss values of the training and validation dataset for Model 11 using data augmentation, L2 regularization, and dropout.

Model 11 was trained for the fine tuning dropout parameters with epochs of 300, and the results are listed in Table 6. Model 16 achieved a validation accuracy of 94.3% and outperformed other models. The accuracy and loss plots of the four tested models are shown in Figure 6. The learning rate was increasing until around 100–150 epochs in Figure 6a. The training and validation accuracy climbed until about 50–100 epochs and then plateaued as seen in Figure 6c,e,g, but overfitting was displayed as worse in Models 17 and 18. Thus, Model 16 was chosen as our final model that converged fast and had high validation accuracy of 94.3% with a training time of about 1 h and 46 min. The schematic architecture of Model 16 is shown in Figure 3.

3.4. PERFORMANCE EVALUATION

The performance of our final model was evaluated on the test dataset. The results of the precision recall and F score of each class are reported in Table 7. Note that the overall F score could reach above 0.9, indicating good classification performance. It took about 8.01 milliseconds to handle one image in our test process, which could be adopted for real-time inspection applications.

Table 6. Results of fine tuning dropout parameters. The convolutional layers' parameters are denoted as "C kernel size/number of kernels". The fully connected layers are denoted as "FC number of hidden units". Epoch = 300 and learning rate = 1×10^{-4}.

Model #	Architecture	Dropout	Time (h:m:s)	Val. Acc. (%)
15	C 5 × 5/32, C 5 × 5/64, C 5 × 5/128, FC 512, FC 64	Y(0.5)|Y(0.5)	1:43:43	87.5
16		Y(0.25)|Y(0.25)	1:46:32	94.3
17		Y(0.1)|Y(0.1)	1:41:56	92.7
18		Y(0.1)|Y(0.25)	1:43:04	90.7

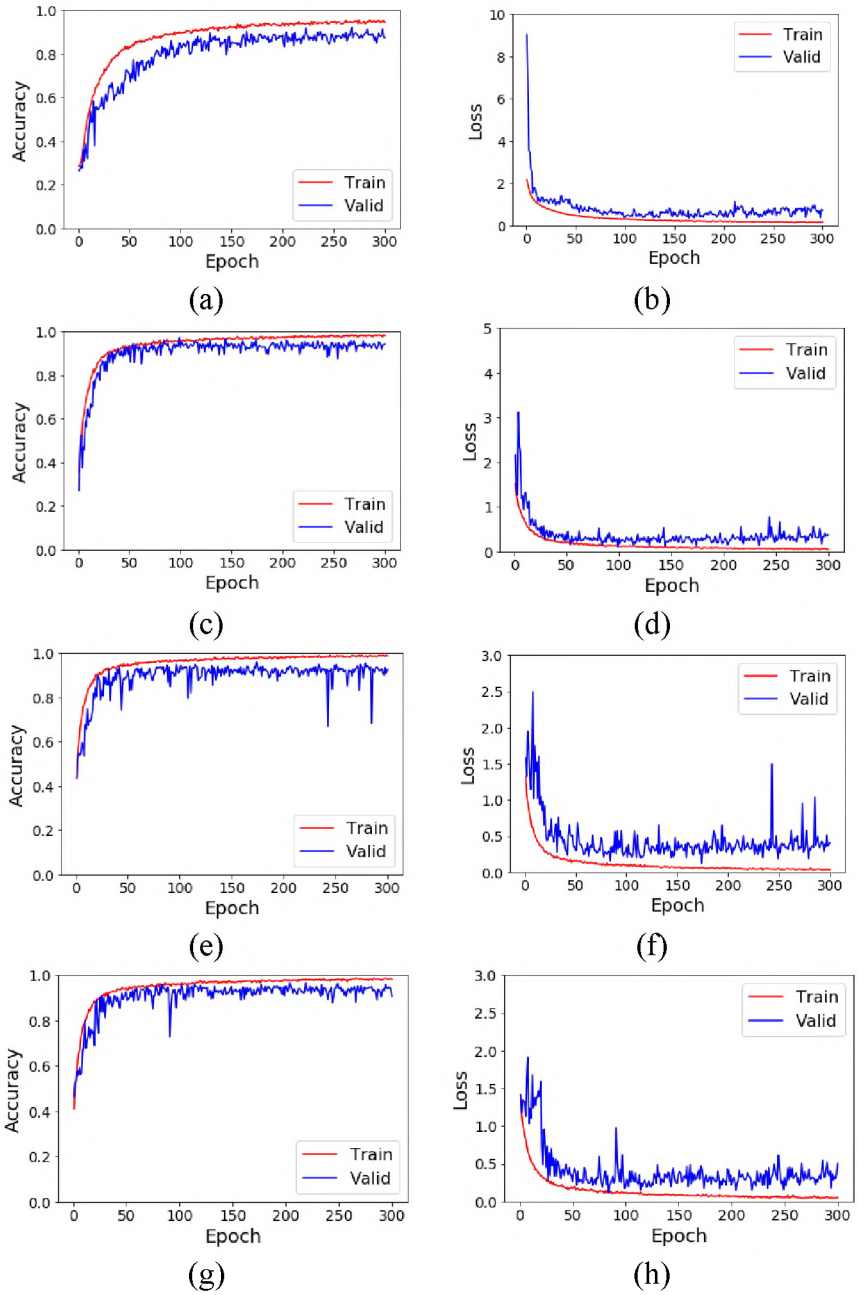

Figure 6. Plots of accuracy and loss for (a,b) Model 15, (c,d) Model 16, (e,f) Model 17 and (g,h) Model 18. (a,c,e) and (g) are accuracy plots and (b,d,f) and (h) are loss plots.

The classification accuracy of three different alloys in the test dataset is listed in Table 8. It is shown that the average accuracy is 91.9% (AlCoCrFeNi alloy), 91.5%

(Ti6Al4V) and 92.7% (AISI 304 stainless steel) respectively, and the difference is ~1%. This indicates that the model can classify the defects robustly for different alloys.

Table 7. Precision, recall, and F score of the final model on the test dataset.

Class	Precision	Recall	F Score
Crack	0.94	0.95	0.945
Gas porosity	0.91	0.87	0.891
Good quality	0.96	0.94	0.949
Lack of fusion	0.88	0.92	0.901

Table 8. Classification accuracy of different alloys in the test dataset.

Alloys	Good	Lack of Fusion	Crack	Gas Porosity
AlCoCrFeNi alloy	93.1%	91.2%	94.9%	88.5%
Ti6Al4V	95.1%	88.7%	93.7%	88.3%
AISI 304 stainless steel	96.4%	89.3%	94.8%	90.4%

Table 9 reports the comparison of the test accuracy of our approach and other methods whose codes are publicly available. The results were experimental on our metal AM parts quality dataset. The accuracy obtained by histogram of oriented gradients (HOG) + SVM [42] was 79.6%, while the accuracy of 89.3% was achieved using Liu's CNN model [36]. Our approach had an accuracy of 92.1%. This could be attributed to our model being efficient in learning the internal features of the AM metal defects, which would be a benefit for our classification task.

Table 9. The performance of classification accuracy with different methods.

Method	Accuracy
Li et al. [42]	79.6%
Liu et al. [36]	89.3%
This work	92.2%

3.5. FEATURE VISUALIZATION

To have a better understanding of what the CNN model has learned, the learned filters and the extracted feature maps are visualized in Figure 7. The 32 filters from the first convolutional layers are shown in Figure 7a. Four samples representing crack, lack of fusion, gas porosity, and good quality are present in Figure 7b–e. It seems difficult to interpret those 32 5 × 5 filters in Figure 7a, but some low-level features are extracted by reviewing the features maps in Figure 7b–e. For example, these filters were able to identify the edges of the crack, as in Figure 7b. The irregular shape of the lack of fusion was emphasized by the filters, which was different from the round shape in gas porosity. The second and the third convolutional layers are not discussed here, as they contain the high-dimensional information and make it less visually interpretable.

Attention maps can be obtained for a given input image with back-propagation on a CNN model. The value of each pixel on the attention map is able to reveal to what extent the same pixel on the input image makes contributions to the final output of the network [18,19]. Therefore, through the attention maps, it can intuitively analyze which part of the AM build metal images attracts the attention of the network. Figure 8 includes the AM build metallic parts profiles shown in a–d and the corresponding attention maps e–h. The defects were highlighted in the red circles and rectangles in Figure 8a–d. The bright places indicate where the CNN model focuses, as seen in Figure 8e–h, while the dark regions suggest where the network is less interested. Those maps demonstrate that the network pays attention to the defects and verify the effectiveness of our model.

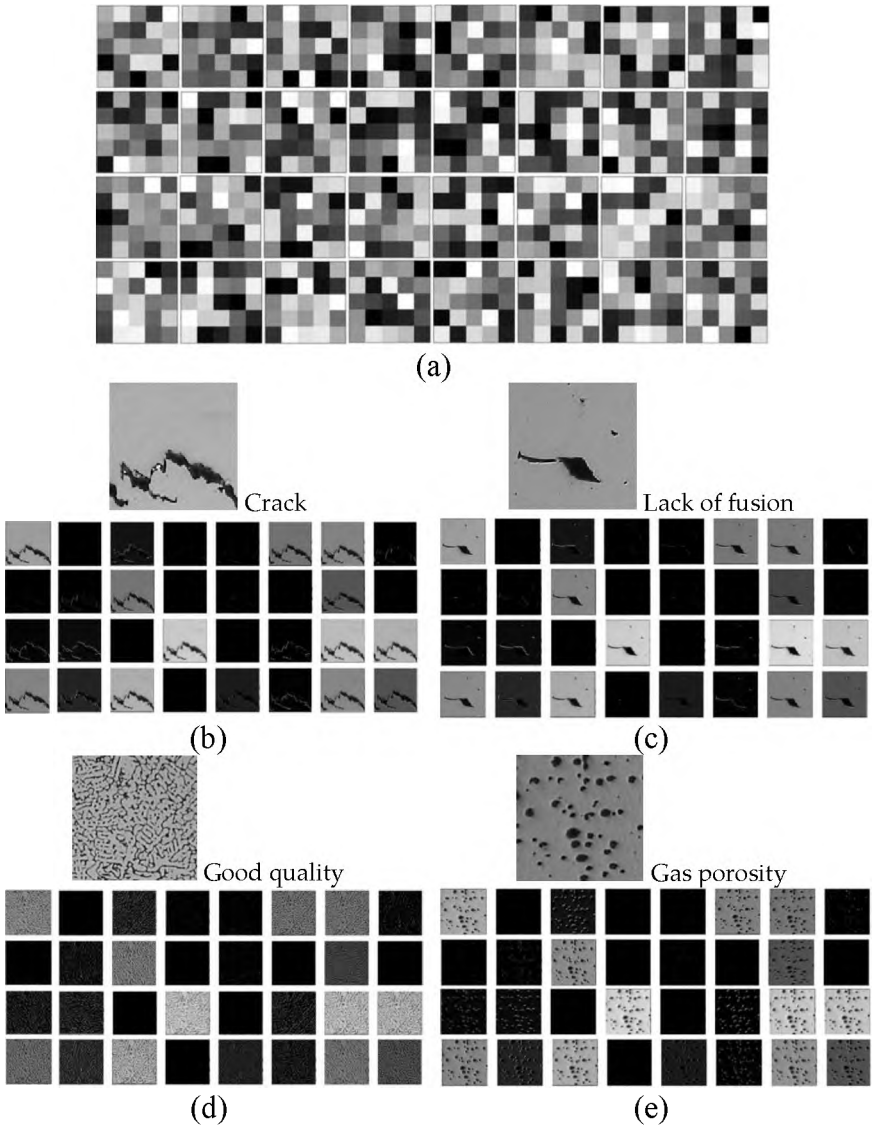

Figure 7. Visualization of the (a) 32 learned filters of the first convolutional layers, (b) 32 feature maps for a crack sample, (c) 32 feature maps for a lack of fusion sample, (d) 32 feature maps for a good sample and (e) 32 feature maps for a gas porosity sample.

3.6. FAILURE CASE STUDY

The failure cases that were not correctly classified in the test dataset will be discussed in this subsection. Some incorrectly classified images are shown in Figure 9. The image shown in Figure 9a was misclassified as "good" as the dirt on the sample surface led to misclassification. The sample images shown in Figure 9b–d could be

attributed to the high similarity between the gas porosity and lack of fusion, which makes it difficult to distinguish them.

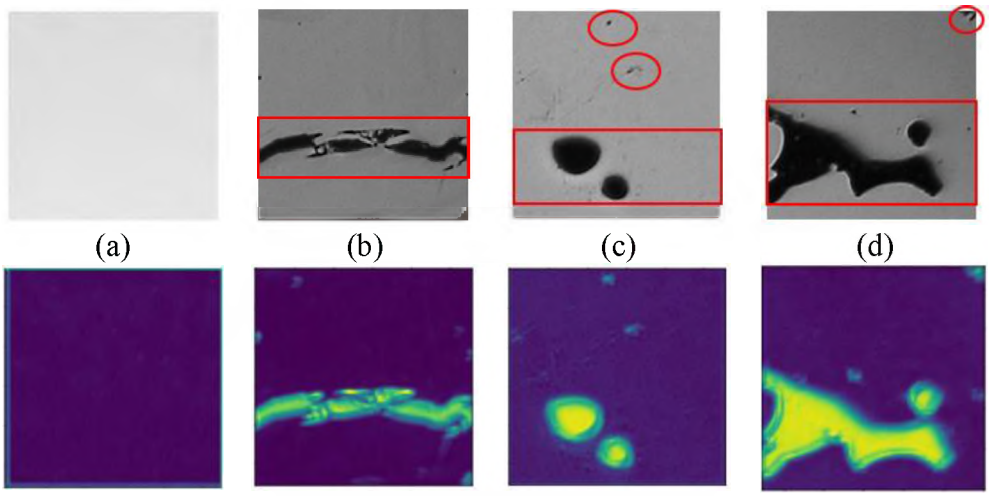

Figure 8. (a–d) Additive manufacturing build metal parts images, (e–h) attention maps corresponding to (a–d).

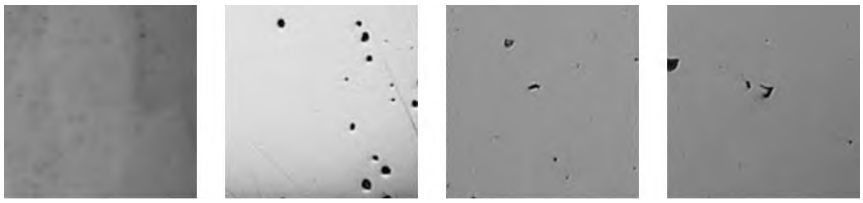

Figure 9. Examples of wrongly classified images in the test dataset of metal additive manufacturing defects. Results highlighted in black and red indicate correct and incorrect classification results, respectively. (a) Gas—Good, (b) Gas—LoF, (c) Gas—LoF, (d) LoF—Gas.

To address the failure cases for performance improvement, some future work will be explored: (1) A variety of AM manufactured materials can be considered to be

included to enlarge the dataset, e.g., ceramics, glass, polymers, and composites. (2) The architecture of the CNN models can be explored to enhance its performance.

4. CONCLUSION

In this paper, we presented the application of a convolutional neural network (CNN) for robust quality inspection of metal additive manufacturing (AM) parts. The Missouri S&T dataset, including optical microscope images of real-world metal AM parts were used to train and test the CNN model. This work contributed to the development of a CNN model with excellent performance in recognition of good quality, crack, gas porosities, and lack of fusion categories. To generate the appropriate model, extensive experiments were investigated on hyper-parameters including kernel size and the number of layers, data augmentation operations, and regularization. Our final model achieved an accuracy of 92.1% with 8.01 milliseconds recognition time of one image. The results indicate the promising application of the CNN method in quality inspection in the AM industry. It would be interesting to explore more CNN architectures and include a variety of materials in the future.

ACKNOWLEDGMENTS

The authors are grateful for the financial support from NSF (National Science Foundation) grants CMMI-1625736 and EEC-1937128, and Intelligent System Center (ISC) at Missouri University of Science and Technology. The materials preparation and

characterization were supported by the Materials Research Center (MRC) at Missouri University of Science and Technology. W.C. would like to thank Wenbin Li and Wenjin Tao from Missouri University of Science and Technology for their discussion and suggestions.

REFERENCES

[1] A. Caggiano, J. Zhang, V. Alfieri, F. Caiazzo, R. Gao, and R. Teti, "Machine learning-based image processing for on-line defect recognition in additive manufacturing," *CIRP Ann.*, vol. 68, no. 1, pp. 451–454, Jan. 2019.

[2] B. E. Carroll et al., "Functionally graded material of 304L stainless steel and inconel 625 fabricated by directed energy deposition: Characterization and thermodynamic modeling," Acta Mater., vol. 108, pp. 46–54, Apr. 2016.

[3] A. Reichardt et al., "Development and characterization of Ti-6Al-4V to 304L stainless steel gradient components fabricated with laser deposition additive manufacturing," Mater. Des., vol. 104, pp. 404–413, Aug. 2016.

[4] C. Huang, Y. Zhang, R. Vilar, and J. Shen, "Dry sliding wear behavior of laser clad TiVCrAlSi high entropy alloy coatings on Ti-6Al-4V substrate," Mater. Des., vol. 41, pp. 338–343, Oct. 2012.

[5] W. Cui, S. Karnati, X. Zhang, E. Burns, and F. Liou, "Fabrication of AlCoCrFeNi high-entropy alloy coating on an AISI 304 substrate via a CoFe2Ni intermediate layer," Entropy, vol. 21, no. 1, p. 2, Jan. 2019.

[6] P. Åkerfeldt, M. L. Antti, and R. Pederson, "Influence of microstructure on mechanical properties of laser metal wire-deposited Ti-6Al-4V," Mater. Sci. Eng. A, vol. 674, pp. 428–437, Sep. 2016.

[7] P. Åkerfeldt, R. Pederson, and M. L. Antti, "A fractographic study exploring the relationship between the low cycle fatigue and metallurgical properties of laser metal wire deposited Ti-6Al-4V," Int. J. Fatigue, vol. 87, pp. 245–256, Jun. 2016.

[8] G. Sun, R. Zhou, J. Lu, and J. Mazumder, "Evaluation of defect density, microstructure, residual stress, elastic modulus, hardness and strength of laser-deposited AISI 4340 steel," Acta Mater., vol. 84, pp. 172–189, Feb. 2015.

[9] H. Taheri, M. Rashid Bin, M. Shoaib, L. Koester, T. Bigelow, and P. C. Collins, "Powder-based additive manufacturing – a review of types of defects, generation mechanisms, detection, property evaluation and metrology," Int. J. Addit. Subtractive Mater. Manuf., vol. 1, no. 2, pp. 172–209, 2017.

[10] W. Li et al., "Fabricating Functionally Graded Materials by Ceramic On-Demand Extrusion with Dynamic Mixing," in Proceedings of the 29th Annual International Solid Freeform Fabrication Symposium, 2018, pp. 1087–1099.

[11] M. N. Ahsan, A. J. Pinkerton, R. J. Moat, and J. Shackleton, "A comparative study of laser direct metal deposition characteristics using gas and plasma-atomized Ti-6Al-4V powders," Mater. Sci. Eng. A, vol. 528, no. 25–26, pp. 7648–7657, Sep. 2011.

[12] W. Li, A. Ghazanfari, D. McMillen, M. C. Leu, G. E. Hilmas, and J. Watts, "Characterization of zirconia specimens fabricated by ceramic on-demand extrusion," Ceram. Int., vol. 44, no. 11, pp. 12245–12252, Aug. 2018.

[13] S. M. Azimi, D. Britz, M. Engstler, M. Fritz, and F. Mücklich, "Advanced steel microstructural classification by deep learning methods," Sci. Rep., vol. 8, no. 1, p. 2128, Dec. 2018.

[14] S. Guan, "Strip Steel Defect Detection Based on Saliency Map Construction Using Gaussian Pyramid Decomposition," ISIJ Int., vol. 55, no. 9, pp. 1950–1955, 2015.

[15] S. Barua, F. Liou, J. Newkirk, and T. Sparks, "Vision-based defect detection in laser metal deposition process," Rapid Prototyp. J., vol. 20, no. 1, pp. 77–85, 2014.

[16] L. Yi, G. Li, and M. Jiang, "An End-to-End Steel Strip Surface Defects Recognition System Based on Convolutional Neural Networks," Steel Res. Int., vol. 88, no. 2, pp. 176–187, Feb. 2017.

[17] W. Tao, M. C. Leu, and Z. Yin, "American Sign Language alphabet recognition using Convolutional Neural Networks with multiview augmentation and inference fusion," Eng. Appl. Artif. Intell., vol. 76, pp. 202–213, Nov. 2018.

[18] K. Li, Z. Wu, K. C. Peng, J. Ernst, and Y. Fu, "Tell Me Where to Look: Guided Attention Inference Network," in Proceedings of the IEEE Computer Society Conference on Computer Vision and Pattern Recognition, 2018, pp. 9215–9223.

[19] B. Zhou, A. Khosla, A. Lapedriza, A. Oliva, and A. Torralba, "Learning Deep Features for Discriminative Localization," in Proceedings of the IEEE Computer Society Conference on Computer Vision and Pattern Recognition, 2016, pp. 2921–2929.

[20] T. Wang, Y. Chen, M. Qiao, and H. Snoussi, "A fast and robust convolutional neural network-based defect detection model in product quality control," Int. J. Adv. Manuf. Technol., vol. 94, no. 9–12, pp. 3465–3471, Feb. 2018.

[21] Y. Lecun, Y. Bengio, and G. Hinton, "Deep learning," Nature, vol. 521, no. 7553, pp. 436–444, May 2015.

[22] A. Krizhevsky, I. Sutskever, and G. E. Hinton, "ImageNet classification with deep convolutional neural networks," Adv. Neural Inf. Process. Syst., pp. 1097–1105, 2012.

[23] X. Qi, G. Chen, Y. Li, X. Cheng, and C. Li, "Applying Neural-Network-Based Machine Learning to Additive Manufacturing: Current Applications, Challenges, and Future Perspectives," Engineering, vol. 5, no. 4, pp. 721–729, Aug. 2019.

[24] H. Gaja and F. Liou, "Defect classification of laser metal deposition using logistic regression and artificial neural networks for pattern recognition," Int. J. Adv. Manuf. Technol., vol. 94, no. 1–4, pp. 315–326, Jan. 2018.

[25] M. Khanzadeh, S. Chowdhury, M. Marufuzzaman, M. A. Tschopp, and L. Bian, "Porosity prediction: Supervised-learning of thermal history for direct laser deposition," J. Manuf. Syst., vol. 47, pp. 69–82, Apr. 2018.

[26] C. Gobert, E. W. Reutzel, J. Petrich, A. R. Nassar, and S. Phoha, "Application of supervised machine learning for defect detection during metallic powder bed fusion additive manufacturing using high resolution imaging.," Addit. Manuf., vol. 21, pp. 517–528, May 2018.

[27] B. L. DeCost, H. Jain, A. D. Rollett, and E. A. Holm, "Computer Vision and Machine Learning for Autonomous Characterization of AM Powder Feedstocks," JOM, vol. 69, no. 3, pp. 456–465, Mar. 2017.

[28] C. S. Venegas-Barrera and J. Manjarrez, "Visual Categorization with Bags of Keypoints," in In Workshop on statistical learning in computer vision, ECCV, 2004, pp. 1–22.

[29] J. Zhang, M. M. Lek, S. Lazebnik, and C. Schmid, "Local Features and Kernels for Classification of Texture and Object Categories: A Comprehensive Study," Int. J. Comput. Vis., vol. 73, no. 2, pp. 213–238, 2007.

[30] B. L. DeCost, T. Francis, and E. A. Holm, "Exploring the microstructure manifold: Image texture representations applied to ultrahigh carbon steel microstructures," Acta Mater., vol. 133, pp. 30–40, Jul. 2017.

[31] A. Chowdhury, E. Kautz, B. Yener, and D. Lewis, "Image driven machine learning methods for microstructure recognition," Comput. Mater. Sci., vol. 123, pp. 176–187, Oct. 2016.

[32] R. Kondo, S. Yamakawa, Y. Masuoka, S. Tajima, and R. Asahi, "Microstructure recognition using convolutional neural networks for prediction of ionic conductivity in ceramics," Acta Mater., vol. 141, pp. 29–38, Dec. 2017.

[33] S. Wen, Z. Chen, and C. Li, "Vision-based surface inspection system for bearing rollers using convolutional neural networks," Appl. Sci., vol. 8, no. 12, p. 2565, Dec. 2018.

[34] X. Tao, D. Zhang, W. Ma, X. Liu, and De Xu, "Automatic metallic surface defect detection and recognition with convolutional neural networks," Appl. Sci., vol. 8, no. 9, p. 1575, Sep. 2018.

[35] R. Wei and Y. Bi, "Research on Recognition Technology of Aluminum Profile Surface Defects Based on Deep Learning," Materials (Basel)., vol. 12, no. 10, p. 1681, May 2019.

[36] Zhu, Ge, and Liu, "Deep Learning-Based Classification of Weld Surface Defects," Appl. Sci., vol. 9, no. 16, p. 3312, Aug. 2019.

[37] Y. Liu, K. Xu, and J. Xu, "Periodic Surface Defect Detection in Steel Plates Based on Deep Learning," Appl. Sci., vol. 9, no. 15, p. 3127, Aug. 2019.

[38] A. Azarniya et al., "Additive manufacturing of Ti–6Al–4V parts through laser metal deposition (LMD): Process, microstructure, and mechanical properties," Journal of Alloys and Compounds, vol. 804. Elsevier Ltd, pp. 163–191, 05-Oct-2019.

[39] L. Yan et al., "Build Strategy Investigation of Ti-6Al-4V Produced Via a Hybrid Manufacturing Process," JOM, vol. 70, no. 9, pp. 1706–1713, 2018.

[40] S. Ioffe and C. Szegedy, "Batch normalization: Accelerating deep network training by reducing internal covariate shift," in 32nd International Conference on Machine Learning, ICML 2015, 2015, vol. 1, pp. 448–456.

[41] D. P. Kingma and J. L. Ba, "Adam: A method for stochastic optimization," in In Proceedings of the International Conference on Learning Representations (ICLR)), 2015.

[42] S. Ding, Z. Liu, and C. Li, "AdaBoost learning for fabric defect detection based on HOG and SVM," in 2011 International Conference on Multimedia Technology, ICMT 2011, 2011, pp. 2903–2906.

IV. LASER METAL DEPOSITION OF AN $AlCoCrFeNiTi_{0.5}$ HIGH-ENTROPY ALLOY COATING ON A Ti6Al4V SUBSTRATE: MICROSTRUCTURE AND OXIDATION BEHAVIOR

ABSTRACT

Ti6Al4V has been recognized as an attractive material, due to its combination of low density and favorable mechanical properties. However, its insufficient oxidation resistance has limited the high-temperature application. In this work, an $AlCoCrFeNiTi_{0.5}$ high-entropy alloy (HEA) coating was fabricated on a Ti6Al4V substrate using laser metal deposition (LMD). The microstructure and isothermal oxidation behaviors were investigated. The microstructure of as-deposited HEA exhibited a Fe, Cr-rich A2 phase and an Al, Ni, Ti-enriched B2 phase. Its hardness was approximately 2.1 times higher than that of the substrate. The oxidation testing at 700 °C and 800 °C suggested that the HEA coating has better oxidation resistance than the Ti6Al4V substrate. The oxide scales of the Ti6Al4V substrate were mainly composed of TiO_2, while continuous Al_2O_3 and Cr_2O_3 were formed in the HEA coatings and could be attributed to oxidation resistance improvement. This work provides an approach to mitigate the oxidation resistance of Ti6Al4V and explore the applicability of the HEA in a high-temperature environment.

1. INTRODUCTION

Ti6Al4V has been an important and versatile titanium alloy currently used in petrochemical, automotive, power generation, and biomedical industries. Indeed, this alloy possesses a desirable combination of properties, such as high melting point,

superior corrosion resistance, good biocompatibility, and weldability [1-3]. However, Ti6Al4V alloy is very active at elevated temperature, which results in being easily oxidized, as well as its insufficient oxidation resistance [4,5]. At present, the permitted maximal service temperature of Ti6Al4V alloy still does not exceed 600 °C [1,4]. The improvement of its high-temperature oxidation property can be solved by the surface modification process [3-6].

As a promising surface modification technology, laser metal deposition (LMD) has introduced a number of capabilities unparalleled by conventional process [3,6-11]. LMD achieves layer-by-layer fabrication of near net-shaped deposition onto the substrate by introducing a powder stream into a laser beam. In addition to the geometry freedom, precise tailoring of compositions and microstructure can be achieved to produce highly specialized coatings. On the basis of these advantages, many efforts have been made to improve the oxidation resistance of Ti6Al4V alloy. In particular, Liu et al. prepared a TiN/Ti_3Al composite coating on the Ti6Al4V substrate [12]. The isothermal oxidation results indicated that the relative oxidation resistance of the coating was approximately six times higher than that of the substrate at 600 °C, due to the formation of TiN, Al_2O_3, and TiO_2. A titanium–aluminum alloy (Ti48Al2Cr2Nb) was adopted as a coating material and demonstrated good anti-oxidation property in comparison with the Ti6Al4V at 800 °C [13]. Successive layers of oxides (up to 12 μm thick) were formed on the Ti48Al2Cr2Nb after 150 h of oxidation, while the oxide layers detached from the Ti6Al4V after 5 h. A gradient Ti-Ni alloy was fabricated by laser cladding, and a dense Al_2O_3 layer was formed, inhibiting the further diffusion of oxygen atoms under 800 °C [14]. Wang et al. manufactured a Ti_5Si_3/γ/TiSi composite coating, in which the presence

of continuous Al_2O_3 and SiO_2 scales contributed to the high-temperature oxidation resistance [15]. The authors also discovered that Ti_5Si_3 and TiSi possessed brittleness at room temperature, and the shedding was observed on the worn face of the coatings. Although the titanium silicide-based materials mentioned above can have an excellent high-temperature oxidation resistance, they also bring some issues, such as the brittleness at room temperature and high cracking susceptibility [2,6,15].

An important concept of "High-entropy alloys (HEAs)" has broken the traditional idea of alloy design based on one or two principal components [16-18]. This new class of alloys typically contain 5 to 13 principal elements, and the concentration of each element is between 5 and 35 atomic percent. The high-entropy effect of HEAs is beneficial to the formation of the solid solution with crystal structures such as face-centered cubic (FCC), body-centered cubic (BCC), or hexagonal close-packed (HCP), instead of too many complex intermetallic compounds. Among a variety kind of HEAs, Al-Co-Cr-Fe-Ni has been one of the most developed and refined systems. The equimolar AlCoCrFeNi alloy exhibited dendritic and interdendritic microstructures, which were composed of CrFe-rich precipitates embedded in an AlNi-rich matrix [19,20]. After the ageing treatments at 800 °C, 1000 °C, and 1200 °C, the precipitation of an FCC phase resulted in reduced compressive yield strength accompanied by enhanced ductility [21]. Concerning the oxidation resistance, the sluggish diffusion kinetics has been found, and it can restrain the formation of non-protective transient oxides [22,23]. Mohanty et al. investigated two types of HEAs ($Al_{0.3}$CoCrFeNi and $Al_{0.7}$CoCrFeNi) and reported that the thickness of the oxide layer increased with the content of Al [24]. The oxidation behaviors of a series of arc-melted $Al_X(NiCoCrFe)_{100-X}$ (x = 8, 10, 12, 15, 20 and 30 atomic%) and

AlCoCrFeNi(Fe or Si) HEAs were studied by Butler et al. [25,26]. The oxide scales contained a combination of Al_2O_3, AlN beneath, and external Cr_2O_3 scale. Each HEA exhibited initial transient oxidation followed by parabolic oxide growth. The oxidation study of $AlCoCrCu_xFeNi$ (x = 0, 0.5, 1 in molar ratio) revealed the parabolic constants were at the same level as those Al-Ni intermetallic alloys [27]. The oxide scales consisted of α-Al_2O_3 and were visible on the oxidation surface of these HEAs. The addition of Ti could lead to solid solution strengthening and precipitation strengthening in $Al_{1.5}CrFeMnTi$ and $AlCoCrFeNiTi_x$ HEAs [28,29]. The study of $Al_xCoCrFeNiTi_{1-x}$ (x = 1, 0.8, 0.5 in molar ratio) indicated that Ti promoted the formation of FCC phase, and Al resulted in BCC phase [30]. Nevertheless, these HEAs have been mainly prepared by arc melting [25-27,29,30], thermal spray technique [31], and the electrospark process [32] . Therefore, it is desirable to laser fabricate an $AlCoCrFeNiTi_{0.5}$ HEA coating and evaluate its oxidation performance.

This work aimed to investigate the microstructure and oxidation behavior of an $AlCoCrFeNiTi_{0.5}$ HEA coating synthesized on the Ti6Al4V substrate by laser metal deposition. Microstructural characterization was performed on the as-deposited HEA coating. Then, the isothermal oxidation test was conducted to evaluate its oxidation behaviors at elevated temperatures. The weight change, phase constitutions, and cross-sectional morphology after oxidation were analyzed and discussed.

2. MATERIALS AND METHODS

2.1. SAMPLE PREPARATION

$AlCoCrFeNiTi_{0.5}$ HEA samples with the nominal composition (as shown in Table 1) were prepared by LMD. Spherical gas-atomized elemental powder blends were used. The powders of Al, Co, Cr, Fe, Ni, and Ti were supplied by Micron Metals (Ramapo, NJ, USA) with 99.9% purity and 44–145 μm particle size distribution. The powder mixture (total: 276.5 g) was prepared by carefully weighing the powders using a weighing balance with an accuracy of ±0.1 mg. The mixed powders were homogenized in a Turbula mixer (Glen Mills Inc., Clifton, NJ, USA) for 1 h. The experimental setup consisted of an IPG 1 kW continuous wave YAG fiber laser (IPG Photonics, Oxford, MA, USA), a numerical control working table, and a vibration powder feeder (Powder Motion Labs, Rolla, MO, USA), as shown in Figure 1. The Grade 5 Ti6Al4V bar stock was used as the substrates (dimensions 75 mm × 12 mm × 6 mm) and cleaned with acetone to remove the dirt and oil before the experiment. The deposition process was performed in a sealed, controlled environment purged with a continuous flow of argon gas. A pre-heating was undertaken to minimize the thermal stress between the deposit and the Ti6Al4V substrate. The powders were delivered to the laser beam by an argon jet with a flow rate of 3 g/min. The deposits with a thin-wall structure were fabricated at the transverse laser speed of 200 mm/s, 2 mm laser beam size, 0.5 mm layer thickness, and the powers of 700 W for the first two layers, 600 W for the next two layers and 500 W for further layers.

Table 1. Nominal composition (atom%) of an $AlCoCrFeNiTi_{0.5}$ high-entropy alloy (HEA).

	Al	Co	Cr	Fe	Ni	Ti
Atom%	18.2	18.2	18.2	18.2	18.2	9.0

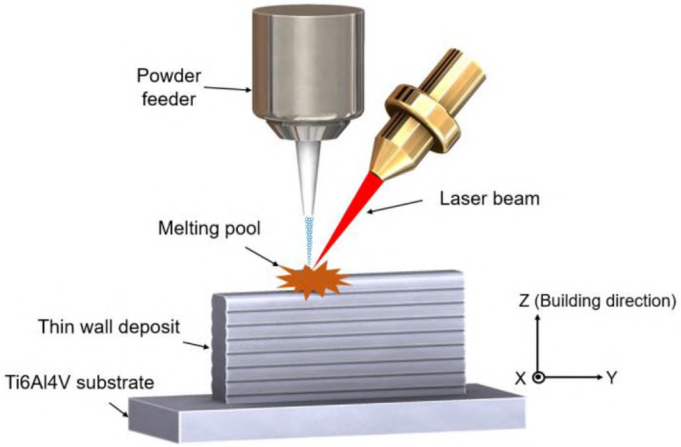

Figure 1. Schematic of the laser metal deposition (LMD) experiment setup.

2.2. CHARACTERIZATION

After the deposition, the specimens were sectioned by electrical discharge machining (EDM) (Hansvedt Industries Inc., Rantoul, IL, USA) and prepared by standard metallographic procedures. They were polished with 320–1200 grit SiC grinding paper, followed by 9 µm, 3 µm, 1 µm diamond solutions with a final step of 0.05 µm colloidal silica suspension. The HEA sample was etched with aqua regia (30 mL HCl and 10 mL HNO3) (Thermal Fisher Scientific, Waltham, WA, USA), and Ti6Al4V was etched with Kroll's reagent (2 mL HF, 8 mL HNO3 and 90 mL H2O) (Thermal Fisher Scientific, Waltham, WA, USA).

The microstructure was characterized by a Helios Nanolab 600 (Thermal Fisher Scientific, Waltham, WA, USA) scanning electron microscope (SEM). The energy

dispersive spectroscopy (EDS) data were collected and analyzed in the factory standardization manner (Oxford AZtec version 4.2). The electron backscatter diffraction (EBSD) scan was acquired using an Oxford HKL system with a step size of 2 μm, and data analysis was performed on HKL Channel 5 software (Oxford Instruments, Abingdon, UK). The grain was determined by a misorientation angle of 10°, and grain size was measured using the line intercept method. X-ray diffraction (XRD) profiling was performed to determine the phase constituents in the samples. The phases were identified by Phillips X'Pert diffractometer (Amsterdam, The Netherlands) using Cu-Kα radiation at 45 kV/40 mA with a scanning step of 0.05° and a scanning range from 20° to 90°. The Vickers hardness was measured using Struers Duramin hardness equipment (Struers Inc, Cleveland, OH, USA) at a 9.8 N load and a duration of 10 s. The reported hardness results were the average of ten indentations.

2.3. OXIDATION TESTS

The HEA and Ti6Al4V specimens for oxidation tests with dimensions of 10 mm (length) × 10 mm (width) × 2 mm (height) were prepared using EDM. Sample surfaces were subsequently polished using 320–1200 grit SiC grinding paper and cleaned with acetone. Oxidation tests were carried out in an electric furnace (DT-29-RSA, Deltech, Denver, CO, USA) under atmospheric pressure at 700 °C and 800 °C for 45 h. The samples were heated from room temperature to the target temperatures at a heating rate of 10 °C/min. The weight gain was measured before and after at specified intervals using an analytic balance (AG204, Mettler Toledo, Columbus, OH, USA) with an accuracy of 0.1 mg. The oxidized samples were characterized by XRD and SEM, as described above.

3. RESULTS AND DISCUSSION

3.1. MICROSTRUCTURE OF THE AS-DEPOSITED HEA

Figure 2 illustrates the XRD patterns of as-deposited $AlCoCrFeNiTi_{0.5}$ HEA and the Ti6Al4V substrate. The α-Ti phase was detected in the Ti6Al4V (Figure 2a). Two BCC phases were observed in the HEA (Figure 2b), and they are ordered a BCC structure (B2) phase and a disordered BCC structure (A2) phase. Through careful analysis of the standard PDF database, the two BCC phases were identified as Al-Ni and Fe-Cr phases, which is in accordance with the similar alloys synthesized using arc-melting [23,30] and casting [33].

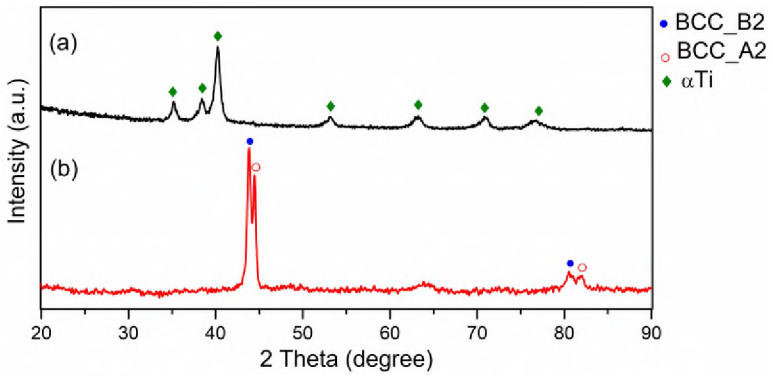

Figure 2. X-ray diffraction (XRD) pattern of the (a) Ti6Al4V substrate and (b) as-deposited $AlCoCrFeNiTi_{0.5}$ HEA.

Figure 3a presents the interface between the HEA coating and the Ti6Al4V substrate, which can be seen as a good metallurgical bond without crack. The EDS line scan was used to characterize the elemental evolution from the Ti6Al4V substrate to the HEA, and the quantitative results are shown in Figure 3b. The EDS measured

compositions of the Ti6Al4V substrate (Ti: ~84–86 atom%, Al: ~10–11 atom%, V: ~3–4 atom%) did not deviate from the nominal compositions of Grade 5 Ti6Al4V. Since the Ti6Al4V was mixed with the HEA layer, the elements of Al (~12–14 atom %), Co (~10–12 atom%), Cr (~11–13 atom%), Fe (~9–11 atom%), Ni (~11–14 atom%) and Ti (~36–39 atom%) were detected. A small amount of V (~1–3 atom%) was detected in the HEA layer, due to the dilution. According to the equilibrium Fe-V, Fe-Ti phase diagrams, the Fe-V or Fe-Ti intermetallic phases might be formed when the content of V was in a range of 30–65 atom% or the content of Fe was above 50 atom% [34-36]. From the elemental analysis above, the contents of V and Fe were low (~10 atom% or below), thus the HEA layer had a low risk of forming those intermetallic phases. Moreover, the XRD patterns obtained did not show Fe-V or Fe-Ti intermetallic phases.

The microstructural details of the laser deposited HEA at different magnifications are shown in Figures 3c,d. The equiaxed grains were delineated by intergranular phases (Figure 3c). The dendritic structure can be observed within the equiaxed grains. The EDS was used to analyze the element distribution, and the results are listed in Table 2 and Figures 4a-g. The dark contrast phase was enriched in Al, Ni, Co, and Ti, and the high level of Fe and Cr concentration was detected in the bright contrast phase. As learned from Table 2, the chemical compositions of Fe and Cr were ~45 atom% in the bright contrast phase while were ~16 atom% in the dark contrast phase. In combination with the phase identification, the dark contrasted phases rich in Al, Ni, and Ti are B2 phase while the bright contrast phases are Fe, Cr enriched A2 phase. A similar microstructure has been observed, and it was attributed to the spinodal decomposition of B2 dendrites into B2 and A2 coexisting phases [20,23,37].

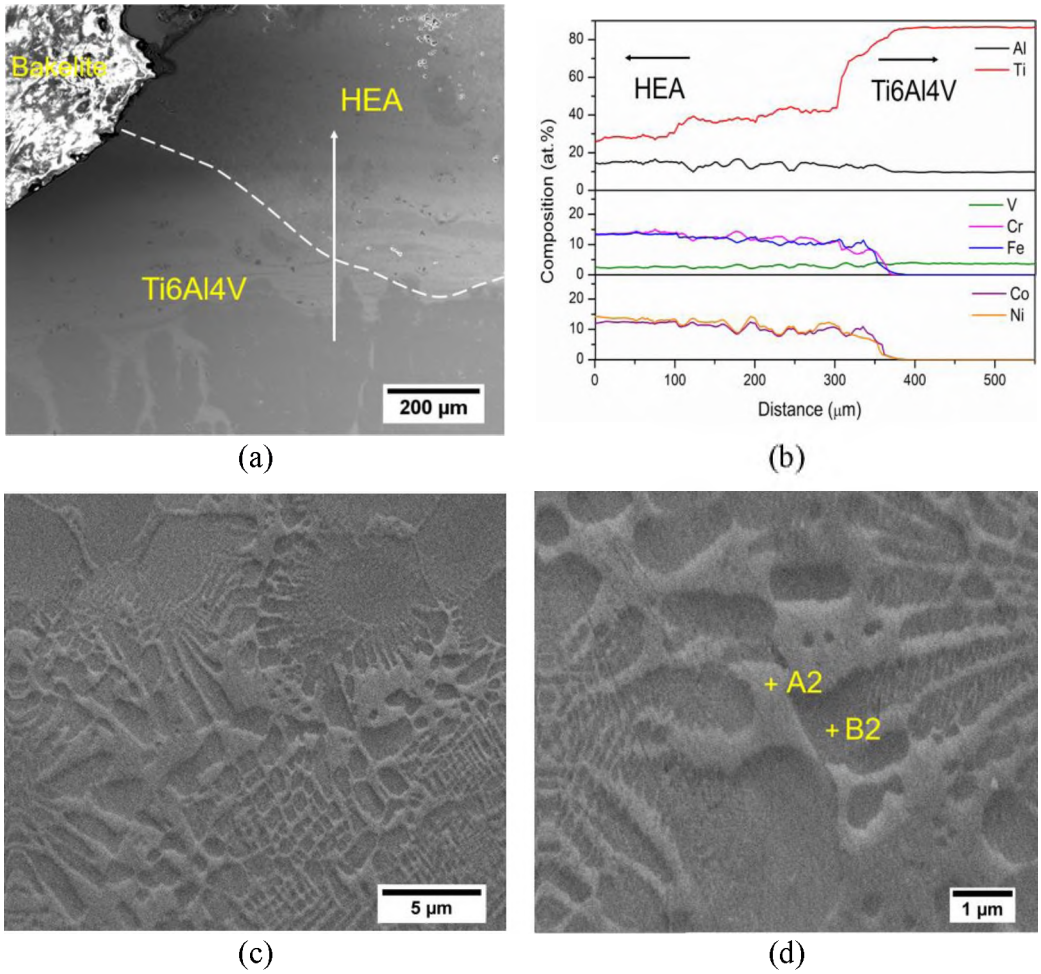

Figure 3. (a) Secondary electron images of the interface between the $AlCoCrFeNiTi_{0.5}$ HEA coating and Ti6Al4V substrate, (b) energy dispersive spectroscopy (EDS) line scan along the white arrow line in (a), (c) and (d) backscattered electron images of the HEA microstructure at different magnifications.

The chemical mixing enthalpies of element pairs in $AlCoCrFeNiTi_{0.5}$ alloy are tabulated in Table 3. The phase formation and element segregation are determined by the mixing enthalpy among the constituent metallic elements. It is shown that Al, Ni, and Co has high negative mixing enthalpy with Ti, and they are liable to generate the B2 phase. For example, the mixing enthalpy between Al-Ti, Al-Ni, and Al-Co are −30 kJ/mol, −22

kJ/mol, and −19 kJ/mol, respectively. Furthermore, Cr and Fe tend to form the A2 phase as they exhibit low mixing enthalpy close to zero.

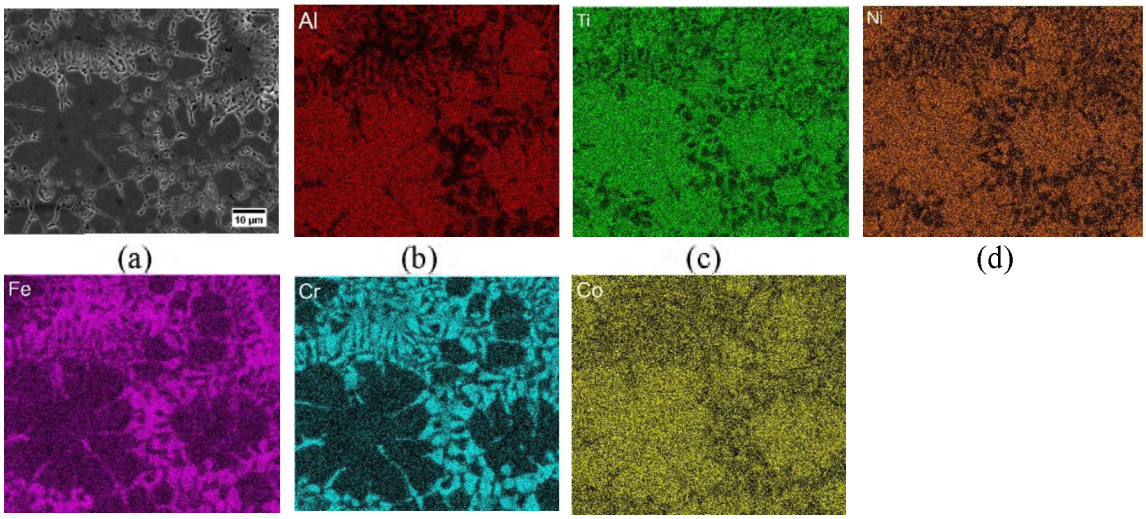

Figure 4. (a) Secondary electron image and the corresponding elemental maps of (b) Al, (c) Ti, (d) Ni, (e) Fe, (f) Cr, and (g) Co of the $AlCoCrFeNiTi_{0.5}$ HEA.

Table 2. Elemental composition (atom %) of each phase in the HEA by SEM-EDS (more than 5 locations).

Phase	Element					
	Al	Co	Cr	Fe	Ni	Ti
B2	24.8 ± 1.6	17 ± 1.0	7.2 ± 0.7	8.4 ± 1.1	21.2 ± 0.6	20 ± 1.7
A2	15.5 ± 2.1	13.8 ± 1.4	19.7 ± 1.2	25.4 ± 1.3	14.3 ± 0.9	12.1 ± 0.5

The EBSD inverse pole figure (IPF) image of a region of 1180 µm by 1056 µm taken in the XZ-plane of the as-deposited $AlCoCrFeNiTi_{0.5}$ alloy is given in Figure 5a. Each individual grain in the IPF image was color-coded based on the relationship between its crystallographic orientation and the building direction, which was vertically upwards (Z direction indicated in Figure 5a). There was no obvious preferred

crystallographic texture developed in the alloy because the grains were randomly color-coded. It revealed the equiaxed grains from the IPF image. Moreover, the histogram of the grain size measurement is illustrated in Figure 5b. The grain size measured by the vertical intercept was approximately 20.3 μm and was 21.1 μm along with the horizontal intercept. It has been acknowledged that, for a specific alloy, the temperature gradient G and the solidification rate R determine the solidification microstructure during the laser process. As the advancing laser moved away from the substrate, the melt pool retreated, and the solidification from moved upward, which led to the temperature field to low G and high R and the formation of the equiaxed grains. A recent study demonstrated that B2-structured dendrites were frequently fragmented, providing profuse effective nucleation sites, and therefore, promoted equiaxed grain formation in the $AlCoCrFeNiTi_{0.5}$ HEA [37].

Table 3. The chemical mixing enthalpies of element pairs and atomic size [9,10].

Element	Al	Co	Cr	Fe	Ni	Ti
(Atomic Size, nm)	(0.143)	(0.125)	(0.127)	(0.127)	(0.125)	(0.145)
Al	-	−19	−10	−11	−22	−30
Co	-	-	−4	−1	0	−28
Cr	-	-	-	−1	−7	−7
Fe	-	-	-	-	−2	−17
Ni	-	-	-	-	-	−35

Figure 6 presents the microhardness of $AlCoCrFeNiTi_{0.5}$ (Al1.0Ti0.5) HEA and Ti6Al4V (Ti64) substrate. Those of AlCoCrFeNi (Al1.0), $CrCuFeNi_2$ (Al0), $Al_{0.75}CrCuFeNi_2$ (Al0.75), and AISI 304 stainless steel substrate (304 SS) alloys reported in our previous work are shown for comparison [17,18]. The addition of Ti into the AlCoCrFeNi system enhanced the microhardness from 418 HV (Al1.0) to 634 HV (Al1.0Ti0.5), which was about 2.1 times that of the Ti6Al4V substrate. Since Ti has a

larger atomic radius than Al (as in Table 3), it would increase lattice distortion and improve the effect of solid solution strengthening. Our previous study reported that Al0 and Al0.75 possessed FCC phase structures, making them less resistant towards localized plastic deformation, thereby exhibiting low hardness (170 HV and 290 HV, respectively). The BCC phase consisted of a decreased number of dislocation slip systems compared to the FCC phase, which could explain the high hardness of $AlCoCrFeNiTi_{0.5}$ HEA in this work.

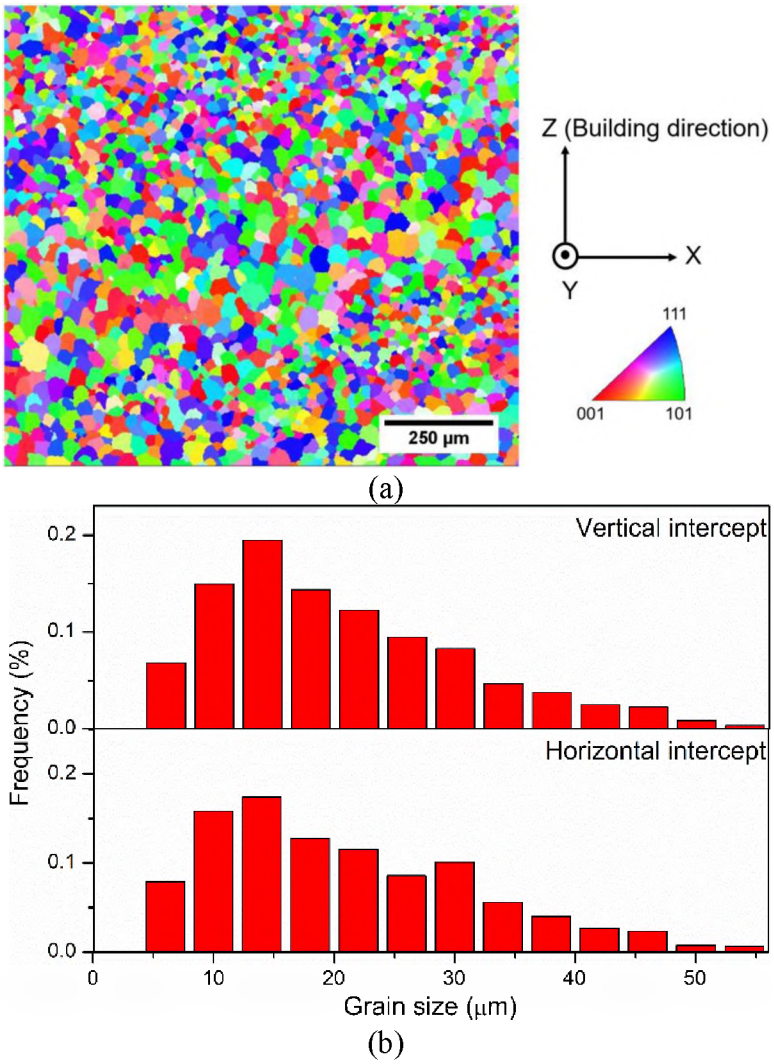

Figure 5. (a) Electron backscatter diffraction (EBSD) - inverse pole figure (IPF) map of the XZ-plane in the as-deposited HEA sample, and (b) histogram of the grain size measurement.

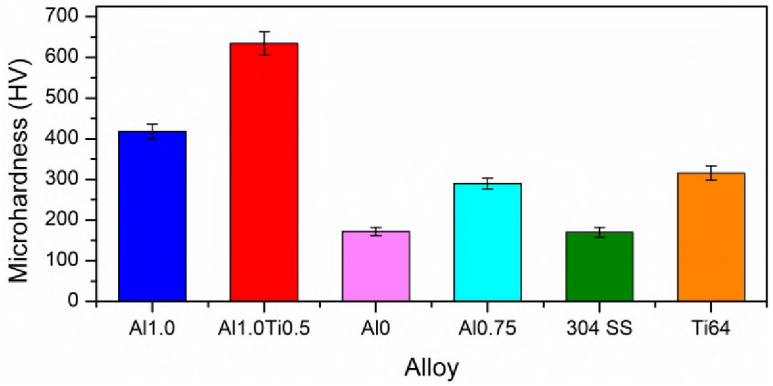

Figure 6. Microhardness of various alloys [7,8].

3.2. OXIDATION BEHAVIOR

3.2.1. Oxidation Kinetics. Figure 7 displays the isothermal oxidation results of the $AlCoCrFeNiTi_{0.5}$ HEA and Ti6Al4V at different temperatures (700 °C and 800 °C), over a period of 45 h in the air atmosphere. As illustrated in Figure 7a, the weight gains (ΔW) of the HEA were found to be 0.23 mg/cm^2 and 0.61 mg/cm^2 at 700 °C and 800 °C, respectively. For the Ti6Al4V alloy, its mass gain was measured at 5.87 mg/cm^2 at 700 °C, and its curve was recorded only within 20 h due to the scale spalling at 800 °C. The oxidation curves were observed to follow the parabolic form. The results of the parabolic rate law plot are shown in Figure 7b–d. Here, the parabolic rate constant, K_p can be considered as a measure of the oxidation resistance, and it was calculated using the Equation (1).

$$(\frac{\Delta W}{A})^2 = K_p \times t + C \quad (1)$$

where ΔW is the mass gain (mg/cm^2), A represents the unit area, K_p is the parabolic rate constant in mg^{2}cm^{-4}h^{-1}, t is the oxidation time (h), and C is a constant value. In addition, the coefficient determination R^2 values (>0.95) indicate that the parabolic model fits well

with the observations in Figure 7b–d. The K_p values were determined as 0.8501 (Ti6Al4V at 700 °C), 0.0011 (HEA at 700 °C) and 0.0077 $mg^2cm^{-4}h^{-1}$ (HEA at 800 °C). For discussion in Section 3.3, the K_p values were converted to the unit of $g^2cm^{-4}s^{-1}$, i.e., 2.36×10^{-10} (Ti6Al4V at 700 °C), 3.06×10^{-13} (HEA at 700 °C), and 2.14×10^{-12} (HEA at 800 °C). Hence, better oxidation resistance was observed with the HEA as its low weight gain and parabolic rate constant.

3.2.2. Phase Analysis. XRD analyses were performed following oxidation tests, and the results are indicated in Figure 8. The strong diffraction peaks of TiO_2 and weak diffraction peaks of Al_2O_3 were seen from the Ti6Al4V substrate, as in Figure 8a. This illustrated that the scale formed on the Ti6Al4V substrate was mostly composed of TiO_2 and a small amount of Al_2O_3. The TiO_2 was a poorly adherent and brittle scale, and Ti and O ions could diffuse through the porous oxides, which resulted in the fast oxidation kinetics. A thick oxide scale was formed and cracked due to the thermal stress at the elevated temperature [2].

For the $AlCoCrFeNiTi_{0.5}$ alloy oxidized at 700 °C, Al_2O_3, together with B2 and A2 phases were detected, as shown in Figure 8b. When oxidized at 800 °C, the oxides were Cr_2O_3, TiO_2, Al_2O_3, and spinel (mainly composed of $NiCr_2O_4$), as in Figure 8c. Besides, a Fe-Cr sigma phase with a tetragonal structure ($P4_2/mmm$, 136) was detected in $AlCoCrFeNiTi_{0.5}$ alloy oxidized shown in Figure 8b. A similar phenomenon was described by Wang et al., in which the transformation occurred from BCC to sigma phase at 650 °C [38,39].

3.2.3. Cross-Section Morphology of Oxidate Scales. The cross-sectional backscattered electron images and the elemental composition distribution of the Ti6Al4V

and $AlCoCrFeNiTi_{0.5}$ HEA oxidized at 700 °C and 800 °C are present in Figure 9. The oxide scales of the Ti6Al4V had a thickness of 25.54 ± 1.85 μm and they were loose, porous, and some cracks can be observed in Figure 9a. Its main composition was TiO_2, as the content of Ti was ~25–28 atom% and ~47–60 atom% of O (as in Figure 9b).

EDS mapping analysis of the cross-sectional HEA oxidized at 700 °C and 800 °C was performed to reveal the oxide scales better, and the results are shown in Figures 10a-h and 11a-h. The thickness of the scale on the HEA oxidized at 700 °C was about 1.73 ± 0.14 μm, of which it mainly contained Al_2O_3 (Al: ~15–17 atom%, O: 50–55 atom%, Ni, Cr, Co, Ti: below 10 atom% as in Figures 9c,d) and this was consistent with the observation in Figure 10. The thickness of the scale on the HEA reached to 5.12 ± 0.37 μm at 800 °C in Figure 9e, corresponding to that the scale thickness increased with the oxidation temperature. The scale structure mainly comprised of TiO_2 (Ti: ~20–22 atom%, O: ~63–66 atom%), Cr_2O_3 (Cr: ~18–21 atom%, O: ~ 53–56 atom%) and Al_2O_3 (Al: ~17–19 atom%, O:~48–50 atom%) for the oxidized HEA at 800 °C (Figure 9f). The thickness of each layer was measured at 0.96 μm for the TiO_2, 1.69 μm for the Cr_2O_3, and 2.51 μm for the Al_2O_3. This HEA mainly formed an outermost TiO_2 scale, an innermost continuous Al_2O_3 layer, and a Cr_2O_3 layer in-between, as illustrated in Figures 11a-e. The formation of the continuous Cr_2O_3 and Al_2O_3 layers can actually limit the diffusion of oxygen [40], providing excellent oxidation resistance at high temperatures.

3.3. DISCUSSION ON THE OXIDATION BEHAVIOR

The oxidation mechanism of Ti6Al4V and $AlCoCrFeNiTi_{0.5}$ HEA can be obtained from the above analysis. The predominant oxide in Ti6Al4V is TiO_2, with a small amount

of Al_2O_3 at 700 °C. Since TiO_2 is brittle and loose in the oxide film, it is vulnerable to detach from the substrate when it comes to high-temperature oxidation.

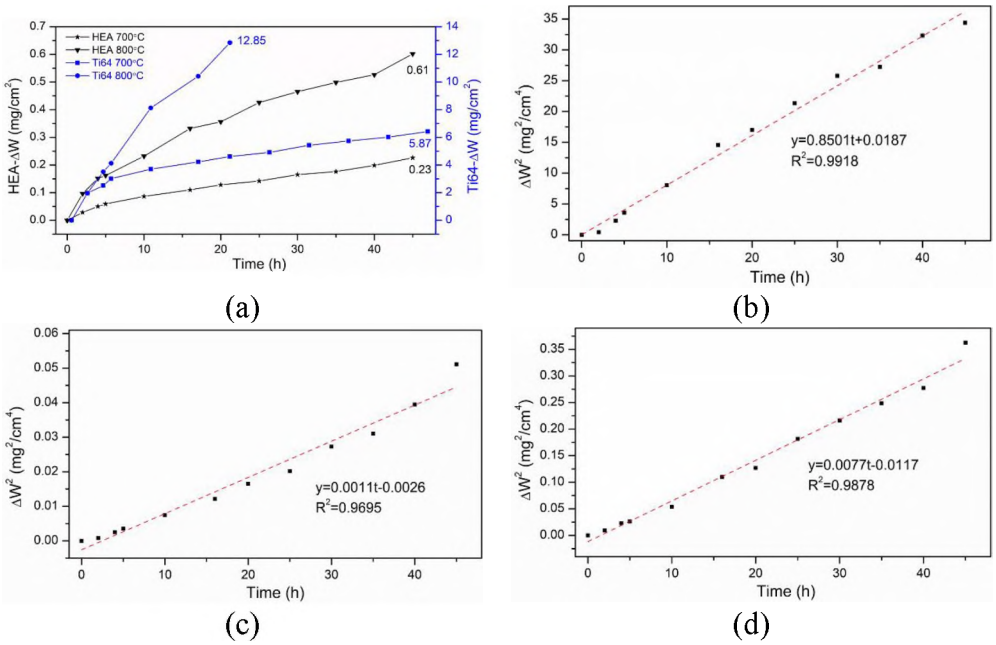

Figure 7. Isothermal oxidation results of $AlCoCrFeNiTi_{0.5}$ HEA and Ti6Al4V at 700 °C and 800 °C for 45 h; (a) weight gain versus oxidation time curves, the parabolic plot for (b)Ti6Al4V at 700 °C, (c) HEA at 700 °C and (d) HEA at 800 °C.

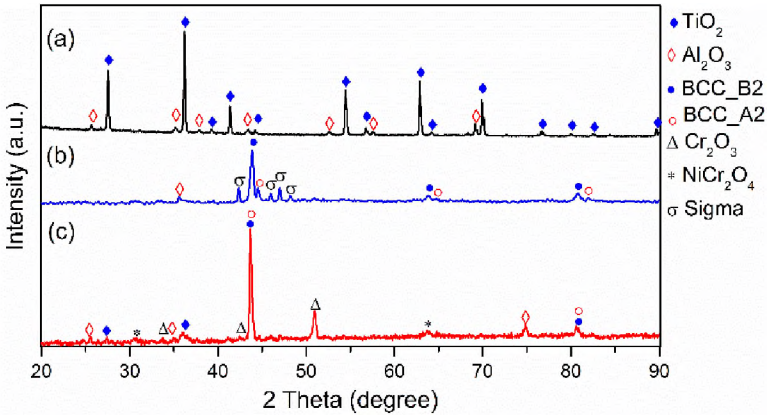

Figure 8. XRD patterns of the oxidized (a) Ti6Al4V at 700 °C, (b) HEA at 700 °C, and (c) HEA at 800 °C for 45 h.

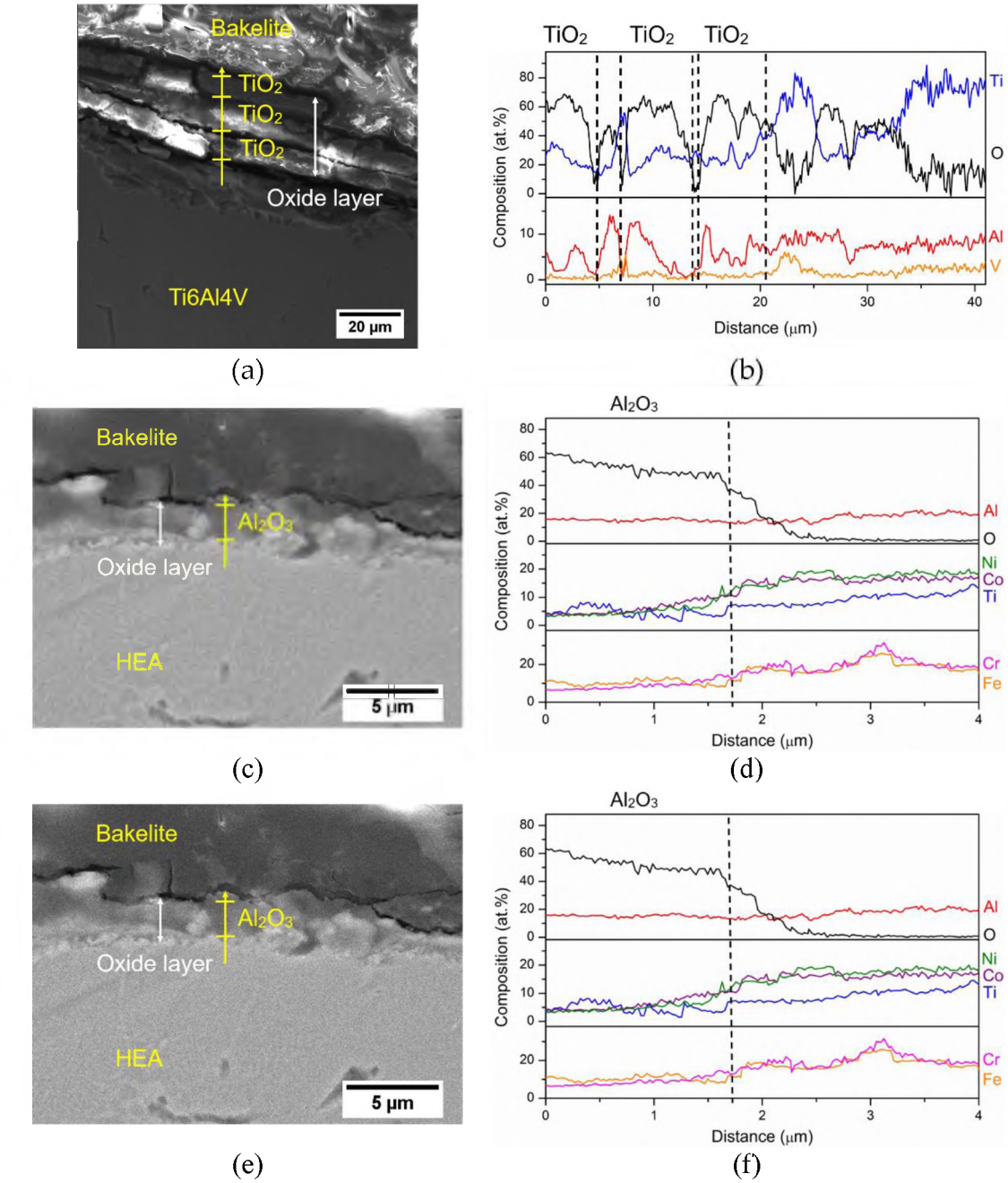

Figure 9. Cross-sectional backscattered electron images and the corresponding elemental composition distribution along the yellow arrow for the oxidized: (a) and (b) Ti6Al4V at 700 °C, (c) and (d) HEA at 700 °C, (e) and (f) HEA at 800 °C for 45 h.

For the $AlCoCrFeNiTi_{0.5}$ HEA, it is slightly oxidized at 700 °C, as a thin Al_2O_3 oxide layer is observed, and the Fe-Cr sigma phase occurs due to the phase

transformation. The Al, Cr, and Ti are selectively oxidized and diffuses and enriches into the oxide layer at 800 °C. The TiO_2 is distributed in the outermost oxide layer, and continuous protective Cr_2O_3 and Al_2O_3 scales are located beneath the TiO_2 layer. The behavior of the $AlCoCrFeNiTi_{0.5}$ HEA is similar to Group II in Ni-Cr-Al alloy systems [25,41]. The oxide map can be explained that the concentrations of Al and Cr facilitate the external Cr_2O_3 with an internal subscale Al_2O_3 scale. In a review of thermodynamic data, the standard Gibbs free energy of Al_2O_3 (−891 KJ/mol at 800 °C) formation is more negative than other possible oxides (i.e., Cr_2O_3: −569 KJ/mol) in the HEA [42], the growth of Al_2O_3 should be favorable during the initial stage of oxidation.

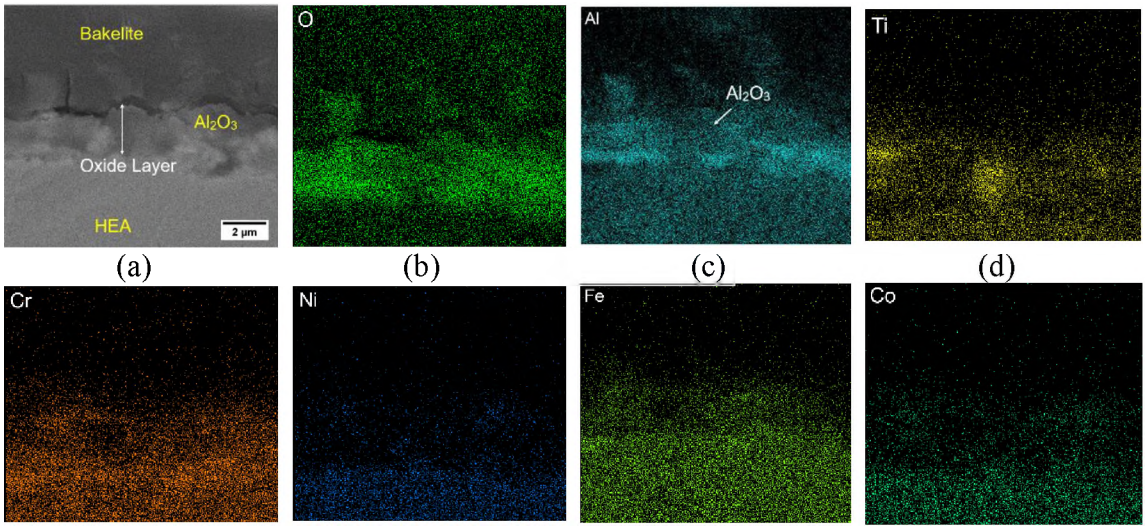

Figure 10. (a) Backscattered electron image and the corresponding (b) O, (c) Al, (d) Ti, (e) Cr, (f) Ni, (g) Fe and (h) Co EDS maps of the oxide scales on $AlCoCrFeNiTi_{0.5}$ HEA oxidized at 700 °C for 45 h.

It is important and interesting to compare the oxidation rates from our work with other HEAs and conventional alloys. Table 4 collects the parabolic constants K_p

measured for different HEAs (CrMnFeCoNi, FeCoNiCrAl and $Al_{0.5}CoCrFeNiTi_{0.5}$) and alumina-forming austenitic (AFA) stainless steel. It is worth noting that the examined HEAs are comparable to those similar types of HEAs. The $AlCoCrFeNiTi_{0.5}$ HEA is believed to own good oxidation properties due to the sluggish diffusion effect and formation of Al_2O_3 and Cr_2O_3 oxides. However, its oxidation resistance is shown to fall short of FeCoNiCrAl, $Al_{1.5}CoCrFeNiTi_{0.5}$ and AFA steel, i.e., 2–3 order of differences in K_p values. According to Butler et al. [24,25], increased Al content enhanced the continuity of the Al_2O_3 scale, leading to improved oxidation resistance. The formed alumina could exhibit a protective effect at low Ti content. With the addition of Ti, it negatively affected the oxidation behavior of the aluminum-containing HEAs. As described in Erdogan's work [43], a good barrier against oxidation did not form in the Ti-rich $CoCrFeNiAl_{0.5}Ti$ due to the fast-growing oxides.

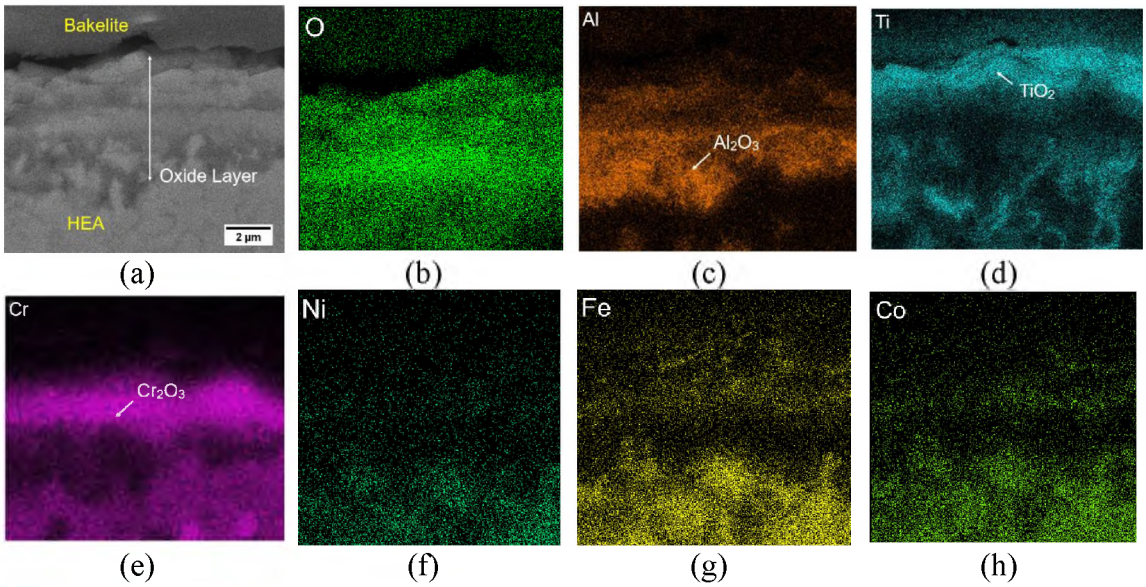

Figure 11. (a) Backscattered electron image and the corresponding (b) O, (c) Al, (d) Ti, (e) Cr, (f) Ni, (g) Fe and (h) Co EDS maps of the oxide scales on $AlCoCrFeNiTi_{0.5}$ HEA oxidized at 800 °C for 45 h.

Table 4. The values of the parabolic constants for various alloys.

Alloy	K_p ($g^2mg^{-4}s^{-1}$)	Temperature (°C)	Reference
$AlCoCrFeNiTi_{0.5}$	3.06×10^{-13}	700	This work
	2.14×10^{-12}	800	
CrMnFeCoNi	5.47×10^{-12}	700	[44]
	1.67×10^{-11}	800	
FeCoNiCrAl	8.5×10^{-15}	700	[45]
	4.0×10^{-14}	800	
$Al_{1.5}CoCrFeNiTi_{0.5}$	1.66×10^{-14}	700	[46]
14Cr-25Ni-3.5Al AFA steel	3×10^{-14}	850	[47]
22Cr-25Ni-2.5Al AFA steel	9.19×10^{-15}	700	[48]
	3.55×10^{-14}	800	

Based on these facts, the laser processed $AlCoCrFeNiTi_{0.5}$ HEA has great potential under the high-temperature application. A great effort should be put on (1) the investigation of the sequence of oxide formation at the early stage, and (2) the improvement of the oxidation resistance by alloying addition, e.g., Al, Si.

4. CONCLUSION

The $AlCoCrFeNiTi_{0.5}$ high-entropy alloy (HEA) coating was fabricated by laser metal deposition (LMD) on a Ti6Al4V substrate. The microstructure and isothermal oxidation behavior at 700 °C and 800 °C in air atmosphere were investigated, and the underlying mechanisms were discussed. The main phase constitutions in as-deposited HEA were the Fe, Cr-rich A2 and Al, Ni, and Ti-enriched B2 phases. The isothermal oxidation testing demonstrated that the HEA coatings could effectively improve the oxidation resistance of the Ti6Al4V substrate. The oxidation kinetics of the HEA and Ti6Al4V met the parabolic rate law, while the weight gain and parabolic rate constant of

the HEA were lower than Ti6Al4V, implying a better oxidation resistance. The scales of the Ti6Al4V were mainly composed of TiO_2 at 700 °C, and it suffered from spalling at 800 °C. The $AlCoCrFeNiTi_{0.5}$ HEA was slightly oxidized at 700 °C as a few oxides were formed. At 800 °C, the formation of continuous Al_2O_3, Cr_2O_3 scales could be ascribed to their good oxidation resistance of the HEA. This work provides an approach to enhance the oxidation resistance of Ti6Al4V alloy and accelerate the broad adoption of HEAs in high-temperature applications.

ACKNOWLEDGMENTS

This work was funded by financial support from NSF (National Science Foundation) grants CMMI-1625736 and EEC-1937128, and Intelligent System Center (ISC) at Missouri University of Science and Technology (Missouri S&T). The materials preparation and characterization were supported by the Materials Research Center (MRC) at Missouri S&T.

REFERENCES

[1] H. Guleryuz and H. Cimenoglu, "Oxidation of Ti-6Al-4V alloy," *J. Alloys Compd.*, vol. 472, no. 1–2, pp. 241–246, Mar. 2009.

[2] C. Huang, Y. Zhang, J. Shen, and R. Vilar, "Thermal stability and oxidation resistance of laser clad TiVCrAlSi high entropy alloy coatings on Ti-6Al-4V alloy," Surf. Coatings Technol., vol. 206, no. 6, pp. 1389–1395, Dec. 2011.

[3] F. Weng, C. Chen, and H. Yu, "Research status of laser cladding on titanium and its alloys: A review," Materials and Design, vol. 58. Elsevier Ltd, pp. 412–425, 01-Jun-2014.

[4] Y. H. Lv, J. Li, Y. F. Tao, and L. F. Hu, "High-temperature wear and oxidation behaviors of TiNi/Ti 2 Ni matrix composite coatings with TaC addition prepared on Ti6Al4V by laser cladding," Appl. Surf. Sci., vol. 402, pp. 478–494, Apr. 2017.

[5] S. Kumar, T. S. N. Sankara Narayanan, S. Ganesh Sundara Raman, and S. K. Seshadri, "Thermal oxidation of Ti6Al4V alloy: Microstructural and electrochemical characterization," Mater. Chem. Phys., vol. 119, no. 1–2, pp. 337–346, Jan. 2010.

[6] Z. Y. Zhou et al., "Laser in-situ synthesizing Ti5Si3/Al3Ni2 reinforced Al3Ti/NiTi composite coatings: Microstructure, mechanical characteristics and oxidation behavior," Opt. Laser Technol., vol. 109, pp. 99–109, Jan. 2019.

[7] L. D. Bobbio et al., "Additive manufacturing of a functionally graded material from Ti-6Al-4V to Invar: Experimental characterization and thermodynamic calculations," Acta Mater., vol. 127, pp. 133–142, Apr. 2017.

[8] A. Reichardt et al., "Development and characterization of Ti-6Al-4V to 304L stainless steel gradient components fabricated with laser deposition additive manufacturing," Mater. Des., vol. 104, pp. 404–413, Aug. 2016.

[9] W. Li, A. Ghazanfari, D. McMillen, M. C. Leu, G. E. Hilmas, and J. Watts, "Characterization of zirconia specimens fabricated by ceramic on-demand extrusion," Ceram. Int., vol. 44, no. 11, pp. 12245–12252, Aug. 2018.

[10] W. Li, A. Ghazanfari, D. McMillen, M. C. Leu, G. E. Hilmas, and J. Watts, "Fabricating ceramic components with water dissolvable support structures by the Ceramic On-Demand Extrusion process," CIRP Ann. - Manuf. Technol., vol. 66, no. 1, pp. 225–228, Jan. 2017.

[11] W. Cui, Y. Zhang, X. Zhang, L. Li, and F. Liou, "Metal Additive Manufacturing Parts Inspection Using Convolutional Neural Network," Appl. Sci., vol. 10, no. 2, p. 545, Jan. 2020.

[12] H. Liu, X. Zhang, Y. Jiang, and R. Zhou, "Microstructure and high temperature oxidation resistance of in-situ synthesized TiN/Ti3Al intermetallic composite coatings on Ti6Al4V alloy by laser cladding process," J. Alloys Compd., vol. 670, pp. 268–274, Jun. 2016.

[13] J. C. Zambrano Carrullo, J. C. Pereira Falcón, and V. Amigó Borrás, "Influence of process parameters and initial microstructure on the oxidation resistance of Ti48Al2Cr2Nb coating obtained by laser metal deposition," Surf. Coatings Technol., vol. 358, pp. 114–124, Jan. 2019.

[14] F. Liu, Y. Mao, X. Lin, B. Zhou, and T. Qian, "Microstructure and high temperature oxidation resistance of Ti-Ni gradient coating on TA2 titanium alloy fabricated by laser cladding," Opt. Laser Technol., vol. 83, pp. 140–147, Sep. 2016.

[15] X. B. Liu and H. M. Wang, "Microstructure, wear and high-temperature oxidation resistance of laser clad Ti5Si3/γ/TiSi composite coatings on γ-TiAl intermetallic alloy," Surf. Coatings Technol., vol. 200, no. 14–15, pp. 4462–4470, Apr. 2006.

[16] J.-W. Yeh et al., "Nanostructured High-Entropy Alloys with Multiple Principal Elements: Novel Alloy Design Concepts and Outcomes," Adv. Eng. Mater., vol. 6, no. 5, pp. 299–303, May 2004.

[17] W. Cui, S. Karnati, X. Zhang, E. Burns, and F. Liou, "Fabrication of AlCoCrFeNi High-Entropy Alloy Coating on an AISI 304 Substrate via a CoFe2Ni Intermediate Layer," Entropy, vol. 21, no. 1, p. 2, Dec. 2019.

[18] W. Cui, X. Zhang, L. Li, Y. Chen, T. Pan, and F. Liou, "Fabrication and characterization of AlxCrCuFeNi2 high-entropy alloys coatings by laser metal deposition," in Procedia Manufacturing, 2019, vol. 39, pp. 509–518.

[19] Y. P. Wang, B. S. Li, M. X. Ren, C. Yang, and H. Z. Fu, "Microstructure and compressive properties of AlCrFeCoNi high entropy alloy," Mater. Sci. Eng. A, vol. 491, no. 1–2, pp. 154–158, Sep. 2008.

[20] Z. Tang et al., "Tensile ductility of an AlCoCrFeNi multi-phase high-entropy alloy through hot isostatic pressing (HIP) and homogenization," Mater. Sci. Eng. A, vol. 647, pp. 229–240, Oct. 2015.

[21] R. Wang, K. Zhang, C. Davies, and X. Wu, "Evolution of microstructure, mechanical and corrosion properties of AlCoCrFeNi high-entropy alloy prepared by direct laser fabrication," J. Alloys Compd., vol. 694, pp. 971–981, Feb. 2017.

[22] K. Y. Tsai, M. H. Tsai, and J. W. Yeh, "Sluggish diffusion in Co-Cr-Fe-Mn-Ni high-entropy alloys," Acta Mater., vol. 61, no. 13, pp. 4887–4897, Aug. 2013.

[23] Z. S. Nong, Y. N. Lei, and J. C. Zhu, "Wear and oxidation resistances of AlCrFeNiTi-based high entropy alloys," Intermetallics, vol. 101, pp. 144–151, Oct. 2018.

[24] A. Mohanty et al., "High temperature oxidation study of direct laser deposited AlXCoCrFeNi (X=0.3,0.7) high entropy alloys," Surf. Coatings Technol., vol. 380, p. 125028, Dec. 2019.

[25] T. M. Butler and M. L. Weaver, "Oxidation behavior of arc melted AlCoCrFeNi multi-component high-entropy alloys," J. Alloys Compd., vol. 674, pp. 229–244, Jul. 2016.

[26] T. M. Butler, J. P. Alfano, R. L. Martens, and M. L. Weaver, "High-Temperature Oxidation Behavior of Al-Co-Cr-Ni-(Fe or Si) Multicomponent High-Entropy Alloys," JOM, vol. 67, no. 1, pp. 246–259, Nov. 2015.

[27] J. Dąbrowa et al., "Influence of Cu content on high temperature oxidation behavior of AlCoCrCuxFeNi high entropy alloys (x = 0; 0.5; 1)," Intermetallics, vol. 84, pp. 52–61, May 2017.

[28] R. Feng et al., "Phase stability and transformation in a light-weight high-entropy alloy," Acta Mater., vol. 146, pp. 280–293, Mar. 2018.

[29] M. Löbel, T. Lindner, T. Mehner, and T. Lampke, "Influence of Titanium on Microstructure, Phase Formation and Wear Behaviour of AlCoCrFeNiTix High-Entropy Alloy," Entropy, vol. 20, no. 7, p. 505, Jul. 2018.

[30] S. Jiang, Z. Lin, H. Xu, and Y. Sun, "Studies on the microstructure and properties of AlxCoCrFeNiTi1-x high entropy alloys," J. Alloys Compd., vol. 741, pp. 826–833, Apr. 2018.

[31] L. H. Tian, W. Xiong, C. Liu, S. Lu, and M. Fu, "Microstructure and Wear Behavior of Atmospheric Plasma-Sprayed AlCoCrFeNiTi High-Entropy Alloy Coating," J. Mater. Eng. Perform., vol. 25, no. 12, pp. 5513–5521, Dec. 2016.

[32] Q. H. Li, T. M. Yue, Z. N. Guo, and X. Lin, "Microstructure and corrosion properties of alcocrfeni high entropy alloy coatings deposited on AISI 1045 steel by the electrospark process," Metall. Mater. Trans. A Phys. Metall. Mater. Sci., vol. 44, no. 4, pp. 1767–1778, Apr. 2013.

[33] Y. Yu, J. Wang, J. Li, H. Kou, and W. Liu, "Characterization of BCC phases in AlCoCrFeNiTix high entropy alloys," Mater. Lett., vol. 138, pp. 78–80, Jan. 2015.

[34] L. D. Bobbio et al., "Characterization of a functionally graded material of Ti-6Al-4V to 304L stainless steel with an intermediate V section," J. Alloys Compd., vol. 742, pp. 1031–1036, Apr. 2018.

[35] S. Chen, M. Zhang, J. Huang, C. Cui, H. Zhang, and X. Zhao, "Microstructures and mechanical property of laser butt welding of titanium alloy to stainless steel," Mater. Des., vol. 53, pp. 504–511, Jan. 2014.

[36] E. M. M. H. Okamoto, M.E. Schlesinger, Ed., "Fe (Iron) Binary Alloy Phase Diagrams," in Alloy Phase Diagrams, ASM International, 2018, pp. 340–361.

[37] S. Guan et al., "Formation of fully equiaxed grain microstructure in additively manufactured AlCoCrFeNiTi0.5 high entropy alloy," Mater. Des., vol. 184, p. 108202, Dec. 2019.

[38] Y. Yu, J. Wang, J. Li, J. Yang, H. Kou, and W. Liu, "Tribological Behavior of AlCoCrFeNi(Ti0.5) High Entropy Alloys under Oil and MACs Lubrication," J. Mater. Sci. Technol., vol. 32, no. 5, pp. 470–476, May 2016.

[39] A. Munitz, S. Salhov, S. Hayun, and N. Frage, "Heat treatment impacts the micro-structure and mechanical properties of AlCoCrFeNi high entropy alloy," J. Alloys Compd., vol. 683, pp. 221–230, Oct. 2016.

[40] W. T. Chen, B. Gleeson, and A. Heuer, "Oxidation Behavior of γ'-Ni_3Al-Based Ni–20Al–5Cr Alloys With and Without Reactive Elements Under Different Heating Conditions," Oxid. Met., vol. 92, no. 3–4, pp. 137–150, Oct. 2019.

[41] C. S. Giggins and F. S. Pettit, "Oxidation of Ni-Cr-Al Alloys Between 1000° and 1200°C," J. Electrochem. Soc., vol. 118, no. 11, p. 1782, 1971.

[42] P. Zhang, Y. Li, Z. Chen, J. Zhang, and B. Shen, "Oxidation response of a vacuum arc melted NbZrTiCrAl refractory high entropy alloy at 800–1200 °C," Vacuum, vol. 162, pp. 20–27, Apr. 2019.

[43] A. Erdogan, K. M. Doleker, and S. Zeytin, "Effect of Al and Ti on High-Temperature Oxidation Behavior of CoCrFeNi-Based High-Entropy Alloys," JOM, vol. 71, no. 10, pp. 3499–3510, Oct. 2019.

[44] G. Laplanche, U. F. Volkert, G. Eggeler, and E. P. George, "Oxidation Behavior of the CrMnFeCoNi High-Entropy Alloy," Oxid. Met., vol. 85, no. 5–6, pp. 629–645, Jun. 2016.

[45] W. Kai et al., "Air-oxidation of FeCoNiCr-based quinary high-entropy alloys at 700–900 °C," Corros. Sci., vol. 121, pp. 116–125, Jun. 2017.

[46] S. Wang, Z. Chen, P. Zhang, K. Zhang, C. L. Chen, and B. L. Shen, "Influence of Al content on high temperature oxidation behavior of Al x CoCrFeNiTi 0.5 high entropy alloys," Vacuum, vol. 163, pp. 263–268, May 2019.

[47] S. Rashidi, J. P. Choi, J. W. Stevenson, A. Pandey, and R. K. Gupta, "Effect of Aluminizing on the High-Temperature Oxidation Behavior of an Alumina-Forming Austenitic Stainless Steel," JOM, vol. 71, no. 1, pp. 109–115, Jan. 2019.

[48] J. Wang et al., "The Influence of Temperature on the Oxidation Mechanism in Air of HR3C and Aluminum-Containing 22Cr–25Ni Austenitic Stainless Steels," Oxid. Met., vol. 89, no. 5–6, pp. 713–730, Jun. 2018.

SECTION

2. CONCLUSIONS

The fabrication of a novel high-entropy alloy (HEA) was fabricated from elemental powders using laser metal deposition (LMD). The microstructure, mechanical properties, and oxidation behavior of as-fabricated HEA have been investigated in the current work. In the first work, $Al_xCrCuFeNi_2$ (x = 0,0.75 in molar ratios) HEAs were coated on AISI 304 stainless steel substrate via laser metal deposition technology. Good metallurgical bonding was observed between the HEA coatings and the substrate. The $Al_xCrCuFeNi_2$ (x = 0,0.75) HEAs coating exhibited columnar dendritic microstructure and FCC structure identified by EBSD.

Next, an AlCoCrFeNi HEA was coated on an AISI 304 substrate by LMD technology. The coating on the substrate without and with the intermediate layer was characterized and discussed. Cracking was prominent when the AlCoCrFeNi HEA was directly coated on the AISI 304 substrate due to the compositional change between HEA and the substrate. Using an intermediate layer of $CoFe_2Ni$ improved the bond. The incorporation of the intermediate layer successfully eliminated crack formation in the deposit.

The oxidation behavior of the HEA was further investigated. The $AlCoCrFeNiTi_{0.5}$ HEA coating was fabricated on a Ti6Al4V substrate. The microstructure and isothermal oxidation behavior at 700 °C and 800 °C in air atmosphere were investigated, and the underlying mechanisms were discussed. The isothermal

oxidation testing demonstrated that the HEA coatings could effectively improve the oxidation resistance of the Ti6Al4V substrate. This work provides an approach to enhance the oxidation resistance of Ti6Al4V alloy and accelerate the broad adoption of HEAs in high-temperature applications.

At last, we presented a convolutional neural network (CNN) application for robust quality inspection of metal additive manufacturing (AM) parts. The Missouri S&T dataset, including optical microscope images of real-world metal AM parts were used to train and test the CNN model. This work contributed to developing a CNN model with excellent performance in recognizing good quality, crack, gas porosities, and a lack of fusion categories. Our final model achieved an accuracy of 92.1% with 8.01 milliseconds recognition time of one image. The results indicate the promising application of the CNN method in quality inspection in the AM industry. It would be interesting to explore more CNN architectures and include a variety of materials in the future.

3. RECOMMENDATIONS FOR FUTURE WORK

The novel AlCoCrFeNi high-entropy alloys (HEAs) have been fabricated by laser metal deposition (LMD) process. Significant progress has been made in terms of the gradient composition fabrication, microstructure, and oxidation behavior. These accomplishments will continue to motivate new research questions and to inspire major scientific themes. Some of these, for example, high-throughput computational and experimental methods, are essential tools to cope with the enormous composition combinations of HEAs. In addition to high-temperature oxidation performance, creep behavior and fatigue properties should also be studied to accelerate HEAs' real-world adoption.

This work established the new neural network-based methods in the metal additive manufacturing (AM) process. We can expect to see that vast amounts of data will be generated with AM's rapid development. However, these data's accessibility is not easy across different research groups, as these data in “these isolated islands” have inconsistent application programming interfaces (APIs) to call. Therefore, the collaboration among the process engineers, materials engineering, and computer scientist will significantly benefit from acquiring unified APIs. The hardware and software will be needed to provide reliable sensor and control systems. We can envision that the advanced deep learning algorithm will boost computational speed and performance. We can forecast that the overwhelming amount of deep learning efforts paid on AM materials and automated process feed-back systems will push forward the intelligent AM forward.

REFERENCES

[1] A. Ostovari Moghaddam, N. A. Shaburova, M. N. Samodurova, A. Abdollahzadeh, and E. A. Trofimov, "Additive manufacturing of high entropy alloys: A practical review," Journal of Materials Science and Technology, vol. 77. Chinese Society of Metals, pp. 131–162, 30-Jun-2021.

[2] M. Moorehead et al., "High-throughput synthesis of Mo-Nb-Ta-W high-entropy alloys via additive manufacturing," Mater. Des., vol. 187, p. 108358, Feb. 2020.

[3] M. A. Melia et al., "High-throughput additive manufacturing and characterization of refractory high entropy alloys," Appl. Mater. Today, vol. 19, p. 100560, Jun. 2020.

[4] W. Li, A. Ghazanfari, D. McMillen, M. C. Leu, G. E. Hilmas, and J. Watts, "Characterization of zirconia specimens fabricated by ceramic on-demand extrusion," Ceram. Int., vol. 44, no. 11, pp. 12245–12252, Aug. 2018.

[5] L. C. Zhang, Y. Liu, S. Li, and Y. Hao, "Additive Manufacturing of Titanium Alloys by Electron Beam Melting: A Review," Advanced Engineering Materials, vol. 20, no. 5. Wiley-VCH Verlag, 01-May-2018.

[6] W. Li, A. Ghazanfari, M. C. Leu, and R. G. Landers, "Extrusion-on-demand methods for high solids loading ceramic paste in freeform extrusion fabrication," Virtual Phys. Prototyp., vol. 12, no. 3, pp. 193–205, Jul. 2017.

[7] W. Li, A. Armani, D. McMillen, M. Leu, G. Hilmas, and J. Watts, "Additive manufacturing of zirconia parts with organic sacrificial supports," Int. J. Appl. Ceram. Technol., vol. 17, no. 4, pp. 1544–1553, Jul. 2020.

[8] P. Bajaj, A. Hariharan, A. Kini, P. Kürnsteiner, D. Raabe, and E. A. Jägle, "Steels in additive manufacturing: A review of their microstructure and properties," Mater. Sci. Eng. A, vol. 772, p. 138633, Jan. 2020.

[9] W. Li and M. C. Leu, "Material Extrusion Based Ceramic Additive Manufacturing," in ASM Handbook, vol. 24, D. Bourell, W. Frazier, H. Kuhn, and M. Seifi, Eds. ASM International, 2020, pp. 97–111.

[10] B. Wu et al., "A review of the wire arc additive manufacturing of metals: properties, defects and quality improvement," Journal of Manufacturing Processes, vol. 35. Elsevier Ltd, pp. 127–139, 01-Oct-2018.

[11] S. Singh, S. Ramakrishna, and R. Singh, "Material issues in additive manufacturing: A review," Journal of Manufacturing Processes, vol. 25. Elsevier Ltd, pp. 185–200, 01-Jan-2017.

[12] B. Li, L. Zhang, Y. Xu, Z. Liu, B. Qian, and F. Xuan, "Selective laser melting of CoCrFeNiMn high entropy alloy powder modified with nano-TiN particles for additive manufacturing and strength enhancement: Process, particle behavior and effects," Powder Technol., vol. 360, pp. 509–521, Jan. 2020.

[13] W. Li, A. Ghazanfari, D. Mcmillen, A. Scherff, M. C. Leu, and G. E. Hilmas, "Fabricating Zirconia Parts with Organic Support Material by the Ceramic On-Demand Extrusion Process," in Proceedings of the 28th Annual Solid Freeform Fabrication Symposium, 2017, pp. 605–615.

[14] M. Li, A. Ghazanfari, W. Li, R. G. Landers, and M. C. Leu, "Modeling and analysis of paste freezing in freeze-form extrusion fabrication of thin-wall parts via a lumped method," J. Mater. Process. Technol., vol. 237, pp. 163–180, Nov. 2016.

[15] L. Li et al., "Predictive model for thermal and stress field in selective laser melting process-Part I," in Procedia Manufacturing, 2019, vol. 39, pp. 539–546.

[16] Y. Kok et al., "Anisotropy and heterogeneity of microstructure and mechanical properties in metal additive manufacturing: A critical review," Mater. Des., vol. 139, pp. 565–586, Feb. 2018.

[17] L. Li et al., "Predictive model for thermal and stress field in selective laser melting process-Part II," in Procedia Manufacturing, 2019, vol. 39, pp. 547–555.

[18] A. Ghazanfari, W. Li, M.-C. Leu, G. Hilmas, M. C. Leu, and G. E. Hilmas, "A Novel Extrusion-Based Additive Manufacturing Process for Ceramic Parts," in Proceedings of the 27th Annual Solid Freeform Fabrication Symposium, 2016, pp. 1509–1529.

[19] A. Ghazanfari, W. Li, M. Leu, J. Watts, and G. Hilmas, "Mechanical characterization of parts produced by ceramic on-demand extrusion process," Int. J. Appl. Ceram. Technol., vol. 14, no. 3, pp. 486–494, May 2017.

[20] S. Liu and Y. C. Shin, "Additive manufacturing of Ti6Al4V alloy: A review," Mater. Des., vol. 164, p. 107552, Feb. 2019.

[21] H. Li et al., "Columnar to equiaxed transition in additively manufactured CoCrFeMnNi high entropy alloy," Mater. Des., vol. 197, p. 109262, Jan. 2021.

[22] W. Li, A. Ghazanfari, D. McMillen, M. C. Leu, G. E. Hilmas, and J. Watts, "Fabricating ceramic components with water dissolvable support structures by the Ceramic On-Demand Extrusion process," CIRP Ann. - Manuf. Technol., vol. 66, no. 1, pp. 225–228, Jan. 2017.

[23] W. Li, A. Ghazanfari, M. C. Leu, and R. G. Landers, "Methods of extrusion on demand for high solids loading ceramic paste in freeform extrusion fabrication," in Proceedings of the 26th Annual Solid Freeform Fabrication Symposium, 2015, pp. 332–345.

[24] A. Armani, W. Li, M. C. Leu, and R. G. Landers, "Optimal Rastering Orientation Freeform Extrusion Fabrication Process," in Proceedings of the 26th Annual Solid Freeform Fabrication Symposium, 2015, pp. 1324–1333.

[25] A. Armani, W. Li, M. C. Leu, and R. G. Landers, "Planning freeform extrusion fabrication processes with consideration of horizontal staircase effect," in Proceedings of the 26th Annual Solid Freeform Fabrication Symposium, 2015, pp. 1313–1323.

[26] A. Ghazanfari, W. Li, and M. C. Leu, "Adaptive rastering algorithm for freeform extrusion fabrication processes," Virtual Phys. Prototyp., vol. 10, no. 3, pp. 163–172, Jul. 2015.

[27] W. Cui, X. Zhang, L. Li, Y. Chen, T. Pan, and F. Liou, "Fabrication and characterization of AlxCrCuFeNi2 high-entropy alloys coatings by laser metal deposition," in Procedia Manufacturing, 2019, vol. 39, pp. 509–518.

[28] L. Yan et al., "Build Strategy Investigation of Ti-6Al-4V Produced Via a Hybrid Manufacturing Process," JOM, vol. 70, no. 9, pp. 1706–1713, Sep. 2018.

[29] X. Zhang, W. Cui, W. Li, and F. Liou, "A Hybrid Process Integrating Reverse Engineering, Pre-Repair Processing, Additive Manufacturing, and Material Testing for Component Remanufacturing," Materials (Basel)., vol. 12, no. 12, p. 1961, Jun. 2019.

[30] L. Li, X. Zhang, W. Cui, F. Liou, W. Deng, and W. Li, "Temperature and residual stress distribution of FGM parts by DED process: modeling and experimental validation," Int. J. Adv. Manuf. Technol., vol. 109, no. 1–2, pp. 451–462, Jul. 2020.

[31] D. Gu, "Materials creation adds new dimensions to 3D printing," Sci. Bull., vol. 61, no. 22, pp. 1718–1722, Nov. 2016.

[32] T. Pan et al., "Characteristics of Inconel 625—copper bimetallic structure fabricated by directed energy deposition," Int. J. Adv. Manuf. Technol., vol. 109, no. 5–6, pp. 1261–1274, Jul. 2020.

[33] C. H. Hung, W. T. Chen, M. H. Sehhat, and M. C. Leu, "The effect of laser welding modes on mechanical properties and microstructure of 304L stainless steel parts fabricated by laser-foil-printing additive manufacturing," Int. J. Adv. Manuf. Technol., pp. 1–11, Nov. 2020.

[34] K. Schmidtke, F. Palm, A. Hawkins, and C. Emmelmann, "Process and mechanical properties: Applicability of a scandium modified Al-alloy for laser additive manufacturing," in Physics Procedia, 2011, vol. 12, no. PART 1, pp. 369–374.

[35] T. D. Ngo, A. Kashani, G. Imbalzano, K. T. Q. Nguyen, and D. Hui, "Additive manufacturing (3D printing): A review of materials, methods, applications and challenges," Composites Part B: Engineering, vol. 143. Elsevier Ltd, pp. 172–196, 15-Jun-2018.

[36] X. Zhang, W. Li, X. Chen, W. Cui, and F. Liou, "Evaluation of component repair using direct metal deposition from scanned data," Int. J. Adv. Manuf. Technol., vol. 95, no. 9–12, pp. 3335–3348, Apr. 2018.

[37] X. Zhang, W. Cui, W. Li, and F. Liou, "Effects of tool path in remanufacturing cylindrical components by laser metal deposition," Int. J. Adv. Manuf. Technol., vol. 100, no. 5–8, pp. 1607–1617, Feb. 2019.

[38] P. Parandoush and D. Lin, "A review on additive manufacturing of polymer-fiber composites," Composite Structures, vol. 182. Elsevier Ltd, pp. 36–53, 15-Dec-2017.

[39] K. C. R. Kolan, W. Li, R. Althage, J. A. Semon, D. E. Day, and M. C. Leu, "Solvent and melt based extrusion 3D printing of polycaprolactone bioactive glass composite for tissue engineering," in Proceedings of the International Conference on Progress in Additive Manufacturing, 2018, vol. 2018-May, pp. 176–182.

[40] C. Murphy, K. Kolan, and W. Li, "3D bioprinting of stem cells and polymer/bioactive glass composite scaffolds for bone tissue engineering," Int. J. Bioprinting, vol. 3, no. 1, pp. 1–11, 2017.

[41] W. Li et al., "Properties of Partially Stabilized Zirconia Components Fabricated by the Ceramic On-Demand Extrusion Process," in Proceedings of the 27th Annual Solid Freeform Fabrication Symposium, 2016, pp. 916–928.

[42] A. Ghazanfari, W. Li, M. C. Leu, J. L. Watts, and G. E. Hilmas, "Additive manufacturing and mechanical characterization of high density fully stabilized zirconia," Ceram. Int., vol. 43, no. 8, pp. 6082–6088, Jun. 2017.

[43] N. Travitzky et al., "Additive manufacturing of ceramic-based materials," in Advanced Engineering Materials, 2014, vol. 16, no. 6, pp. 729–754.

[44] A. Ghazanfari, W. Li, M. C. Leu, and G. E. Hilmas, "A novel freeform extrusion fabrication process for producing solid ceramic components with uniform layered radiation drying," Addit. Manuf., vol. 15, pp. 102–112, May 2017.

[45] C. Haase, F. Tang, M. B. Wilms, A. Weisheit, and B. Hallstedt, "Combining thermodynamic modeling and 3D printing of elemental powder blends for high-throughput investigation of high-entropy alloys – Towards rapid alloy screening and design," Mater. Sci. Eng. A, vol. 688, pp. 180–189, Mar. 2017.

[46] S. Praveen and H. S. Kim, "High-Entropy Alloys: Potential Candidates for High-Temperature Applications – An Overview," Adv. Eng. Mater., vol. 20, no. 1, p. 1700645, Jan. 2018.

[47] E. P. George, W. A. Curtin, and C. C. Tasan, "High entropy alloys: A focused review of mechanical properties and deformation mechanisms," Acta Materialia, vol. 188. Acta Materialia Inc, pp. 435–474, 15-Apr-2020.

[48] W. Cui, M. S. Moats, A. Luyima, and C. Heckman, "Examination of copper electrowinning smoothing agents. Part III. Chloride interaction with HydroStar and Cyquest N-900," Miner. Metall. Process., vol. 33, no. 1, pp. 31–38, Feb. 2016.

[49] A. Luyima, W. Cui, C. Heckman, and M. S. Moats, "Examination of copper electrowinning smoothing agents. Part IV: Nucleation and growth of copper on stainless steel," Miner. Metall. Process., vol. 33, no. 1, pp. 39–46, Feb. 2016.

[50] W. Cui, "Effect and interactions of commercial additives and chloride ion in copper electrowinning," 2014.

[51] M. S. Moats, A. Luyima, and W. Cui, "Examination of copper electrowinning smoothing agents. Part I: A review," Miner. Metall. Process., vol. 33, no. 1, pp. 7–13, Feb. 2016.

[52] A. Luyima, M. S. Moats, W. Cui, and C. Heckman, "Examination of copper electrowinning smoothing agents. Part II: Fundamental electrochemical examination of DXG-F7," Miner. Metall. Process., vol. 33, no. 1, pp. 14–22, Feb. 2016.

[53] J. Joseph, T. Jarvis, X. Wu, N. Stanford, P. Hodgson, and D. M. Fabijanic, "Comparative study of the microstructures and mechanical properties of direct laser fabricated and arc-melted AlxCoCrFeNi high entropy alloys," Mater. Sci. Eng. A, vol. 633, pp. 184–193, May 2015.

[54] H. R. Sistla, J. W. Newkirk, and F. Frank Liou, "Effect of Al/Ni ratio, heat treatment on phase transformations and microstructure of AlxFeCoCrNi2-x (x=0.3, 1) high entropy alloys," Mater. Des., vol. 81, pp. 113–121, Sep. 2015.

[55] Z. Tang et al., "Tensile ductility of an AlCoCrFeNi multi-phase high-entropy alloy through hot isostatic pressing (HIP) and homogenization," Mater. Sci. Eng. A, vol. 647, pp. 229–240, Oct. 2015.

[56] C. M. Lin and H. L. Tsai, "Evolution of microstructure, hardness, and corrosion properties of high-entropy Al0.5CoCrFeNi alloy," Intermetallics, vol. 19, no. 3, pp. 288–294, Mar. 2011.

[57] J. W. Qiao, S. G. Ma, E. W. Huang, C. P. Chuang, P. K. Liaw, and Y. Zhang, "Microstructural characteristics and mechanical behaviors of AlCoCrFeNi high-entropy alloys at ambient and cryogenic temperatures," in Materials Science Forum, 2011, vol. 688, pp. 419–425.

[58] S. G. Ma and Y. Zhang, "Effect of Nb addition on the microstructure and properties of AlCoCrFeNi high-entropy alloy," Mater. Sci. Eng. A, vol. 532, pp. 480–486, Jan. 2012.

[59] W. R. Wang, W. L. Wang, S. C. Wang, Y. C. Tsai, C. H. Lai, and J. W. Yeh, "Effects of Al addition on the microstructure and mechanical property of Al xCoCrFeNi high-entropy alloys," Intermetallics, vol. 26, pp. 44–51, Jul. 2012.

[60] A. Manzoni, H. Daoud, R. Völkl, U. Glatzel, and N. Wanderka, "Phase separation in equiatomic AlCoCrFeNi high-entropy alloy," Ultramicroscopy, vol. 132, pp. 212–215, Sep. 2013.

[61] R. Wang, K. Zhang, C. Davies, and X. Wu, "Evolution of microstructure, mechanical and corrosion properties of AlCoCrFeNi high-entropy alloy prepared by direct laser fabrication," J. Alloys Compd., vol. 694, pp. 971–981, Feb. 2017.

[62] S. Gorsse, C. Hutchinson, M. Gouné, and R. Banerjee, "Additive manufacturing of metals: a brief review of the characteristic microstructures and properties of steels, Ti-6Al-4V and high-entropy alloys," Sci. Technol. Adv. Mater., vol. 18, no. 1, pp. 584–610, Dec. 2017.

[63] H. Zhang, Y. Pan, Y. He, and H. Jiao, "Microstructure and properties of 6FeNiCoSiCrAlTi high-entropy alloy coating prepared by laser cladding," Appl. Surf. Sci., vol. 257, no. 6, pp. 2259–2263, Jan. 2011.

[64] C. Huang, Y. Zhang, J. Shen, and R. Vilar, "Thermal stability and oxidation resistance of laser clad TiVCrAlSi high entropy alloy coatings on Ti-6Al-4V alloy," Surf. Coatings Technol., vol. 206, no. 6, pp. 1389–1395, Dec. 2011.

[65] H. Zhang, Y. He, and Y. Pan, "Enhanced hardness and fracture toughness of the laser-solidified FeCoNiCrCuTiMoAlSiB0.5 high-entropy alloy by martensite strengthening," Scr. Mater., vol. 69, no. 4, pp. 342–345, Aug. 2013.

[66] X. W. Qiu and C. G. Liu, "Microstructure and properties of Al2CrFeCoCuTiNix high-entropy alloys prepared by laser cladding," J. Alloys Compd., vol. 553, pp. 216–220, Mar. 2013.

[67] X. Ye, M. Ma, Y. Cao, W. Liu, X. Ye, and Y. Gu, "The property research on high-entropy alloy AlxFeCoNiCuCr coating by laser cladding," in Physics Procedia, 2011, vol. 12, no. PART 1, pp. 303–312.

[68] H. Zhang, Y. Z. He, Y. Pan, and S. Guo, "Thermally stable laser cladded CoCrCuFeNi high-entropy alloy coating with low stacking fault energy," Journal of Alloys and Compounds, vol. 600. Elsevier Ltd, pp. 210–214, 05-Jul-2014.

[69] I. Kunce, M. Polanski, K. Karczewski, T. Plocinski, and K. J. Kurzydlowski, "Microstructural characterisation of high-entropy alloy AlCoCrFeNi fabricated by laser engineered net shaping," J. Alloys Compd., vol. 648, pp. 751–758, Jul. 2015.

[70] T. M. Yue, H. Xie, X. Lin, H. O. Yang, and G. H. Meng, "Solidification behaviour in laser cladding of AlCoCrCuFeNi high-entropy alloy on magnesium substrates," J. Alloys Compd., vol. 587, pp. 588–593, Feb. 2014.

[71] Y. Shon, S. S. Joshi, S. Katakam, R. Shanker Rajamure, and N. B. Dahotre, "Laser additive synthesis of high entropy alloy coating on aluminum: Corrosion behavior," Mater. Lett., vol. 142, pp. 122–125, Mar. 2015.

[72] S. Zhang, C. L. Wu, C. H. Zhang, M. Guan, and J. Z. Tan, "Laser surface alloying of FeCoCrAlNi high-entropy alloy on 304 stainless steel to enhance corrosion and cavitation erosion resistance," Opt. Laser Technol., vol. 84, pp. 23–31, Oct. 2016.

[73] J. Liu, H. Liu, P. Chen, and J. Hao, "Microstructural characterization and corrosion behaviour of AlCoCrFeNiTi x high-entropy alloy coatings fabricated by laser cladding," Surf. Coatings Technol., vol. 361, pp. 63–74, Mar. 2019.

[74] C. L. Wu, S. Zhang, C. H. Zhang, H. Zhang, and S. Y. Dong, "Phase evolution and cavitation erosion-corrosion behavior of FeCoCrAlNiTixhigh entropy alloy coatings on 304 stainless steel by laser surface alloying," J. Alloys Compd., vol. 698, pp. 761–770, Mar. 2017.

[75] T. Borkar et al., "A combinatorial assessment of AlxCrCuFeNi2 ($0 < x < 1.5$) complex concentrated alloys: Microstructure, microhardness, and magnetic properties," Acta Mater., vol. 116, pp. 63–76, Sep. 2016.

[76] A. Ghazanfari, W. Li, M. C. Leu, Y. Zhuang, and J. Huang, "Advanced ceramic components with embedded sapphire optical fiber sensors for high temperature applications," Mater. Des., vol. 112, pp. 197–206, Dec. 2016.

[77] A. Ghazanfari, W. Li, M. C. Leu, J. Watts, Y. Zhuang, and J. Huang, "Freeform extrusion fabrication of advanced ceramic components with embedded sapphire optical fiber sensors," in ASME 2016 Conference on Smart Materials, Adaptive Structures and Intelligent Systems, SMASIS 2016, 2016, vol. 1.

[78] Z. Tang, L. Huang, W. He, and P. Liaw, "Alloying and Processing Effects on the Aqueous Corrosion Behavior of High-Entropy Alloys," Entropy, vol. 16, no. 2, pp. 895–911, Feb. 2014.

[79] J. Lu et al., "Effect of Al content on the oxidation behavior of Y/Hf-doped AlCoCrFeNi high-entropy alloy," Corros. Sci., vol. 170, p. 108691, Jul. 2020.

[80] Y. Zhang et al., "Microstructures and properties of high-entropy alloys," Progress in Materials Science, vol. 61. Elsevier Ltd, pp. 1–93, 01-Apr-2014.

[81] S. Y. Chang, C. E. Li, Y. C. Huang, H. F. Hsu, J. W. Yeh, and S. J. Lin, "Structural and thermodynamic factors of suppressed interdiffusion kinetics in multi-component high-entropy materials," Sci. Rep., vol. 4, no. 1, pp. 1–8, Feb. 2014.

[82] D. L. Beke and G. Erdélyi, "On the diffusion in high-entropy alloys," Mater. Lett., vol. 164, pp. 111–113, Feb. 2016.

[83] K. Y. Tsai, M. H. Tsai, and J. W. Yeh, "Sluggish diffusion in Co-Cr-Fe-Mn-Ni high-entropy alloys," Acta Mater., vol. 61, no. 13, pp. 4887–4897, Aug. 2013.

[84] W. Cui, X. Zhang, and F. Liou, "Additive Manufacturing of High-Entropy Alloys - A Review," in Proceedings of the 28th Annual Solid Freeform Fabrication Symposium, 2017, pp. 712–724.

[85] W. Cui, W. Li, W.-T. Chen, and F. Liou, "Laser Metal Deposition of an AlCoCrFeNiTi0.5 High-Entropy Alloy Coating on a Ti6Al4V Substrate: Microstructure and Oxidation Behavior," Crystals, vol. 10, no. 8, p. 638, Jul. 2020.

[86] L. Yan et al., "Mechanical Properties Evaluation of a Ti-6Al-4V Thin-Wall Structure Produced by a Hybrid Manufacturing Process," in Proceedings of the 29th Annual Solid Freeform Fabrication Symposium, 2018, pp. 291–301.

[87] T. M. Butler and M. L. Weaver, "Oxidation behavior of arc melted AlCoCrFeNi multi-component high-entropy alloys," J. Alloys Compd., vol. 674, pp. 229–244, Jul. 2016.

[88] P. K. Huang, J. W. Yeh, T. T. Shun, and S. K. Chen, "Multi-principal-element alloys with improved oxidation and wear resistance for thermal spray coating," Adv. Eng. Mater., vol. 6, no. 1–2, pp. 74–78, Feb. 2004.

[89] C. M. Liu, H. M. Wang, S. Q. Zhang, H. B. Tang, and A. L. Zhang, "Microstructure and oxidation behavior of new refractory high entropy alloys," J. Alloys Compd., vol. 583, pp. 162–169, Jan. 2014.

[90] M. H. Chuang, M. H. Tsai, W. R. Wang, S. J. Lin, and J. W. Yeh, "Microstructure and wear behavior of AlxCo 1.5CrFeNi1.5Tiy high-entropy alloys," Acta Mater., vol. 59, no. 16, pp. 6308–6317, Sep. 2011.

[91] O. N. Senkov, S. V. Senkova, D. M. Dimiduk, C. Woodward, and D. B. Miracle, "Oxidation behavior of a refractory NbCrMo 0.5Ta 0.5TiZr alloy," J. Mater. Sci., vol. 47, no. 18, pp. 6522–6534, Sep. 2012.

[92] T. M. Butler, J. P. Alfano, R. L. Martens, and M. L. Weaver, "High-Temperature Oxidation Behavior of Al-Co-Cr-Ni-(Fe or Si) Multicomponent High-Entropy Alloys," JOM, vol. 67, no. 1, pp. 246–259, Nov. 2015.

[93] X. Li, X. Jia, Q. Yang, and J. Lee, "Quality analysis in metal additive manufacturing with deep learning," J. Intell. Manuf., pp. 1–15, 2020.

[94] D. Cerniglia, M. Scafidi, A. Pantano, and J. Rudlin, "Inspection of additive-manufactured layered components," Ultrasonics, vol. 62, pp. 292–298, Sep. 2015.

[95] X. Li, W. Li, F. Rezaei, and A. Rownaghi, "Catalytic cracking of n-hexane for producing light olefins on 3D-printed monoliths of MFI and FAU zeolites," Chem. Eng. J., vol. 333, pp. 545–553, Feb. 2018.

[96] W. Cui, S. Karnati, X. Zhang, E. Burns, and F. Liou, "Fabrication of AlCoCrFeNi High-Entropy Alloy Coating on an AISI 304 Substrate via a CoFe2Ni Intermediate Layer," Entropy, vol. 21, no. 1, p. 2, Dec. 2019.

[97] M. Borish, B. K. Post, A. Roschli, P. C. Chesser, L. J. Love, and K. T. Gaul, "Defect Identification and Mitigation Via Visual Inspection in Large-Scale Additive Manufacturing," JOM, vol. 71, no. 3, pp. 893–899, Mar. 2019.

[98] W. Cui, Y. Zhang, X. Zhang, L. Li, and F. Liou, "Metal Additive Manufacturing Parts Inspection Using Convolutional Neural Network," Appl. Sci., vol. 10, no. 2, p. 545, Jan. 2020.

[99] W. Li et al., "Fabricating Functionally Graded Materials by Ceramic On-Demand Extrusion with Dynamic Mixing," in Proceedings of the 29th Annual Solid Freeform Fabrication Symposium, 2018, pp. 1087–1099.

[100] M. Seifi et al., "Progress Towards Metal Additive Manufacturing Standardization to Support Qualification and Certification," JOM, vol. 69, no. 3. Minerals, Metals and Materials Society, pp. 439–455, 01-Mar-2017.

[101] F. H. Kim and S. P. Moylan, "Literature Review of Metal Additive Manufacturing Defects," NIST Adv. Manuf. Ser., pp. 100–116, 2018.

[102] W. Li et al., "Extrusion-based additive manufacturing of functionally graded ceramics," J. Eur. Ceram. Soc., vol. 41, no. 3, pp. 2049–2057, Mar. 2021.

[103] H. Baumgartl, J. Tomas, R. Buettner, and M. Merkel, "A deep learning-based model for defect detection in laser-powder bed fusion using in-situ thermographic monitoring," Prog. Addit. Manuf., vol. 5, no. 3, pp. 277–285, Sep. 2020.

[104] B. Zhang, P. Jaiswal, R. Rai, P. Guerrier, and G. Baggs, "Convolutional neural network-based inspection of metal additive manufacturing parts," Rapid Prototyp. J., vol. 25, no. 3, pp. 530–540, Apr. 2019.

[105] C. Wang, X. P. Tan, S. B. Tor, and C. S. Lim, "Machine learning in additive manufacturing: State-of-the-art and perspectives," Additive Manufacturing, vol. 36. Elsevier B.V., p. 101538, 01-Dec-2020.

[106] L. Meng et al., "Machine Learning in Additive Manufacturing: A Review," JOM, vol. 72, no. 6. Springer, pp. 2363–2377, 01-Jun-2020.

[107] C. Gobert, E. W. Reutzel, J. Petrich, A. R. Nassar, and S. Phoha, "Application of supervised machine learning for defect detection during metallic powder bed fusion additive manufacturing using high resolution imaging.," Addit. Manuf., vol. 21, pp. 517–528, May 2018.

[108] F. Amato, A. López, E. M. Peña-Méndez, P. Vaňhara, A. Hampl, and J. Havel, "Artificial neural networks in medical diagnosis," Journal of Applied Biomedicine, vol. 11, no. 2. University of South Bohemia, pp. 47–58, 01-Jan-2013.

[109] M. de Bruijne, "Machine learning approaches in medical image analysis: From detection to diagnosis," Medical Image Analysis, vol. 33. Elsevier B.V., pp. 94–97, 01-Oct-2016.

[110] J. Wang, Y. Ma, L. Zhang, R. X. Gao, and D. Wu, "Deep learning for smart manufacturing: Methods and applications," J. Manuf. Syst., vol. 48, pp. 144–156, Jul. 2018.

[111] J. L. Bartlett, A. Jarama, J. Jones, and X. Li, "Prediction of microstructural defects in additive manufacturing from powder bed quality using digital image correlation," Mater. Sci. Eng. A, vol. 794, p. 140002, Sep. 2020.

[112] T. Young, D. Hazarika, S. Poria, and E. Cambria, "Recent trends in deep learning based natural language processing [Review Article]," IEEE Computational Intelligence Magazine, vol. 13, no. 3. Institute of Electrical and Electronics Engineers Inc., pp. 55–75, 01-Aug-2018.

[113] M. Liang and X. Hu, "Recurrent Convolutional Neural Network for Object Recognition," in In Proceedings of the IEEE conference on computer vision and pattern recognition, 2015, pp. 3367–3375.

[114] C. E. Tuncali, G. Fainekos, H. Ito, and J. Kapinski, "Simulation-based Adversarial Test Generation for Autonomous Vehicles with Machine Learning Components," in IEEE Intelligent Vehicles Symposium, Proceedings, 2018, vol. 2018-June, pp. 1555–1562.

[115] L. Scime and J. Beuth, "Using machine learning to identify in-situ melt pool signatures indicative of flaw formation in a laser powder bed fusion additive manufacturing process," Addit. Manuf., vol. 25, pp. 151–165, Jan. 2019.

[116] M. Khanzadeh, S. Chowdhury, M. Marufuzzaman, M. A. Tschopp, and L. Bian, "Porosity prediction: Supervised-learning of thermal history for direct laser deposition," J. Manuf. Syst., vol. 47, pp. 69–82, Apr. 2018.

[117] R. Raina, A. Battle, H. Lee, B. Packer, and A. Y. Ng, "Self-taught learning: Transfer learning from unlabeled data," in ACM International Conference Proceeding Series, 2007, vol. 227, pp. 759–766.

[118] M. I. Jordan and T. M. Mitchell, "Machine learning: Trends, perspectives, and prospects," Science, vol. 349, no. 6245. American Association for the Advancement of Science, pp. 255–260, 17-Jul-2015.

[119] X. Zhai, Y. Yin, J. W. Pellegrino, K. C. Haudek, and L. Shi, "Applying machine learning in science assessment: a systematic review," Studies in Science Education, vol. 56, no. 1. Routledge, pp. 111–151, 02-Jan-2020.

[120] D. Silver et al., "A general reinforcement learning algorithm that masters chess, shogi, and Go through self-play," Science (80-.)., vol. 362, no. 6419, pp. 1140–1144, Dec. 2018.

[121] O. Vinyals et al., "Grandmaster level in StarCraft II using multi-agent reinforcement learning," Nature, vol. 575, no. 7782, pp. 350–354, Nov. 2019.

[122] F. Y. Wang et al., "Where does AlphaGo go: From church-turing thesis to AlphaGo thesis and beyond," IEEE/CAA J. Autom. Sin., vol. 3, no. 2, pp. 113–120, Apr. 2016.

[123] S. Singh, A. Okun, and A. Jackson, "Artificial intelligence: Learning to play Go from scratch," Nature, vol. 550, no. 7676. Nature Publishing Group, pp. 336–337, 18-Oct-2017.

[124] C. Wan et al., "An artificial sensory neuron with visual-haptic fusion," Nat. Commun., vol. 11, no. 1, pp. 1–9, Dec. 2020.

[125] K. Aoyagi, H. Wang, H. Sudo, and A. Chiba, "Simple method to construct process maps for additive manufacturing using a support vector machine," Addit. Manuf., vol. 27, pp. 353–362, May 2019.

[126] A. Douard, C. Grandvallet, F. Pourroy, and F. Vignat, "An Example of Machine Learning Applied in Additive Manufacturing," in IEEE International Conference on Industrial Engineering and Engineering Management, 2019, vol. 2019-December, pp. 1746–1750.

[127] F. Caiazzo and A. Caggiano, "Laser Direct Metal Deposition of 2024 Al Alloy: Trace Geometry Prediction via Machine Learning," Materials (Basel)., vol. 11, no. 3, p. 444, Mar. 2018.

[128] J. Jiang, G. Hu, X. Li, X. Xu, P. Zheng, and J. Stringer, "Analysis and prediction of printable bridge length in fused deposition modelling based on back propagation neural network," Virtual Phys. Prototyp., vol. 14, no. 3, pp. 253–266, Jul. 2019.

[129] D. Ye, G. S. Hong, Y. Zhang, K. Zhu, and J. Y. H. Fuh, "Defect detection in selective laser melting technology by acoustic signals with deep belief networks," Int. J. Adv. Manuf. Technol., vol. 96, no. 5–8, pp. 2791–2801, May 2018.

[130] S. A. Shevchik, G. Masinelli, C. Kenel, C. Leinenbach, and K. Wasmer, "Deep learning for in situ and real-time quality monitoring in additive manufacturing using acoustic emission," IEEE Trans. Ind. Informatics, vol. 15, no. 9, pp. 5194–5203, 2019.

[131] Y. Lecun, Y. Bengio, and G. Hinton, "Deep learning," Nature, vol. 521, no. 7553. Nature Publishing Group, pp. 436–444, 27-May-2015.

[132] A. Krizhevsky, I. Sutskever, and G. E. Hinton, "ImageNet Classification with Deep Convolutional Neural Networks," in Advances in neural information processing systems, 2012, pp. 1097–1105.

[133] R. Kondo, S. Yamakawa, Y. Masuoka, S. Tajima, and R. Asahi, "Microstructure recognition using convolutional neural networks for prediction of ionic conductivity in ceramics," Acta Mater., vol. 141, pp. 29–38, Dec. 2017.

[134] M. W. Akram et al., "CNN based automatic detection of photovoltaic cell defects in electroluminescence images," Energy, vol. 189, p. 116319, Dec. 2019.

[135] X. Qi, G. Chen, Y. Li, X. Cheng, and C. Li, "Applying Neural-Network-Based Machine Learning to Additive Manufacturing: Current Applications, Challenges, and Future Perspectives," Engineering, vol. 5, no. 4. Elsevier Ltd, pp. 721–729, 01-Aug-2019.

VITA

Wenyuan Cui was born and grew up in China. Influenced by her family and high school teachers, she studied Materials Science and Engineering at Central South University, Changsha, China. After received her B.S. degree in 2012, she continued her M.S. study in Materials Science and Engineering at Missouri University of Science and Technology (Missouri S&T), Rolla, MO. During 2014-2016, she worked as an Engineer in Freeport-McMoRan Inc. She conducted metallurgical work, provided data-driven solutions to meet the operation strategy and business needs. She enjoyed working with different people, had the curiosity of the new technology and the ambitious of pushing the current technology boundary forward, which motivated her to pursue a Ph.D. degree in Mechanical Engineering. She joined Dr. Frank Liou's lab in January 2017 and had been working on the development of the High-entropy alloys (HEAs) and deep-learning based inspection in additive manufacturing. During her Ph.D. study, she authored and co-authored 20 journal publications and 8 conference papers. She completed her second master's degree in Applied Mathematics in May 2020. In May 2021, she received her Doctorate degree in Mechanical Engineering from Missouri S&T under the direction of Dr. Frank Liou.